THE UNIVERSITY OF CHICAGO

TIME-RESOLVED SURFACE DYNAMICS: DIRECTED REACTIVITY, EXTRATERRESTRIAL ICES, AND NERVE AGENT SIMULANTS

A DISSERTATION SUBMITTED TO

THE FACULTY OF THE DIVISION OF THE PHYSICAL SCIENCES

IN CANDIDACY FOR THE DEGREE OF

DOCTOR OF PHILOSOPHY

DEPARTMENT OF CHEMISTRY

BY

GRANT GREGORY LANGLOIS

CHICAGO, ILLINOIS

MARCH 2017

These violent delights

have violent ends

Table of Contents

List of Figures

Acknowledgments (A Chronology)

To Sandy, who not only doggedly kept the roof over our heads, but stayed on top of a lazy student and found the money California State University Stanislaus was eager to give away.

To Greg, the original storyteller, who would tell you he did nothing with his Master's degree in English, but had a son reading by age two.

To Nana, the savior of a working single mother of three, who lived not once, but twice. She's undoubtedly still laughing.

To Evan and Lyrica, who have held the fort for over ten years by this point and emerged extraordinary adults nonetheless.

To Ann, who recognized that first grade just wasn't worth my time.

To Paul, Mallory, and Myles, who all taught me how to take myself much less seriously.

To Graeme, the extrovert to my introvert, my oldest friend, who thankfully always kept me way the hell out of my shell, and who I know won't ever stop doing so.

To the Criminal Justice major advisor—a name I unfortunately don't remember—who insisted I switch to Chemistry so I'd have an actual marketable skill.

To Shane, who encouraged the student looking to take double the full-time level of coursework each semester.

To Rose, who couldn't get me to leave Chemistry, but showed me what I was missing out on in the world of Physics.

To Michael, who was the first person to articulate that graduate school was a bright and worthwhile future.

To Zack, hater of the shirt collar, who was the first to reach out, and is literally *the* reason I'm in the present group and lab—I am grateful for every day I don't sit in front of an STM.

To Pat, who may not realize that he got me to *enjoy* my first beer. It was an IPA, by the way.

To Ben, Mark, Alex, Nick, Chad, Johnny, Dubs, Frank, and John, the most colorful cast for the production called graduate school.

To Ryan, who got my instrument up and running after we turned it into a fish tank.

To Wenxin, my partner in the trenches, conspirator in said crime of turning our instrument into a fish tank, who educated me in the many wonderful culinary and cultural eccentricities of China.

To Kevin, the unrelenting wit—literally the funniest person I've met, who force-fed me David Foster Wallace and helped usher in me a rediscovery of the joy in reading.

To Becca, the walking embodiment of moxie, who breathed new life into the waning years of graduate school with our shared passions for food and jamming to thumping beats.

To Dan, Chris, Gaby, Natalie, Qianqian, Ying, Tuo, Hyung Ju, Bryan, Jay, Michelle, Katherine, Jon, Jeff, Darren, Ross, Tim, Kathryn, Ellen, Jacob, Tim, Sarah, Michelle, Alison, and Julie, literally the best group one could ask for.

To John, Maria, Tanya, Helmut, Luigi, Qiti, Dave, and Gerry, who kept it all running.

To Cagey, the man behind the curtain.

To Ka Yee and Greg, who will help guide me to the finish line.

To Steve, who instilled the importance of fearlessness in me on day one, and who granted me the autonomy I needed to flourish as a scientist and a thinker.

…

To Traci, the riverbed, the "life" half of work-life balance, my *Adenium obesum*. I'll always cherish meeting you at a very strange time in your life; your brushstrokes have certainly colored mine.

Abstract

This thesis describes a diverse cross-section of interfacial surface chemistry, ranging from investigating controlling reaction dynamics with an ordered surface, to modifying extraterrestrial ice, to destroying chemical warfare agents.

In an update to the days of oriented, crossed molecular beam experiments, self-assembled monolayers of thiolates on gold were used as a participant in an $O(^3P)$ addition reaction, showing that restricting collisions to mainly unfavorable mutual orientation produces a low reaction probability despite sufficient energetics. The use of the ordered monolayer aids in rapid dissipation of collision energy, leaving intermediates that would normally rip apart in the gas phase.

It has also been shown that neutral gaseous projectiles traveling with large momentum can directly embed into amorphous water ice, remaining trapped until the ice can desorb. This discovery, novel in the case of neutral projectiles, better informs modeling growth of astrophysical bodies and aircraft icing.

Finally, the destruction by $O(^3P)$ of a pair of condensed-phase films of compounds simulating the G-series chemical warfare agents was studied, showing the close proximity afforded to intermediates resulted in formation of polymeric overlayers that exhibit greater thermal stability than the original simulants. These overlayers restrict the rate of destruction as they form.

These experiments highlight the efficacy and wide applicability of time-resolved reflection-absorption infrared spectroscopy of surfaces during exposure to streams of atoms and molecules of tunable energy and flux.

Chapter 1

Introduction: A Cross-Section of Interfacial Chemistry

Good science is not typically borne of vacuum, but the science in this thesis takes place *in* vacuum. Indeed, the world of ultrahigh vacuum surface chemistry is one of cleanliness. In order to trust the data one must ensure that the surroundings are clean, that they are orderly, and that they remain so. This is dogma. Single crystals are precisely cut, meticulously cleaned, and their surroundings pumped free of background: on the order of one ten-trillionth of the pressure one experiences on Earth, low enough that a single molecule-thick layer of water takes *at least* three hours to form. If an atom or molecule collides with a condensate, it better be the intended one. If two atoms or molecules are careening toward each other through space, there better not be rogue species in the way.

On that last note, the science—not to mention the instrumentation discussed in **Chapter 2**—in this thesis owes a great deal to the pioneering work done by scientists studying molecular dynamics using crossed molecular beams. A molecular beam is an extremely useful tool used to produce collision-free streams of gas, and the supersonic beams referenced herein provide for high fluxes of gas with tunable energies; through various methods, the kinetic and internal energies are highly customizable, with high resolution available in both energy and spatial distribution (collimation). This technology bred the "spherical cow" of chemistry: two species colliding, initial conditions controlled, virtually free of outside influence.

But collisions with surfaces are much harder—and sometimes softer. When one thinks of surfaces, the connotation is one of rigidity or regularity, of order. Surface chemistry is, however, rarely this

straightforward, testified by the large cross-section of topics tackled in this thesis. In **Chapter 3**, the chemistry occurring at the oriented interface of a well-ordered, self-assembled monolayer is messy, despite these structures being championed as well-defined and rigid. There is plenty of energy at room temperature, though, and these surfaces effectively dissipate excess energy from collisions, making them prime candidates for ensembles of reactants ripe for exploitation for what is defined as "stereodynamic" control, or the control of mutual orientation. Reaction intermediates that would be ripped apart in the gas phase are instead stabilized on the surface for detection. The system studied, oxygen atom additions onto unsaturated carbon bonds, produces interesting results: restriction of collisions to mostly unfavorable orientations yields a low reaction probability despite the system's energy far above the energetic barrier. This framework proves a promising lead for updating the methods behind crossed, oriented molecular beams.

Disordered surfaces, such as the amorphous, "glassy" ices of **Chapter 4**, present entirely different challenges. Amorphous solid water, or ASW, is a form of ice that exists primarily in space. The genesis of astrophysical icy bodies is an important field of study that addresses questions of planet creation, atmosphere formation, and could even address the origins of life on Earth. When studying processes that occur slowly over extremely long periods of time, even low-probability events can be vital to modelling and understanding. Thus, the discovery of the previously unobserved "ballistic embedding" process, where neutral gases traveling with high momentum can embed into amorphous ice and remain at surface temperatures far above their thermodynamic sticking temperature, casts the modification of icy surfaces in a new light. On a more terrestrial level, this work could also inform better modeling of ice accumulation on aircraft.

Finally, surface chemistry makes a clear real-world connection in **Chapters 5 and 6**, where the study of chemical warfare agent remediation is viewed through the lens of basic science.

Destruction of species similar in chemical structure to real nerve agents such as Sarin and Soman—called "simulants" in the literature—is accomplished through use of one of the most basic oxidants, atomic oxygen in its ground electronic state, $O(^3P)$. The condensed-phase nature of this system—the close proximities involved—yields a cacophony of reaction pathways, and an overlayer is generated that hinders effective destruction of the simulants and their release from the surface. In the race for cleaner effective remediation techniques, this work informs the use of plasma-based decontamination methods

Chapter 2

Experimental Methods

All experimentation described in this thesis was chiefly performed in an ultrahigh vacuum chamber (UHV) with a base pressure historically below 1 x 10^{-10} Torr, with typical operating pressures ranging from ~10^{-8} Torr for the SAM experiments described in **Chapter 3** (due to frequent venting required for sample changes), to a significantly cleaner ~10^{-10} Torr for the CO_2 experiments described in **Chapter 4** to discourage background water interference. Housed within the chamber are the optics necessary for performing reflection-absorption infrared spectroscopy (RAIRS) and X-ray photoelectron spectroscopy (XPS). These technologies allowed for *in situ* resolution of sub-monolayer structural changes to surfaces of interest in real time (RAIRS), as well as elemental analysis of the surfaces (XPS) as prepared or after modification. The chamber is also outfitted for performing low-energy electron diffraction and Auger electron spectroscopy of surfaces, but these methods are not discussed in this thesis and their operation is therefore omitted herein.

The chamber is connected, *via* manually-operated gate valve, to a triply-differentially-pumped supersonic molecular beamline. The beamline is used to source collimated, collision-free streams of atoms or molecules at highly-tunable, well-defined kinetic energies with high fluxes (up to ~10^{20} cm^{-2} s^{-1}). Two different sources were used in the beamline: a custom-designed, water-cooled quartz nozzle used to generate radio frequency (RF) plasmas within the source gas, principally used for generating beams containing reactive O(^{3}P) (**Chapters 3, 5, 6**), and a stainless-steel nozzle with customizable pinhole sizes (15-200 μm), capable of heating the source gas to a maximum of 1200 K (**Chapter 4**). A quadrupole mass spectrometer (QMS) in the main chamber is used to

characterize the beam each time it is run, typically at both the beginning and end of a day's experiment.

Analytical Instrumentation of the Main Chamber

The main commercial UHV chamber (TNB-X, Perkin-Elmer), is composed of two different levels or "planes," shown in **Figure 2-1**. The lower plane is on the same level as the beamline and contains several mirrors for directing infrared radiation off the center of a surface placed directly in front of the beamline. This is the main operating position of the instrument, where changes in the surface induced by exposure to the beam are monitored in real time, allowing for direct measurement of kinetics that take place on the order of minutes or seconds. Approximately 24 cm above this position is the main chamber's second plane, used mainly for secondary *in situ* XPS analyses and sample cleaning *via* Ar^+ ion sputtering.

After bake-out, this chamber's ultimate pressure is nominally ~10^{-10} Torr or below before any sample cooling, as measured by a Bayard-Alpert-type nude ion gauge. The vacuum is maintained by a 260 L s^{-1} turbomolecular pump (HiPace 300, Pfeiffer Vacuum) backed by a 3 L s^{-1} dry scroll pump (nXDS10i, Edwards Vacuum).

Reflection-Absorption Infrared Spectroscopy (RAIRS)

RAIRS monitors the changes in the vibrational modes of molecules physisorbed or covalently bonded to a reflective metal substrate of choice. Vibrational spectroscopy of surfaces, in general, is a powerful tool that allows for detection of chemical species on a surface, as well as immediate chemical environments and molecular structure. High resolution is achieved due to the fact that spectral bandwidths are determined solely by heterogeneities and surface-molecule interactions.[1] The technique follows the same basic principles of typical Fourier transform infrared spectroscopy

Figure 2-1

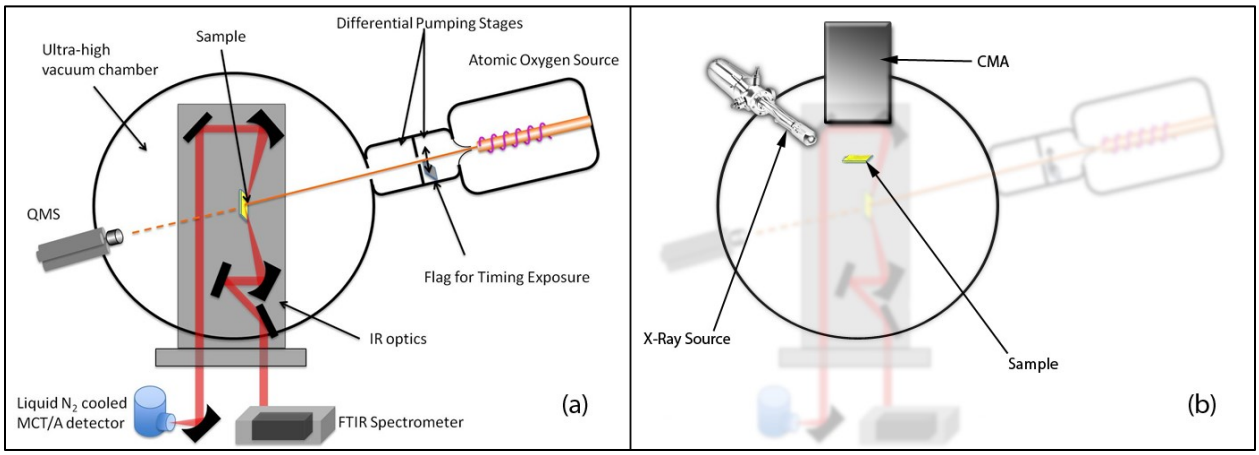

Layout of main UHV chamber instrumentation. *(a) Lower plane capable of performing time-resolved RAIRS with simultaneous exposure to the molecular beam. (b) Second plane, with necessary instrumentation for performing XPS.*

(FTIR), with one very distinct exception: only vibrational excitations normal to the surface are detected. This is due to the fact that transition dipole moments (TDM) parallel to the metal substrate induce an equal and opposite image dipole in the metal, yielding a net zero-intensity TDM. This provides for an additional aspect of detection, allowing qualitative (and sometimes near-quantitative) determination of molecular orientation relative to the substrate plane, as seen in **Chapter 3**.

The phase change of light reflected from a metal surface depends on both its incident angle and polarization.[2] Defining the "plane of incidence" as that containing the rays of incident light, reflected light and the surface normal, as shown in **Figure 2-2**, the electric field vector can be broken up into two components: *s*- and *p*-polarized, corresponding to light perpendicular and parallel to the plane of incidence, respectively.[1] Regardless of the incident angle, all *s*-polarized light waves experience a phase shift of nearly 180° upon reflection from a metal surface, and thus form a standing-wave field that participates in a negligible capacity regarding vibrational excitation of the deposited layer. Conversely, *p*-polarized light waves experience phase shifts that are highly dependent upon incident angle, changing most rapidly near glancing angles. Greenler demonstrated theoretically that maximum reflectance occurs at an angle of 86° relative to the surface normal for a model system of a thin organic layer deposited on a gold surface.[2,3]

In terms of experimental design, maximum signal therefore requires incident light to be polarized perpendicular to the substrate's surface prior to incidence at a glancing angle. Incoming light from the FTIR spectrometer (Nicolet 6700, Thermo Fischer Scientific) is polarized in a nitrogen-purged area outside of the UHV chamber so that it is entirely perpendicular to the surface upon incidence. Custom optics mounted inside the UHV chamber direct the polarized light so that its angle of incidence with a given surface is 75°. The reflected light is directed outside of the chamber into a

Figure 2-2

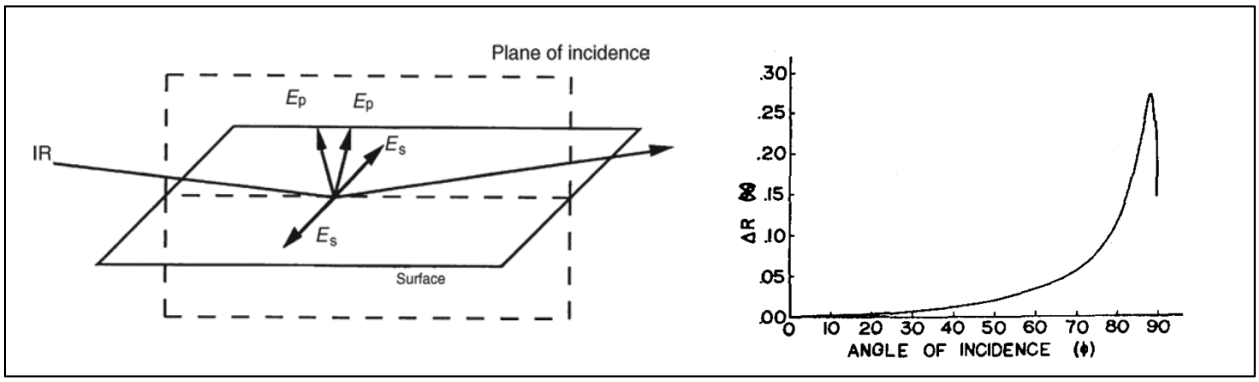

Theoretical description of RAIRS. *As defined within the plane of incidence, s-polarized light undergoes a nearly 180° phase shift upon reflectance, the resultant standing field participating negligibly in excitation of a deposited film. The intensity of the p-polarized standing field is highly dependent upon incident angle, peaking at ~86° for a model organic film on gold.*

liquid-nitrogen-cooled mercury cadmium telluride detector (MCT/A), providing large band intensities within the 4000 – 650 cm^{-1} range. Typical spectra used throughout this thesis are composed of averages of 100 to 1000 scans obtained at resolutions of either 2 cm^{-1} (**Chapter 3**) or 4 cm^{-1} (**Chapters 4-6**).

X-ray Photoelectron Spectroscopy (XPS)

Additionally, XPS is used to obtain information regarding the chemical composition of the surfaces studied. The use of XPS in terms of the experiments at hand is limited to direct confirmation of changes in structure observed in RAIR spectra. As a photon beam technique, XPS takes advantage of the photoelectric effect to probe the elements present on surfaces and their immediate chemical environment. In principle, the sample is bombarded with high-energy photons of known frequency which interact with core electrons of atoms in the sample. Energy conservation requires that electrons ejected from an atom have kinetic energy equal to the difference between the photon energy and binding energy, and spectrometer work function, given by the following equation: [1,4]

$$KE = h\upsilon - E_B - \phi_{spec} \quad \textbf{(2-1)}$$

As each element has unique core electron binding energies, this technique provides for direct elemental analysis of the surface. Additionally, bonds existing between two or more atoms perturb the binding energy of the atoms' core electrons on the order of a few eV, and the presence of these chemical shifts can empirically characterize an atom's immediate chemical environment at the surface.

The experimental setup consists of an achromatic Al Kα X-ray source (04-153, Perkin Elmer) positioned at a 45° angle incident upon the sample, emitting X-rays with average energy 1486.6

eV. The electrons emitted from the sample are focused and detected by a cylindrical mirror analyzer (15-255G, Perkin Elmer) and referenced by assignment of the characteristic $4f_{5/2}$ and $4f_{7/2}$ photoemission peaks of gold at 87.63 eV and 83.95 eV, respectively.[5] It is important to note that X-ray irradiation and any secondary electrons generated from the surface can disrupt features of the thin films discussed in this thesis *via* bond cleavage, desorption, and disordering. Thus, XPS was always performed on a pristine film used only for initial characterization, or on an exposed film at the end of an experiment.

The Supersonic Beamline

The beamline consists of three chambers: one source chamber, followed by two stages of differential pumping prior to entering the main chamber. A schematic is given in **Figure 2-3**. Once a source gas exits the nozzle, the stream supersonically expands into the high-vacuum region of the source chamber (~5 x 10^{-7} Torr with no source gas) maintained by an 8000 L s^{-1} diffusion pump (VHS-400, Varian), with foreline backed by a 19 L s^{-1} single-stage rotary vane pump (Duo 65 MC, Pfeiffer Vacuum). During operation of the source, a Roots blower with a maximum flow rate of 175 L s^{-1} (WKP 500AM, Pfeiffer Vacuum) accompanies this setup to account for the gas load, providing extra compression.

The collision-free centerline of the expansion is selected out by the 0.5 mm aperture of a nickel conical skimmer (Gentry) located ~1 cm from the source aperture, whereupon it enters the first high-vacuum (10^{-7} Torr) differential chamber (1DC), passes through a 3.4 mm aperture into the second high-vacuum (10^{-8} Torr) differential chamber (2DC), and exits into the main chamber through a 2.3 mm aperture. The 1DC's vacuum is maintained by a 1200 L s^{-1} diffusion pump (VHS-4, Varian), while the 2DC's vacuum is maintained by a 230 L s^{-1} turbomolecular pump (TPU 240, Pfeiffer Vacuum). Both of these chambers empty into a shared foreline backed by a 3

Figure 2-3

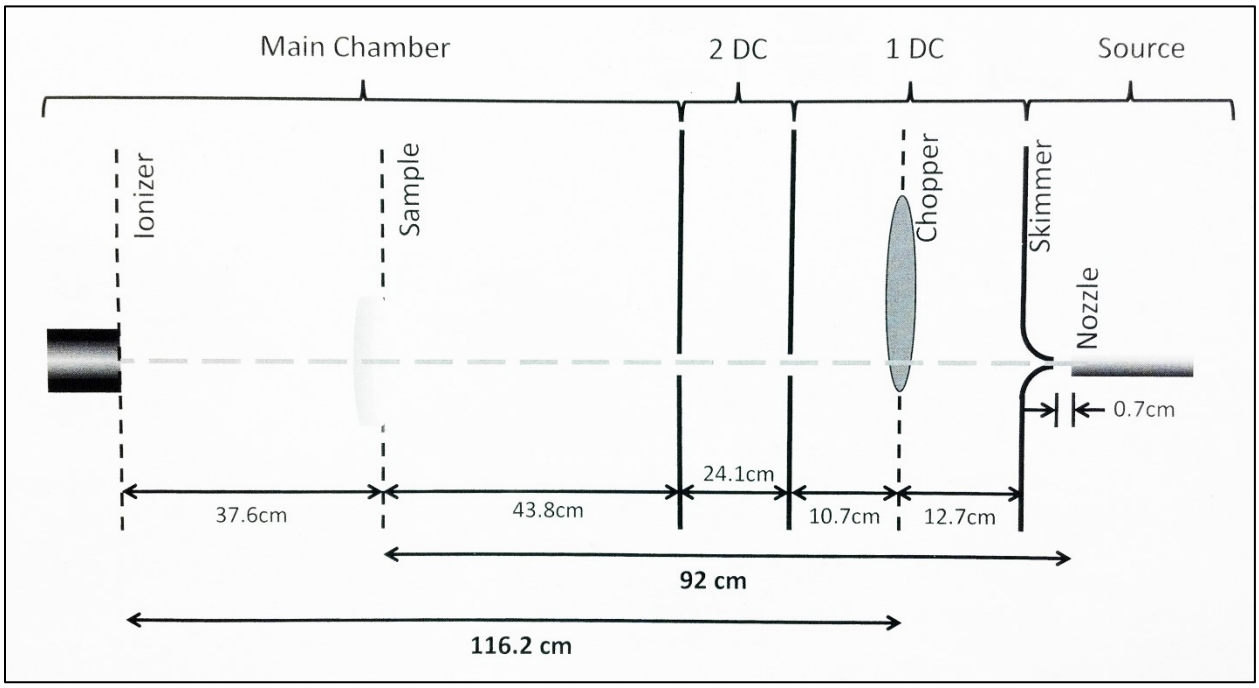

Schematic of supersonic beamline. *The instrumentation of the differentially-pumped beamline exiting into the main UHV chamber, complete with measured distances. The beam can be modulated using the mechanical chopper in the first differential chamber, or 1DC.*

L s^{-1} two-stage rotary vane pump (Duo 10 M, Pfeiffer Vacuum). The 1DC chamber contains a solenoid-operated beam flag located just before the exiting aperture to allow for precise control of beam's exposure to the main chamber.

Time-of-Flight (TOF) Analysis of Supersonic Beams

The velocity distributions of the components in a particular stream generated in the beamline are measured by an in-line quadrupole mass spectrometer (QMS; QMG 112, Balzers) located in the main chamber. The beam can be modulated by a variable-speed mechanical chopping wheel located in the 1DC, operated at 100 Hz for all studies discussed in this thesis. The wheel is driven by a hysteresis-synchronous motor powered by an audio amplifier stereo receiver (XGA-3000, Gemini). The driving signal is produced by a signal generator (651A Test Oscillator, Hewlett-Packard) and split by an RC circuit to produce two 90° out-of-phase signals amplified by the stereo receiver

The chopper wheel has patterns cut for a 50% duty-cycle square waveform, a 50% duty-cycle 511-bit pseudorandom sequence (for use in cross-correlation characterizations outside the context of this thesis), and a 1% duty-cycle. It is mounted on a linear motion vacuum feedthrough, with *z*-translation controlled by micrometer, allowing for the beam's modulation by any of the patterns cut into the wheel, as well as for removing the wheel from the beam's path during experiments.

The aforementioned 1% duty-cycle modulation is used for the TOF studies of the beam's components, chopping the beam into packets that travel 116.2 cm to the electron bombardment ionizer of the QMS, detected and counted by a multi-channel analyzer (MCA) in a computer. Counting is triggered by an infrared LED that passes through the same slit as the skimmed beam and detected by a photodiode operational amplifier detector (United Detector Technologies).

Figure 2-4 shows one example of the raw output from detection by the QMS at m/z = 32 and its conversion to a velocity distribution. The raw signal intensity in counts is converted to counts per second (cps), given knowledge of the counting bin's size as set by the MCA. The TOF output of a single component of the beam in the time domain is then converted to the velocity domain *via* a $1/v^2$Jacobian transformation:

$$n(t)dt = n\left(\frac{L}{t}\right)dv(t) = -\frac{L}{t^2}n(v)dt \quad \textbf{(2-2)}$$

$$n(v) \sim n(t)/v^2 \quad \textbf{(2-3)}$$

Given that the QMA's detector is sensitive to number density instead of flux, the ionization efficiency is inversely proportional to the velocity, so the number density in the time domain must be divided by the velocity to obtain the true response from the detector:

$$n(v) \sim n(t)/v^2 = [n_{\text{den}}(t)/v]/v^2 = n_{\text{den}}(t)/v^3 \quad \textbf{(2-4)}$$

The above analysis assumes modulation by an infinitely thin slit. Normally, the slit width must be deconvoluted from the distribution, but for beams produced for the experiments in this thesis, the slit width was negligible compared to the distribution widths. This deconvolution procedure was therefore omitted from analyses. The resultant data are ultimately fit to the theoretical velocity distribution for a supersonic molecular beam to obtain the average velocity:

$$n(v) \sim v^3 exp\left[-\frac{(v-v_0)^2}{\alpha^2}\right] \quad \textbf{(2-5)}$$

Determination of Flux

The flux of a stream containing only one component can be directly measured from the pressure rise, ΔP, in the main chamber when the beam is opened, *via* inversion of the Knudsen equation:

Figure 2-4

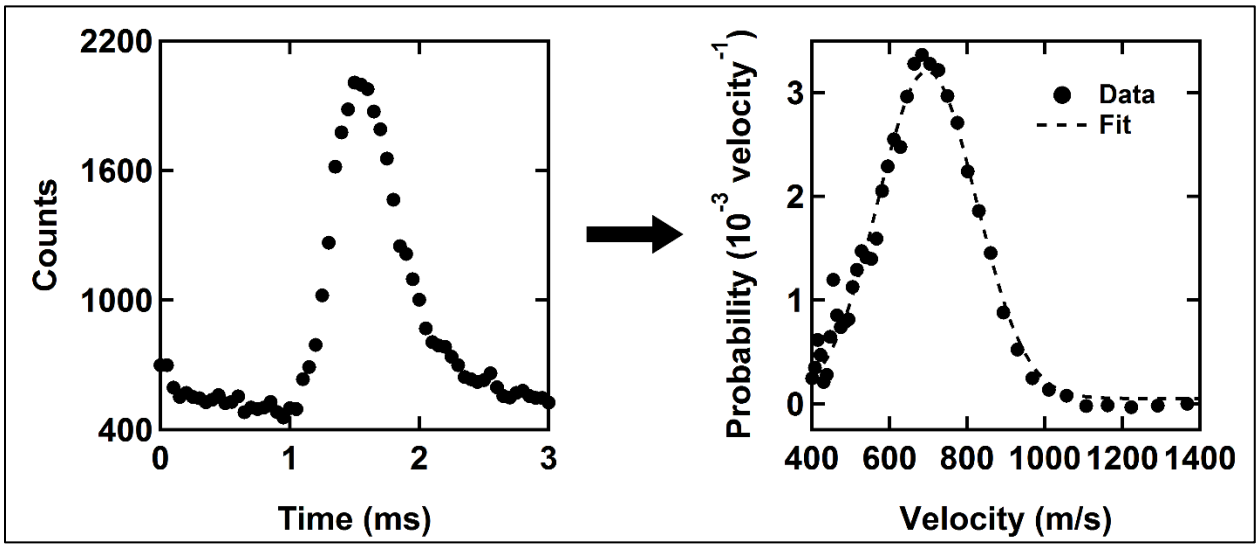

An example of raw TOF data converted to a velocity distribution. *The ordinate values are corrected via the appropriate Jacobian transformation (see text) as well as for detection method. This particular velocity distribution (right) has an average velocity of ~700 m* s^{-1}*, with a width of 43%.*

$$\Phi = \frac{Q}{V} = \frac{Q}{kT \cdot A} \Delta P \cdot X \quad \textbf{(2-6)}$$

In **Equation 2-6**, Q is the pumping speed of the pump, k is Boltzmann's constant, T is temperature, and A is the cross-sectional area of the stream at the point where it impinges upon the sample (4 mm; defined by the geometry of the collimating apertures). A correction factor, X, is required to account for differences in total ionization cross section by the ion gauge of the atom or molecule in question, relative to nitrogen. Q takes both the pumping speed, Q', and conductance, C, of the tube leading to the pump, which is determined from the geometry of the pipe (uniform cylinder) assuming molecular flow:

$$C = \frac{8}{3\sqrt{\pi}} \left(\frac{2kT}{m}\right)^{\frac{1}{2}} \left(\frac{D^3}{L}\right) \quad \textbf{(2-7)}$$

In **Equation 2-7**, m is the mass of the gaseous atom or molecule, D is the diameter of the tube in cm, and L is its length in cm. At the time of writing, C is measured to be 340 ± 60 L s^{-1} for the main chamber. Q is then calculated from **Equation 2-8**:

$$\frac{1}{Q} = \frac{1}{Q'} + \frac{1}{C} \quad \textbf{(2-8)}$$

For the multicomponent mixtures referenced in this thesis, the flux of any one component is therefore calibrated using **Equation 2-6** by first calculating the flux of a stream containing only that component, and linearly relating the flux to either the change in pressure measured by the main chamber's RGA at the component's parent mass, or to the area under its TOF curve (corrected for differential velocity detection, $n_{\mathrm{den}}(t)$ in **Equation 2-4**). Thus, during exposure of the multicomponent mixture, measurement of either of these two values is directly related to the flux through a simple conversion factor. **Figure 2-5** shows an example of this extrapolation done for O_2.

Figure 2-5

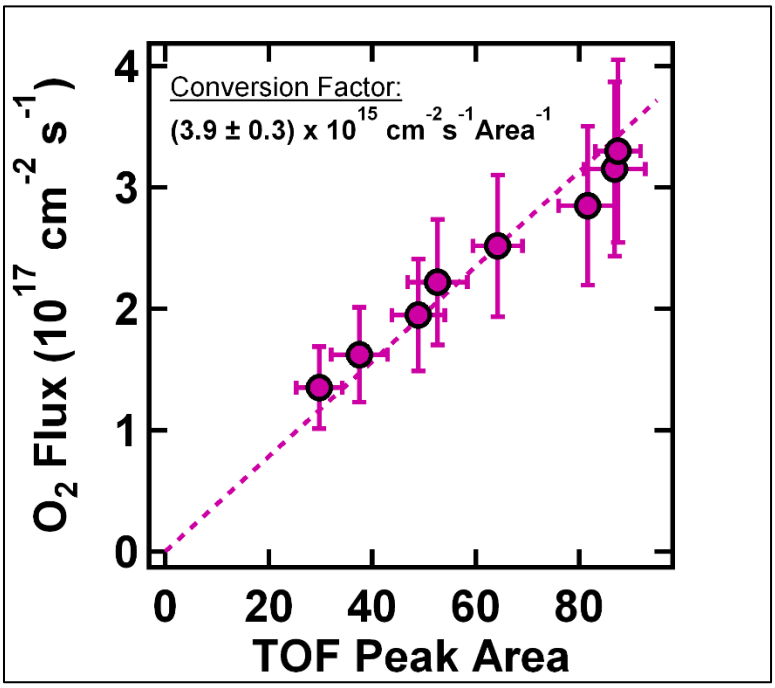

An example of a flux calibration for a neat O_2 beam. *Details regarding how the ordinate values are measured are given in the text.*

Radio Frequency (RF) Plasma Source

An important function of this instrument's beamline is the capability of generating intense beams of atomic species. For example, atomic oxygen in its ground electronic state, $O(^3P)$, is used in the experiments described in **Chapters 3, 5 and 6**. This requires the use of a source[6] capable of generating intense plasmas in the gas just before its supersonic expansion into the high vacuum of the source chamber. A gas mixture of 5% O_2 in Ne is fed into the custom-designed, water-cooled quartz nozzle of the plasma source, where a radio frequency discharge focused just behind the nozzle ignites the gas, causing a fraction of the O_2 to decompose to $O(^3P)$. In addition to $O(^3P)$, discharge of this mixture is capable of producing $O(^1D_2)$, $O_2(^1\Delta_g)$, O_2^+, O^+, Ne^+, and metastable Ne. A pair of 2 kV cm^{-1} deflection plates located in the 1DC chamber remove any unwanted ionic species from the stream, although in practice, ionic species were not detected in the stream under any conditions used in this thesis. Most $O(^1D_2)$ potentially formed in the discharge is quenched by Ne, but again, the RF power and stagnation pressures quoted in this thesis do not generate a significant intensity of $O(^1D_2)$.[7,8] Under this same logic, the flux of $O_2(^1\Delta_g)$ is equally negligible.[9]

Therefore, for all experiments utilizing modification of a surface with a beam produced using this source, control experiments are performed with a pure Ne plasma to rule out modification by metastable Ne in the beam. In all relevant experiments addressed in this thesis (**Chapters 3, 5, 6**), a pure Ne discharge, prepared under identical conditions used for the mixture, did not modify the sample. Thus, the main constituents of the product stream produced from this source are Ne, O_2, and $O(^3P)$.

This beam source routinely produces O_2 dissociation ranging from 30-60%. This is quantified for each beam by measuring the absolute intensity of signals in the QMS at m/z = 16 and m/z = 32 with and without the RF discharge, since the signal at m/z = 16 with the discharge on has

contributions not only from the O_2 dissociated in the plasma, but also from dissociatively-detached O_2 formed by electron bombardment in the QMS (with reaction cross-section σ_D):

$$O_2 + e^- \xrightarrow{\sigma_D} O^+ + O + 2e^- \quad \textbf{(2-9)}$$

The number density ratio, R, of O to O_2 in the beam with the discharge on is calculated from **Equation 2-10**:

$$R = \frac{N_O}{N_{O_2}} = \frac{\sigma_D}{\sigma_O}\left(\frac{I_O/I_{O_2}}{\eta} - 1\right) \quad \textbf{(2-10)}$$

In this equation, I_O and I_{O_2} are the measured intensities of O and O_2 in the beam with the discharge on, while η is the ratio of I_O to I_{O_2} observed with the discharge off. σ_O is the reaction cross-section of ionization of O(^{3}P) by electron bombardment:

$$O + e^- \xrightarrow{\sigma_O} O^+ + 2e^- \quad \textbf{(2-11)}$$

Calculation of O(^{3}P) flux is then performed using R and the calibrated O_2 flux from the beam.

Stainless-Steel Source

A different source is used for the experiments in **Chapter 4**, where fine control over the average translational kinetic energy of the components and the energy distribution's width are desired. The nozzle is machined from a blank ¼" VCR gland, with Mo or Pt pinholes (3.04 mm dia., SPI Supplies) inserted into the gland. Resistively-heatable wire (1 Nc I 10, Thermocoax) is tightly coiled along the length of the gland and secured by a thin Ta sheet to promote efficient, even heating. A Type-K thermocouple is spot-welded to the tip of the gland beside the pinhole exit and used to control the nozzle temperature *via* a feedback loop from a temperature controller (CN76000, Omega). With this setup, the nozzle can be heated from room temperature to ~1200 K.

Sample Manipulation and Preparation

All experiments in this thesis were performed using single-crystal Au(111) as the substrate, except for **Chapter 3** where polycrystalline Au(111) films on mica were used. Au(111) is a convenient substrate due to its high reflectivity (RAIRS) and resistance to oxidation. This substrate is secured to a six-axis (*x*-, *y*-, and *z*-translation; *x*- and *y*-azimuth tilt; polar rotation) manipulator in the main chamber. The crystal is clipped onto the sample plate of a modified commercial resistive heater assembly (HST, Thermo Vacuum Generators) attached to the sample holder at the bottom of the manipulator (SH2, Thermo Vacuum Generators).

The first modification, used in **Chapter 3**, was a "dual-sample" Mo plate machined in-house, identical to the commercial plate except for being ~1.75 cm longer. This allowed for a clean Au/mica substrate to be secured in vacuum, used as the background reference spectrum for RAIRS of prepared SAMs. This substrate was secured by Ta clips bent from foil and spot-welded to the plate.

The second modification, used in the rest of the chapters, was a sample plate with the same dimensions as the commercial plate, instead made of oxygen-free high-conductivity (OFHC) copper to supply superior cooling power to samples. Sandwiched between the Au(111) crystal and the OFHC plate was a piece of gold foil to prevent alloying of the crystal when the sample plate was heated. In contact with this sample was a polished OFHC copper plate welded under argon to a pair of OFHC copper braids secured to a small stainless-steel dewar, with intake and output lines for the dewar exiting vacuum through UHV feedthroughs in the conflat (CF) flange of the manipulator. This dewar, kept filled with liquid nitrogen, provided cooling power to the sample holder. Combined with resistive heating of a filament directly behind the sample plate, the crystal temperature could be reliably held at any point within the range 120-800 K, as measured by a

Type-K thermocouple affixed to the plate beside the crystal. This plate (as well as the dual-sample plate), was electrically isolated from the rest of the mount and the chamber, grounded by a thin wire connected to a BNC feedthrough also on the manipulator's CF flange.

Liquid Helium Cryostat Manipulator

An upgrade to the cooling capacity of a sample was completed in order to outfit the instrument with the ability to do future cryogenic research. While not mentioned, a few of the experiments in **Chapter 6** made use of this manipulator despite the superior cooling power being unnecessary. The customized manipulator was modified from a commercial recirculating liquid helium cryostat (204P and DMX-20B, Advanced Research Systems). In order to conform to the instrumentation present in the UHV chamber, the sample holder is mounted onto the end of a long OFHC copper extension. The nickel-plated radiation shield was faced at the bottom to provide clearance for the glancing IR radiation from RAIRS as well as the chamber's CMA used in XPS. Again, the sample is electrically isolated, this time sitting on a *c*-axis sapphire plate, and can be grounded in the same manner used for the previous manipulator.

Allowing for polar rotation of the sample is accomplished by attaching the cryostat to the chamber *via* differentially-pumped rotary seal (RNN-400, Thermionics Vacuum Products). Differential pumping is required for maintaining UHV while rotating, the "chambers" being the spaces between the pair of Teflon seals.

Crystal Preparation

After any reaction of a deposited film, the underlying Au(111) crystal substrate was sputtered and thermally annealed in vacuum. Instead of sputter-annealing cycles, the crystal was sputtered by 1 kV Ar^+ ions (from a ~5 x 10^{-5} Torr Ar backfill into the chamber) directed at the crystal by an ion

gun while the surface temperature was held at 773 K, typically for 10-15 minutes. Cleanliness was confirmed by high-resolution XPS scans of the surface showing no trace of carbon or oxygen.

Chapter 3

Formation of Stabilized Ketene Intermediates in the Reaction of O(^{3}P) with Oligo(Phenylene Ethynylene) Thiolate Self-Assembled Monolayers on Au(111)

We have taken steps to develop a methodology for quantifying the kinetics and dynamics of bimolecular reactions through spectroscopic monitoring of reactants and products during exposure of well-ordered self-assembled monolayers to supersonic beams of atomic reagents. The use of a SAM stabilizes highly energetic intermediates formed from bimolecular reactions at the vacuum/film interface due to rapid thermal equilibration with the SAM matrix that are otherwise not readily observed under single-collision conditions in the gas phase. In this paper we will discuss the elucidation of the mechanistic details for the fundamental reaction between O(^{3}P) and phenyl-substituted alkyne bonds by monitoring chemical and structural changes in an oligo(phenylene ethynylene) SAM reacting with O(^{3}P) under collision conditions having specified initial reaction orientation. Utilizing time-resolved reflection-absorption infrared spectroscopy (RAIRS) and scanning tunneling microscopy (STM) under ultrahigh vacuum conditions, we have confirmed electrophilic addition of O(^{3}P) onto the alkyne moieties, resulting in formation of a ketene intermediate via phenyl migration. Under single-collision conditions in the gas phase the vibrationally-excited ketene intermediate cleaves to release CO. In contrast to this, formation of the condensed-phase stabilized singlet ketene is observed using RAIRS. Moreover, we have observed that the phenyl ring at the vacuum/film interface significantly cants towards the substrate

plane as a result of this reaction. STM images of the SAM taken before and after O(^{3}P) exposure show an expansion of the ordered lattice resulting from formation of the new nonlinear molecular structures within the SAM and the reaction preferentially propagates along the lattice direction of the monolayer domain. This approach of using pre-oriented reactive molecules in ordered self-assembled monolayers in combination with angle- and velocity-selected energetic reagents provides a general approach for probing geometric constraints associated with reaction dynamics for a wide range of chemical reactions.

Introduction

At the heart of chemistry lies an initiative to both elucidate and predict the behavior of chemical reactions through analysis of the complex molecular dynamics taking place. Direct study of reaction mechanisms, however, is naturally precluded by establishment of some degree of control over the intended pathways. Historically, this has been accomplished in the gas phase through either excitation of relevant internal states of reacting molecules[11–14] or controlling their mutual orientation.[15] Early examples in the literature of the latter method include alignment of polar molecules in molecular beams using either hexapole or "brute-force" techniques.[16,17]

Our goal is to apply this same notion of stereodynamic control by dosing reactive species prepared in a molecular beam to the exposed interface of a self-assembled monolayer. SAMs offer unique opportunities to probe the mechanisms of reactions at interfaces due to their well-defined, ordered structures and chemical stability, and organothiolates on gold are a classically robust system of choice for studying reactions of organic matter.[18] Their self-assembly in solution is often simple and effective, utilizing precursors with nearly any functional terminus of choice.[19,20] The use of a SAM surface as an ensemble of reactants is also advantageous due to its ability to rapidly dissipate excess energy.[21–23] Highly energetic intermediates that fall apart or further react in the gas phase

can instead be stabilized at the interface, a process akin to collisional stabilization in the gas phase at high pressures. Utilizing reflective spectroscopic techniques and high-resolution scanning probe microscopy, we are uniquely situated to successfully characterize reactions occurring at these interfaces in both real time and real space.

We aim to directly observe reaction products in the foundational reactions of $O(^3P)$ with unsaturated hydrocarbons using this technique, specifically considering addition onto phenyl-substituted alkynes. Reactions with phenylacetylene, 2-propynylbenzene, and biphenylacetylene have previously been experimentally characterized, with energetic barriers associated with $O(^3P)$ addition onto the side chains measured to be low (< 8 kJ mol^{-1}) compared with the phenyl rings (~20 kJ mol^{-1}).[24,25] Specifically in the case of biphenylacetylene, Eichholtz *et al.* reported the formation of biphenyl as a main product and proposed a mechanism for its formation through, in part, decomposition of a vibrationally-excited biphenylketene intermediate via phenyl ring migration to release CO.[15] This mechanism is supported by experimental[26–28] and theoretical[29–33] studies of analogous reactions with acetylene and other substituted alkynes where CO formation results from cleavage of singlet ketenes formed from intersystem crossing of long-lived triplet ketocarbenes. These observations are also in line with experimental studies of $O(^3P)$ addition onto ethylene, where intersystem crossing is observed to contribute heavily to overall product formation.[34,35]

Ketenes have previously been directly observed in studies of acetylene/$O(^3P)$ reactions in low-temperature solid matrices[36] and at high pressures,[37] so the ability to directly observe the biphenylketene intermediate expected in this reaction via rapid thermal equilibration of the reaction complex with the SAM matrix can be expected. The SAMs used in this study were composed of oligo(phenylene ethynylene)thiolate (oPE) molecules which have previously been

shown to self-assemble onto Au(111) in solution to form well-ordered, densely-packed monolayers of upright molecules.[38–40] This surface yields an exposed interface of phenyl-substituted alkyne bonds.

Experimental Details

SAM Preparation

oPE-SAMs were prepared on commercially-fabricated Au(111) substrates deposited onto mica (1.1 cm x 1.0 cm), obtained from Agilent Technologies. These substrates were cleaned in a commercial UV/O_3 cleaning unit for two hours, rinsed thoroughly with ethanol, and dried under a stream of pure nitrogen prior to immersion into a solution containing the oPE-SAM precursor.

2 mg of *S*-[4-[2-[4-(2-Phenylethynyl)phenyl]ethynyl]phenyl]thioacetate (oPE) and 25 μL of 30%(w/v) aqueous NH_3 (both obtained from Sigma-Aldrich) were diluted to 10 mL in a 2:1 acetone/ethanol mixture to form a 0.5 mM thiolate solution, similar to literature preparation.[41] A thioacetate precursor was used instead of the free thiol to prevent side-reactions with functional groups in the SAM precursor backbone. Since SAMs formed from thioacetates are inferior in quality compared to those formed from free thiols,[42] the acetate protecting group is removed via base-catalyzed hydrolysis initiated by the addition of NH_3. The prepared solutions were left to sit at room temperature, with 30 minutes being sufficient for complete deprotection,[43] and the cleaned Au(111) substrates were immersed into these solutions for 24 hours at 60 ºC, followed by subsequent washes in fresh 2:1 acetone/ethanol and pure ethanol. This method routinely produces SAMs of high quality.[38,42]

Molecular Beam/RAIRS

All reactions were carried out in a molecular beam scattering apparatus that consisted of an ultra-high vacuum chamber and supersonic molecular beam. **Chapter 2** describes this instrument in great detail, so only a brief description including the relevant modifications is included here.

A radio-frequency plasma source was used to generate a supersonic atomic oxygen beam formed by igniting and expanding a gas mixture of 5% O_2 in Neon through a water-cooled quartz nozzle. The beam is characterized using time-of-flight techniques to determine both the extent of O_2 dissociation and the average kinetic energy of the resultant $O(^3P)$ atoms. Typical experimental conditions yield an $O(^3P)$ flux of 9×10^{13} atoms cm^{-2} s^{-1}, impinging upon SAM surfaces at normal incidence with an average kinetic energy of 9 kJ mol^{-1}. The energy was chosen to discourage side reactions, namely the addition of $O(^3P)$ onto the phenyl rings of oPE-SAM occurring near 18 kJ mol^{-1}.[25] Flux is determined from monitoring the change in pressure within the reaction chamber when it is open to the incoming beam, given that the extent of O_2 dissociation is known.

In situ time-resolved Fourier transform reflection-absorption infrared spectroscopy (RAIRS) is accomplished through the use of incoming infrared radiation from a commercial IR spectrometer (Nicolet 6700), which is polarized perpendicular to the substrate of interest prior to reflection at a 75º incidence angle and collected with a liquid-nitrogen-cooled HgCdTe detector. Spectra were averages of 1000 scans at a 2 cm^{-1} resolution taken in reference to a clean Au(111)/mica substrate, with peaks fit to Gaussian line shapes with cubic polynomial baselines using a nonlinear least-squares routine. The time-resolved nature of this technique stems from the ability to block the incoming $O(^3P)$ with the beam flag, allowing for precise control over the amount of time the SAM is exposed to incoming $O(^3P)$.

UHV-STM

All scanning tunneling microscopy (STM) images were taken at room temperature in a commercial UHV-STM system (UHV 300 from RHK Technology, Inc.), with a base pressure of $1x10^{-10}$ Torr. Reacted SAMs were exposed to the molecular beam in the RAIRS system before transferring through air to the STM system, with total exposure to air lasting less than ten minutes. STM images were taken with typical scanning parameters of ±0.7 V and 40-50 pA. Fresh oPE-SAM samples were prepared for each reacted surface imaged.

Results and Discussion

SAM Characterization

RAIRS signals detailed in **Figure 3-1** show relevant example absorption bands of oPE-SAM on polycrystalline gold substrates, the locations of which are in good agreement with literature.[39] Due to the surface selection rule, only vibrational modes with dipole moments perpendicular to the surface are observable,[2] allowing inferences regarding molecular orientation to be made. The average tilt angle of the molecules relative to the surface normal was not quantitatively characterized in this study, however the most intense peaks observed correspond to modes with transition dipole moments parallel to the molecular axis. This is consistent with the oPE molecules being anchored with their molecular axes nearly perpendicular to the substrate, which is expected since SAMs composed of these and similar oligophenylene molecules have been reported to exhibit small tilt angles relative to the surface normal.[38,40,44–47]

Scanning tunneling microscopy images of the pristine oPE-SAM are shown in **Figure 3-2**. The oPE molecules form highly-ordered domains composed of two distinct close-packed structures: (1) a $(\sqrt{3} \times 2\sqrt{3})R30^{o}$ structure commensurate with the underlying Au(111) surface, containing

Figure 3-1

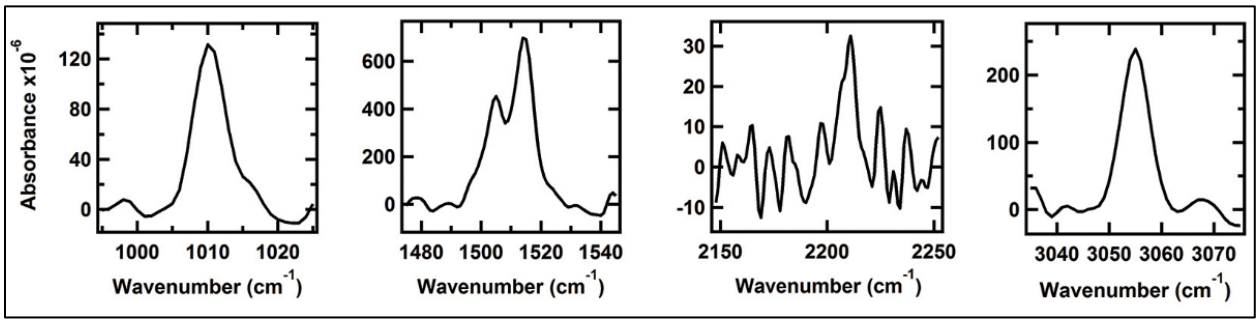

Relevant vibrational modes of prepared oPE-SAM as measured by RAIRS. *(from left to right) C-C bending mode at 1010 cm^{-1}, C=C semicircle stretches at 1504 and 1514 cm^{-1}, alkyne stretching mode at 2210 cm^{-1}, C-H stretching mode at 3055 cm^{-1}. All modes are parallel to the molecular axis.*

Figure 3-2

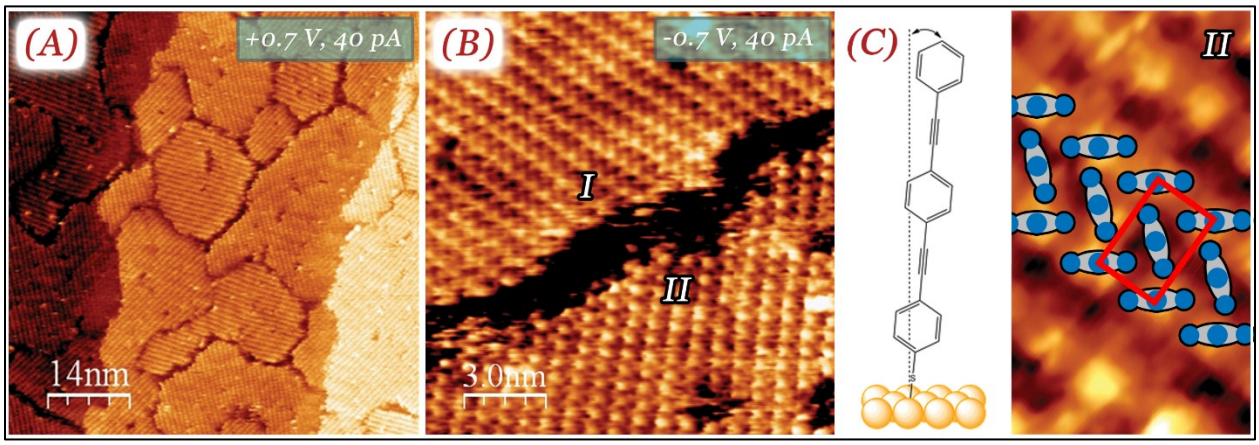

Structure of oPE-SAM as determined by UHV-STM. (a) *oPE readily forms an ordered monolayer with large domains on Au(111) in solution.* ***(b)*** *The monolayer consists of two types of domains: a "commensurate" (I) and "incommensurate" (II) structure, both of which have been observed previously in the literature. We observe that the overall structure of the monolayer is dominated (~75%) by the "incommensurate" domains.* ***(c)*** *The oPE molecules are anchored with their molecular axes nearly perpendicular to the Au(111) substrate. Intermolecular interactions are the main driving force for this ordering, resulting in a herringbone-like packing on the surface.*

lattice constants of a = 5.0 Å and b = 9.7 Å and observed by Sita *et al.*[39] and (2) an incommensurate structure with a rectangular lattice of a = 5.5 Å and b = 8.0 Å observed by Liu *et al.*[40] While both of these domains coexist on the surface and are shown in **Figure 3-2(*b*)**, we observe ~75% of the monolayer is composed of the incommensurate structure under our preparation conditions. Additionally, this structure remains constant throughout a bias voltage range of ±1 V.

The close-packed oPE molecules are bonded to the underlying Au(111) through the sulfur atom, with the molecular chain standing near-perpendicular to the surface (**Figure 3-2(*c*)**). Adjacent molecules are rotated to maximize π-π interactions between the benzene substituent on neighboring chains, forming a herringbone-styled array of molecules across the domain. The face of the benzene rings located on the same molecular chain are aligned within the same plane and locked into this position by the triple bonds between the carbon atoms; this results in a different structure than self-assembled monolayers composed of biphenylthiolate molecules, in which the orientation of the benzenes are independent from one another and are rotated with respect to each other on the same molecule to minimize steric effects.[48]

The rectangular unit cell is composed of oPE molecules that appear as both bright and dark features in the STM image. Liu *et al.* proposed that the difference in apparent STM height is the result of a change in the electronic structure between oPE molecules bound at different Au(111) lattice sites;[40] however, replicating the unit cell across a bulk-terminated Au(111) surface does not result in consistent binding locations for a given feature (*i.e.* not all "bright" molecules bind at the same Au(111) lattice site). More recently, a number of experimental groups have revealed the presence of gold adatoms at the interface of bulk-terminated Au(111) and thiol-based self-assembled monolayers.[49–53] While STM is unable to image the gold-monolayer interface directly, changes in relative electronic structure across the monolayer surface is detectable and we believe the

rectangular unit cell with bright and dark features is the result of a complex interfacial structure involving bulk-terminated Au(111), gold adatoms, and oPE molecules. Further study of oPE SAM formation is needed to fully explain this observation.

Mechanism of O(^{3}P)/oPE-SAM Reaction

Upon exposure to O(^{3}P), distinct structural changes in the SAM are observed. These changes are summarized in **Figure 3-3**. The most notable is the appearance of a new mode at 2102 cm^{-1} immediately upon exposure of oPE-SAM to O(^{3}P). The peak position is consistent with formation of a ketene, and closely matches that of the C=C=O stretching mode of biphenylketene at 2094 cm^{-1}.[54] Moreover, this is consistent with an expected product of electrophilic addition of O(^{3}P) onto an alkyne bond in oPE. Combined, these observations are congruent with a biphenylketene-like product being formed. In the gas phase, a phenyl shift occurring after addition onto biphenylacetylene results in a highly vibrationally-excited triplet ketene, which cleaves to form CO and a carbene. On the thermally equilibrated surface, however, the excess energy from the reaction can dissipate through the SAM matrix. Additionally, the triplet biradical intermediate is likely stabilized on the surface to the singlet ketene, similar to collisional stabilization by surrounding inert gases in high-pressure gas reactions. While we can make no spectroscopic distinction between the two alkyne bonds of oPE, the argument can nevertheless be made that the alkyne bond closest to the vacuum/film interface is initially the most accessible.

Formation of a nonlinear ketene structure at the vacuum/film interface would naturally result in the canting of the interfacial benzene, given that the other end of the molecule is anchored to the substrate. Concurrent with the appearance of the ketene mode, exposure results in significant decay of the phenyl C-H peak at 3055 cm^{-1} alone; this change is not reciprocated in the rest of oPE-SAM's IR signals. We assign this peak to the C-H stretching mode (20a) of the monosubstituted

Figure 3-3

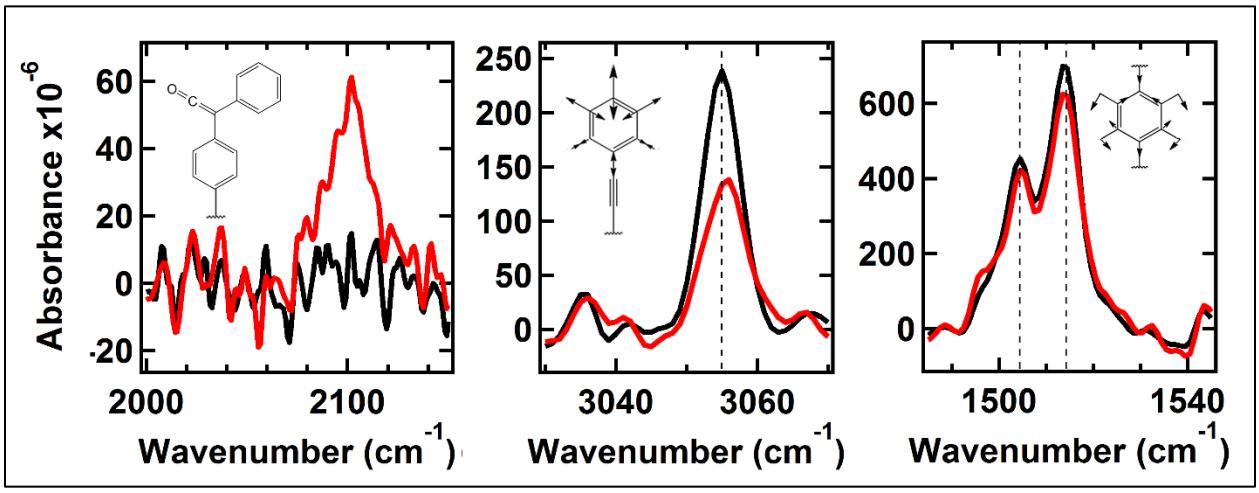

RAIR spectra of oPE-SAM before and after exposure to O(^{3}P). *RAIR spectra of monolayer before (black) and after (red) exposure of ~8 x 10^{15} O(^{3}P) cm^{-2}. New mode associated with ketenyl stretching appears at 2102 cm^{-1} (left), consistent with expected position of a biphenylketene-like moiety. Peak associated with C-H stretching mode of the phenyl ring at the vacuum/film interface (middle) decreases significantly upon exposure of the monolayer to O(^{3}P). Other peaks, such as the C=C semicircle stretching modes (right), remain unchanged at this level of exposure, suggesting that initial exposure results in formation of ketenes, resulting in canting of interfacial phenyl rings' planes towards the substrate, with the rest of the molecular backbone remaining intact.*

benzene of oPE located at the vacuum/film interface.[55] Decay of the 20a mode is attributed to a change in orientation of the phenyl ring plane—and therefore the orientation of the 20a transition dipole moment (TDM)—relative to the surface normal. The decrease supports canting of the ring, resulting in the 20a TDM ending up more parallel to the surface plane. Due to the surface selection rule of RAIRS, the intensity appears smaller due to the decrease in the magnitude of the perpendicular component of the 20a TDM even though the structure is still on the surface. The parallel component is "invisible" since the image dipole induced by the gold surface is equal in magnitude but opposite in direction, effectively cancelling it out.

It is important to address other possible causes for the decrease in C-H mode intensity. Abstraction of hydrogen atoms from the phenyl rings can be ruled out due to the associated high energetic barrier (~60 kJ mol^{-1} for benzene[55]). Due to the persistence of the rest of the modes, oxidation of sulfur headgroups leading to desorption of entire chains does not satisfactorily account for the observed decay. Were this the case, all modes belonging to oPE would decay to the same extent, but the modes associated with C=C semicircle stretches, for example, decay by only a few percent over this same exposure (**Figure 3-3(*c*)**). It is also worth noting that these changes in the SAM take place only when $O(^3P)$ is present in the molecular beam. Control trials using a pure neon discharge or an O_2 gas source, seeded in either helium or neon, without the discharge resulted in no detectable change in the structure of the SAM over similar total exposures. We can thus conclude that the structural changes are directly attributable to the presence of $O(^3P)$.

Based on the above observations, we are able to propose a mechanism for the reaction of $O(^3P)$ with oPE-SAM, a schematic of which is detailed in **Figure 3-4**. Upon dosing $O(^3P)$ onto oPE-SAM, the oxygen atoms react with the alkyne bond closest to the vacuum/film interface first to form a triplet biradical intermediate. This intermediate undergoes a phenyl shift to yield a

Figure 3-4

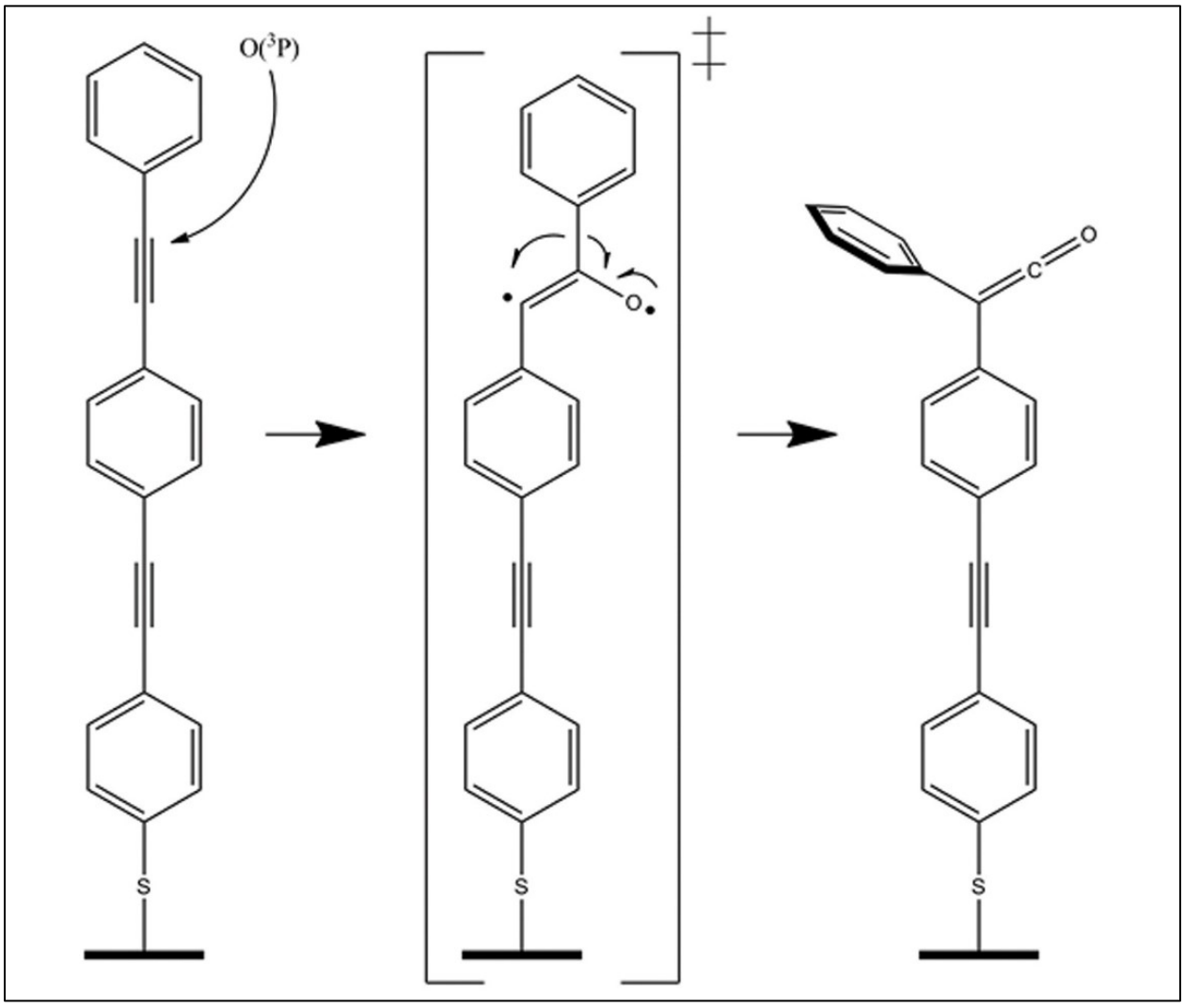

Proposed mechanism for O(^{3}P) reaction with oPE-SAM. *Electrophilic addition of O(^{3}P) onto the alkyne bonds closest to the vacuum/film interface results in formation of a triplet biradical intermediate that undergoes phenyl migration and is stabilized to singlet ketene by rapid equilibration with the SAM matrix.*

vibrationally-excited ketene that is stabilized on the surface to its singlet state, yielding a nonlinear biphenylketene-like moiety located at the vacuum/film interface. This reaction results in the canting of the interfacial phenyl ring's molecular plane towards the substrate.

This mechanism is further corroborated by STM images of reacted oPE-SAM. The STM current, and therefore the "height" in an STM image, is a combination of both the electronic state and the topographic height; STM is not able to directly perform chemical analysis of individual molecules. **Figure 3-5** shows a partially reacted oPE monolayer that contains areas of both reacted and unreacted molecules after ~3 x 10^{15} O(^{3}P) cm^{-2} of exposure. We assign the bright molecules as reacted oPE, based on an increased spacing of the lattice at these particular sites, while the darker molecules approximately retain the pristine lattice spacing. As observed in the RAIRS spectra, upon the formation of the ketene on a reacted molecule, the top benzene rotates downward and becomes more parallel to the gold surface. The reacted molecules appear brighter in the STM image despite the lower topographic height due to the change in the electronic structure upon the addition of the ketene and the resulting exposure of the benzene face. Neighboring unreacted oPE chains tilt and adjust to accommodate the wider reacted molecule, forcing the lattice to expand. **Figure 3-5** also shows a direct comparison between the unreacted and reacted SAM, where the monolayer has maintained a rectangular unit cell and its lattice constants have expanded to a = 6.0 Å and b = 8.5 Å.

We observe in the STM images (**Figure 3-5**) that monolayer reactivity takes place at preferential sites. Interestingly, the reaction does not appear to occur initially at every molecule located along a domain boundary, where the triple bond would be the most exposed to the incident oxygen atoms, before propagating to molecules located in the interior of the domain. Instead we observe that reacted molecules always appear along rows of the unit cell. After the reaction takes place at an

Figure 3-5

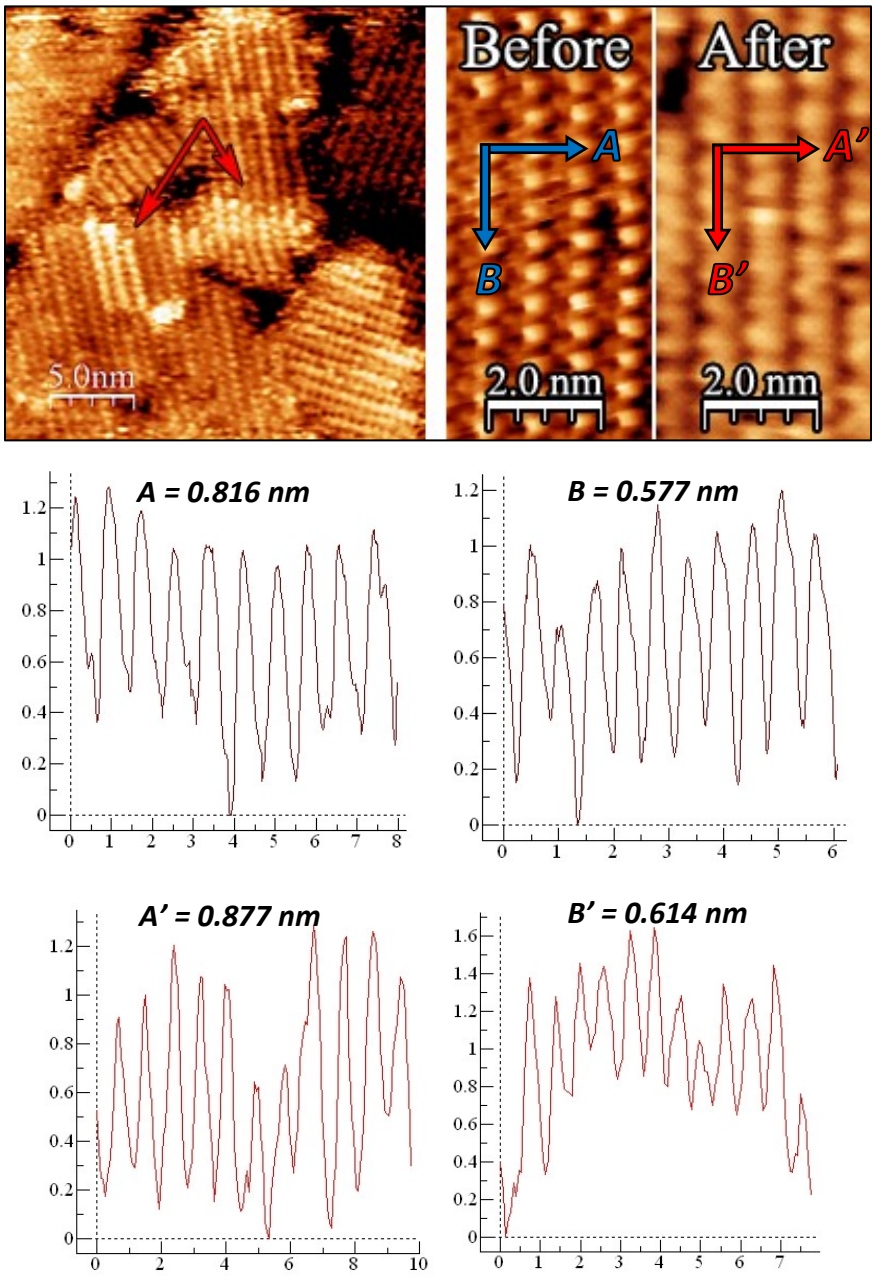

UHV-STM images of oPE-SAM after reaction with O(^{3}P). *STM images (0.7 V, 40 pA) of oPE-SAM after exposure of ~3 x 10^{15} O(^{3}P) cm^{-2} show that this reaction propagates along rows of the unit cell due to greater accessibility of nearby alkyne bonds after canting of the first interfacial phenyl ring. A rectangular lattice is conserved, but with expanded dimensions (0.5 Å along each unit cell direction, see line scans) to accommodate the newly-formed nonlinear structures.*

initial molecule, the benzene rotates parallel to the gold surface and the neighboring molecules expand slightly to accommodate the change in structure. This increases the accessibility of the triple bond on a neighboring molecule to additional oxygen atoms, propagating the reaction along a lattice direction and into the monolayer.

It is worth noting, finally, that continued exposure of oPE-SAM to $O(^3P)$ results in severe disordering of the monolayer. All RAIRS peaks associated with oPE have significantly decayed in intensity by the time the monolayer has been exposed to ~50 x 10^{15} $O(^3P)$ cm^{-2}. This is corroborated with STM images which display no molecular resolution at this level of exposure.

Kinetics of the $O(^3P)$/oPE-SAM Reaction

Appearance of the ketene mode, while reproducible, yields an IR signature that is weak in intensity. Additionally, ketenes formed may undergo further reaction with $O(^3P)$ or O_2 as exposure continues. We have therefore monitored the kinetics of the reaction by characterizing the decay of the stronger 20a mode as a function of total exposure, detailed in **Figure 3-6**, which follows a first-order decay. As exposure increases, the intensity of this mode clearly does not approach zero, instead decaying to a value roughly 25% that of the original intensity. This observation agrees well with the proposed mechanism. Assuming the oPE chain is nearly perpendicular to the substrate, formation of the ketene results in the angle between surface normal and the 20a TDM increasing from ~0° to ~60°. This results in the magnitude of the perpendicular component of the TDM decreasing to roughly one-half its original value. Given intensity is proportional to the square of the TDM's magnitude, the relative intensity of the 20a mode should be roughly one-fourth its initial value.

Taking into account the above points, we can assert that the total signal prior to exposure represents a fraction of remaining interfacial alkyne bonds of 100%. Additionally, the total signal as exposure

Figure 3-6

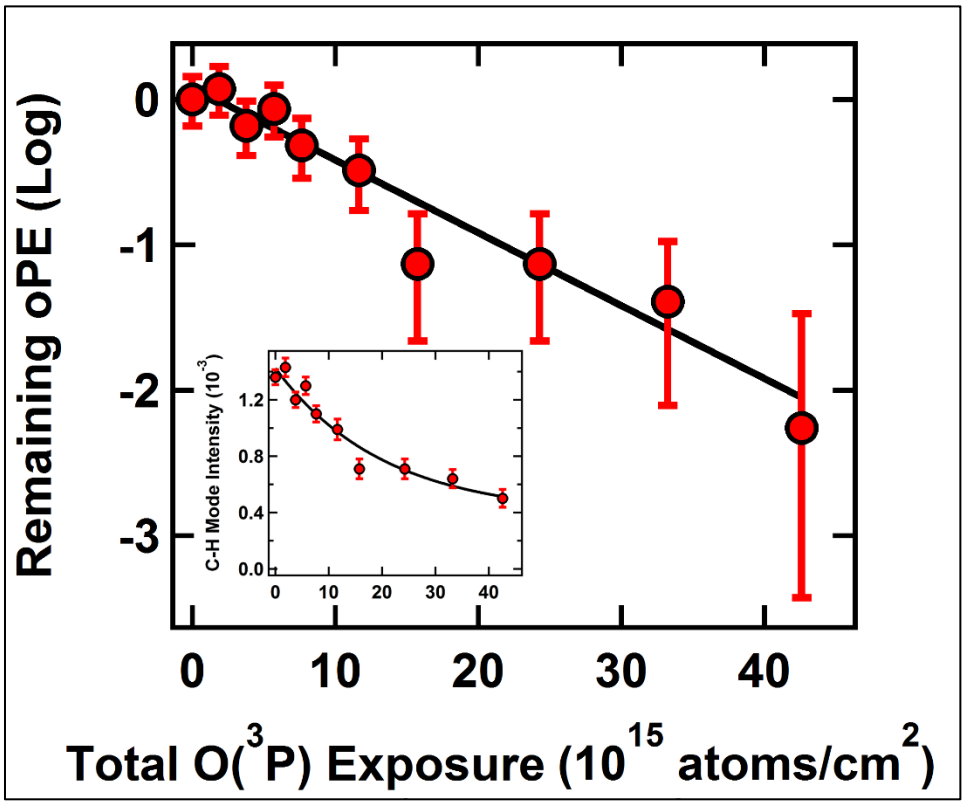

O(^{3}P) + oPE-SAM reaction kinetics. *Plotting the log of remaining unreacted oPE versus total O(^{3}P) exposure yields a linear trend. Fitting the data to a Langmuirian model results in a reaction probability of 7 ± 2%. These data were derived from the decay of the C-H stretching mode intensity at 3055 cm^{-1} (inset), which tends towards ~25% of its original intensity given that the decay is a change in orientation of the interfacial phenyl ring relative to the substrate and not entire removal of the structure.*

approaches infinity approximates a remaining fraction of zero. At any point in between, the total 20a intensity is approximately a combination of these two values:

$$I_{tot} = I_{100\%}\theta + I_{0\%}(1-\theta) \quad \textbf{(3-1)}$$

In **Equation 3-1**, θ is the aforementioned fraction; each data point can be converted to a remaining fraction. Plotting the natural log of this fraction versus the total O(^{3}P) exposure yields a linear decay, which fits well to a first-order Langmuirian model for the rate of O(^{3}P) addition onto the alkyne bond located closest to the vacuum/film interface. This allows for estimation of the initial reaction probability, γ_o:[56]

$$\ln\theta = -(\gamma_o/4A)\Phi \quad \textbf{(3-2)}$$

In **Equation 3-2**, Φ is the total exposure of O(^{3}P), and A is the average density of oPE molecules on the surface. A weighted linear least-squares fit to the data yields an initial reaction probability of 7 ± 2%. The average surface density, A, was estimated from the STM data, where the commensurate (~25%) and incommensurate (~75%) structure unit cells are calculated to contain 2 molecules per 44 ± 1 Å^2 and 48 ± 1 Å^2, respectively.

Use of the SAM as an ensemble of reactants provides a framework for controlling how reactants encounter each other in real space. The barrier for addition onto the alkyne bond of biphenylacetylene in the gas phase was measured by Eichholtz *et al.* to be 0.6 kJ mol^{-1}.[25] Collisions between O(^{3}P) and oPE-SAM occur at the phenyl rings decorating the vacuum/film interface, where no reaction is observed to occur due to unfavorable energetics. Enforcing the majority of collisions to occur under unfavorable conditions yields a low reaction probability despite incident O(^{3}P) atoms having kinetic energies (9 kJ mol^{-1}) far above the energetic barrier. Only when incoming oxygen atoms penetrate the interface can they react with the underlying alkyne bonds.

The most readily-accessible alkyne bonds in oPE-SAM are obscured from direct reaction by the interfacial phenyl rings, and so the addition reaction would not be expected to follow Eley-Rideal kinetics and instead involve incorporation of O(^{3}P) into the SAM. Although gas-surface interactions utilizing oligophenylthiolate SAMs have not been explicitly characterized in the literature, studies of these types of interactions with *n*-alkanethiolate SAMs are plentiful. It is established that lateral motion in these SAMs effectively dissipates energy from collisions of gaseous species.[21–23,57,58] Specifically it has been suggested that, for O(^{3}P) collisions with *n*-alkanethiol SAMs under conditions similar to those outlined in this study, physisorption onto the interface dominates—only ~27% of O(^{3}P) penetrates the interface.[58] It is readily apparent, therefore, that the low reaction probability is a direct result of the change in accessibility of the alkyne bonds in the SAM versus the gas phase. This is also in line with the findings of Eichholtz *et al.*, where the pre-exponential factor for addition onto the alkyne bond was measured to be nearly two orders of magnitude smaller than addition onto the phenyl ring.[25] Enforcing the majority of collisions to occur with the phenyl rings naturally yields a lower probability for the addition reaction. Thus, the ability to stereodynamically control a reaction is demonstrated herein, in this case by restricting the accessibility of a reactive group just below the immediate vacuum/film interface.

Conclusion

Utilizing a combination of *in situ* RAIRS and STM, we have characterized and confirmed the mechanism of the reaction of O(^{3}P) with phenyl-substituted alkynes. *In situ* RAIRS indicates that decay of the phenyl mode at the vacuum/film interface is a result of ketene formation between the top two phenyl rings of oPE-SAM and subsequent canting of the phenyl moiety towards the substrate plane. Subsequent characterization of changes in local topology using STM completes

the picture by establishing that the reaction propagates along rows of the unit cell due to increased accessibility of a neighboring triple bond after one oPE molecule reacts. Kinetic measurements support a mechanism that relies on incorporation of $O(^3P)$ into the SAM matrix in order for reaction to occur. Unfavorable geometric constraints imposed upon the reactants' approach yield low initial reaction probability despite establishing sufficient energetics. Through direct observation of the ketene intermediate, the use of oPE-SAM as a scaffold for an ensemble of oriented reactants proves effective in facilitating rapid thermal equilibration and detection of products not readily observed in the gas phase.

A crucial next step is to utilize SAMs in this manner with reactive groups located directly at the vacuum/film interface. Approaching reactants prepared in a supersonic beam could undergo direct reactions exhibiting Eley-Rideal kinetics given that incoming reactants have translational energies near or above associated energetic barriers. SAMs can readily be prepared with interfacial reactive groups in different orientations with respect to the surface plane, providing a direct route to stereochemical control. This technique is effective for the elucidation of orientation-dependent kinetics, with the added ability to "collisionally stabilize" reactive intermediates not necessarily detectable under, as an example, crossed molecular beam techniques using high collision energies.

Chapter 4

The Ballistic Embedding of Hyperthermal Atoms and Molecules in Amorphous Water Ice

Presented herein is comprehensive work detailing the capture and aggregation of hyperthermal atoms and molecules (CO_2, CF_4, Xe, Kr) by amorphous solid water (ASW) under ultra-high vacuum conditions at 125 K, near the amorphous/crystalline transition. Using time-resolved *in situ* reflection-absorption infrared spectroscopy (RAIRS), the gases prepared in supersonic molecular beams with translational energies above ~3.0 eV are observed to directly embed underneath the vacuum-ice interface to become absorbed within amorphous ice films despite an inability to adsorb at 125 K. Embedding into crystalline films, when observed, is less effective. Upon embedding, resultant mobility within the ice and the strength of intermolecular interactions can yield segregation of these gases into clusters, as seen in the case of CO_2. Tracing the kinetics of these embedding events under different energetic conditions allows for elucidation of the underlying dynamics, and we draw comparison between all studied gases to promote generalized conclusions in regards to empirical prediction of embedding probability. Through application of a classical model of the entrance barrier for atoms and molecules colliding with amorphous ice, we provide direct evidence for a unified connection between embedding probability and momentum of the incoming atoms and molecules; an account of all embedding data measured by our group traces a singular barrier. This work highlights the interplay between translational energy and momentum

accommodation during collisions with ice; atoms and molecules can become trapped in an icy surface despite an inability to simply stick to the interface. These results are of considerable importance to studies of both the astrochemistry and evolution of interstellar bodies and dust, and detailing the capture and release of gases by permafrost relating to global climate forcing.

Introduction

The interaction of gases with ice is fundamental to numerous scientific disciplines. In astrophysics, delivery of volatile species from comets theories of atmospheric formation on planets and moons focus primarily on delivery of volatile species from comets.[61–64] Simple gaseous species accumulate and concentrate within the ices of comets and pre-cometary matter,[65,66] potentially subject to bombardment by high-energy electromagnetic radiation and interstellar matter to form complicated molecules.[67] Simulation of these processes in many laboratories using pre-mixed cometary ice analogs has produced organic residues containing molecules potentially important in understanding possible sources of prebiotic chemistry on Earth.[68–74] Additionally, answers to important questions related to geophysics and global energy issues are built upon the foundation of a thorough understanding of gas-ice interactions, with intense focus on clathrate hydrates,[75,76] whose contemporary applications include endeavors into hydrogen storage[77,78] and capture of anthropogenic greenhouse gases.[79,80]

CO_2—along with its interaction with ice—represents a major constituent of interstellar matter,[81,82] and is hypothesized to be a major component of global climate forcing. Comparison between the sequestration and release of CO_2 by glacial ice during prior geological epochs and the current global climate provides tangible links to consequences associated with Earth's currently melting permafrost.[83,84] In this work, we present the first study on the capture and concentration of neutral, hyperthermal CO_2 by amorphous solid water (ASW) under ultra-high vacuum (UHV) conditions

at a surface temperature where CO_2 adsorption is infeasible as a method of accretion. We demonstrate that the observed CO_2 uptake by ASW at 125 K is dominated by the process of energetic ballistic deposition, or "embedding." This is a phenomenon we have described at length in previous publications, whereby small atoms and molecules with high translational energies and trajectories near normal incidence directly bury underneath the vacuum-solid interface upon collision.[59,85–87]

Finally, we draw comparisons between the observed embedding efficacy of CO_2 in amorphous water ice and the other gaseous projectiles studied by our group—Xe, Kr, CF_4, SF_6—and *via* application of a classical empirical model to the activated process, firmly establish a generalized connection between projectile momentum and embedding probability.

The embedding of CO_2 and other small atoms and molecules into ASW inherently differs from percolation into the bulk following adsorption onto an icy surface, which itself is well characterized.[65,66,88–92] Namely, our results imply that ice composition can be modified by gases with high translational energies, even when ice temperature precludes adsorption.[67,68] These findings have direct implications in studies of planetesimals travelling at high speeds in protoplanetary nebulae,[93] and in studies and simulations of the hazardous icing of aircraft during flight.[94,95]

Experimental Details

The experiments referenced herein were conducted in a molecular beam scattering instrument described at length in **Chapter 2**.

Ice coverage and CO_2 uptake in all experiments were quantified by integrating RAIR spectra by fitting observed bands with Gaussian peaks atop cubic baselines. All spectra were obtained using

a Nicolet model 6700 infrared spectrometer with incident *p*-polarized IR radiation reflected from the underlying Au(111) crystal at an incident angle of 75° and directed into a liquid-nitrogen-cooled MCT/A detector. Spectra were averaged over either 200 (CF_4) or 250 (CO_2) scans taken at 4 cm^{-1} resolution with clean Au(111) as background. Ice films were grown on the Au(111) crystal housed inside the UHV chamber, with the crystal secured to a temperature-controlled sample plate on the instrument's manipulator. All embedding experiments within the RAIRS instrument, unless elsewhere noted, were performed with the crystal held at 125 K as measured by a Type-K thermocouple secured to the OFHC sample plate directly beside the crystal. The sample temperature was controlled with a combination of liquid-nitrogen-cooling and resistive heating of a filament located directly behind the sample plate. Use of sixty- to seventy-five-layer thick films (one layer = 1.07 x 10^{15} H_2O molecules[96,97]) of low density amorphous ice promoted both substrate independence and homogeneity, *i.e.* self-similar structural presentation at the vacuum-solid interface.[97,98] Under these conditions, the sticking coefficient of H_2O and D_2O on both Au and water ice is nearly unity,[99] and desorption is negligible over a period of hours. Ice thickness was quantified by backfilling the main chamber at a known deposition rate with respect to the Au(111) surface and correlating the rate with growth of the integrated intensity of the ~3300 cm^{-1} OH or 2600 cm^{-1} OD bands.[100] This quantitation is valid with ice film thicknesses up to 200 layers using our setup, after which optical field penetration changes the band shape.

In order to produce the highest possible translational energies in our beam, we expand ~1% CF_4 or CO_2 diluted in H_2 at 400-600 psi through a 15μm platinum (CF_4) or molybdenum (CO_2) pinhole, with all exposure to ice done at normal incidence. CF_4 translational kinetic energies ranging from 2.3 eV to 5.4 eV with an average width (ΔE/E) of 16%, and CO_2 translational kinetic energies ranging from 0.9 eV to 4.1 eV with widths ranging from 18-46%, are all obtainable by resistively

heating the beam nozzle up to, at most, 1200 K, as characterized using time-of-flight techniques. We note that, in the case of CO_2, this method of producing high translational energies causes CO_2 and H_2 to readily react under some of the chosen conditions—to near completion as the nozzle temperature approaches 1200 K at all stagnation pressures used—producing CO and H_2O through the reverse water-gas shift reaction[101] either homogeneously or catalyzed by the exposed metal surfaces. Similar beam reactivity phenomena were reported by Herschbach *et al.* in the case of small hydrocarbons forming larger hydrocarbons within the nozzle of a molecular beam under analogous conditions.[102] While no evidence of CO accumulation is observed on or within the ice surfaces discussed in this paper, H_2O is deposited throughout our experiments with a rate typically at or below ~10^{-2} layers per second as a product of the reverse water-gas shift reaction taking place.

Total CO_2 flux from the seeded molecular beams is determined by first calibrating the pressure rise in the sample chamber with a nude Bayard-Alpert ion gauge while open to neat CO_2 beams.[59] With knowledge of the chamber pumping speed, the relative sensitivity of the gauge to CO_2,[103,104] and the beam's spot size on the Au(111) crystal, the molecular flux of the neat beam is determinable. For neat beams at different stagnation pressures, the calculated fluxes were each correlated with an observed rise in signal at m/z = 44 when open to the chamber as measured by a residual gas analyzer (RGA) located outside of the beam's line of sight. Linear regression yields direct conversion between RGA signal rise and total CO_2 flux, and in this way, CO_2 flux in seeded beams could be determined purely from the RGA readings for all experiments.

Results and Discussion

Embedding: Ice Structure and Composition

CF_4 uptake by ASW D_2O ice was confirmed with the reproducible appearance of peaks at 1276 and 1257 cm^{-1} upon exposure of the ice to the CF_4 beam at a variety of incident translational energies. An example of embedding with an incident CF_4 translational energy of 5.3 eV is detailed in **Figure 4-1**. Observed peak locations correspond to the Fermi resonance of the ν_3 asymmetric stretch and the first overtone of the ν_4 deformation, respectively. The peaks are red-shifted from the gas phase values (1283 and 1261 cm^{-1}, respectively[105,106])—a phenomenon often observed for species physically adsorbed to or bound within an inert matrix.[107] These values are not red-shifted towards values observed for condensed phases with significant CF_4-CF_4 intermolecular interaction,[107,108] and thus we infer from the IR data that the CF_4 molecules are sparsely dispersed amongst the D_2O molecules in the ice film.

Given that sticking is observed to be negligible at this temperature, we infer that the mechanism behind CF_4 uptake is that of energetic ballistic deposition, akin to what has been previously observed for Kr and Xe in H_2O and D_2O ices.[85] The initial rate of CF_4 embedding is observed to be linear in all cases, with observable embedding occurring above a critical translational energy near ~3.0 eV, as determined by RAIRS. From **Figure 4-2**, the CF_4 embedding was not observed to saturate after more than ten thousand layers of CF_4 were dosed. This distinctly contrasts the case of rare-gas-embedding, where saturation occurred after dosing only four thousand layers of either Kr or Xe embedding into ASW and CI crystalline ices.[85] In the same study, it was observed that ~3 eV Kr and Xe deposition saturated near a total uptake of ~0.5 layers. For purposes of comparison to the Xe data, we have related the total CF_4 flux to a measure of "layers of CF_4" by approximating the packing density of a CF_4 monolayer as being comparable to that of Xe given its similar size. Given the comparable size of CF_4 to Kr and Xe, as well as the similar energy used in the saturation experiment detailed in **Figure 4-2**, we make the assumption that CF_4 saturates at

Figure 4-1

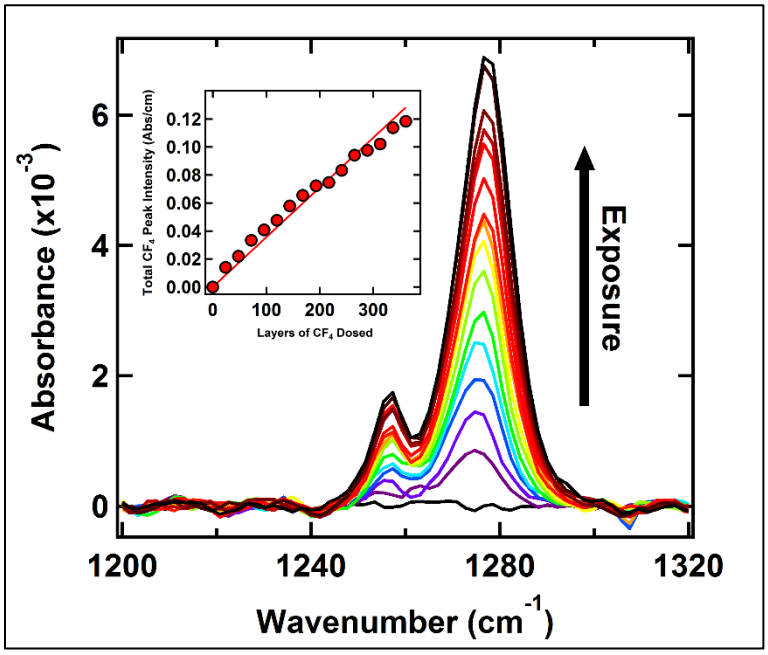

Uptake of hyperthermal CF_4 by ASW D_2O ice as measured by RAIRS. *Energetic ballistic deposition of 5.3 eV CF_4 into ASW ice is characterized by the appearance of RAIRS peaks at 1276 and 1257 cm^{-1}, the intensity of which increases linearly with respect to the total amount of CF_4 dosed onto the surface at normal incidence. Inset graph details the linear dependence, the slope of which is taken as the initial rate of embedding into 60 layers of ice. Each data point is the integrated intensity of the two peaks in each of the displayed spectra. Copyright 2014 American Institute of Physics.*[59]

Figure 4-2

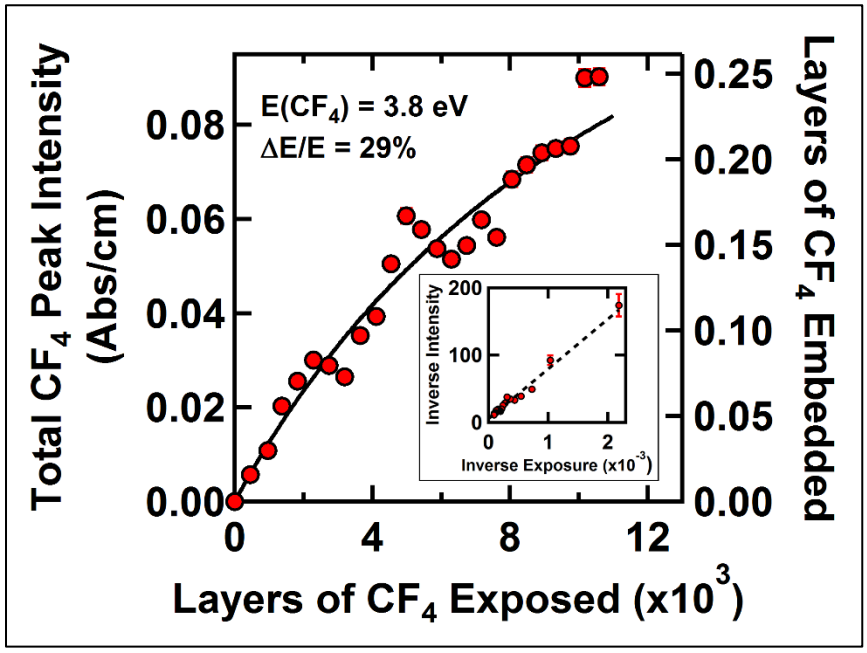

CF_4 absorptivity quantification via measurement of saturation in ice. *Total CF_4 in the ice is not observed to saturate after exposure to more than ten thousand layers of CF_4 as measured by RAIRS, in contrast to the trend observed with rare-gas-embedding which saturates by four thousand layers of exposure in both ASW and CI ice films. The curved solid line is the Langmuir isotherm fit to the data as determined by a linear least-squares fit shown in the figure's inset. The saturation experiments were performed with a 30 μm nozzle at 120 psi in order to maximize CF_4 flux, which in turn yielded a larger incident CF_4 energy distribution of 29%. Error bars (where visible) indicate one standard deviation with respect to the integration of peaks fit to the IR data. Copyright 2014 American Institute of Physics.*[59]

this same level; the CF_4 molecules' access below the second ice layer is not probable. Applying a simple Langmuir adsorption treatment to the data (see inset of **Figure 4-2**), the IR intensity can be expected to saturate at 0.18 ± 0.01 for 3.8 eV CF_4, and we take this intensity to be that of a half-monolayer, yielding a conversion factor for the IR data of 2.8 ± 0.2 layers per integrated absorbance unit.

Upon exposure of ASW to high-translational-energy CO_2, a rich profile of local environments is observed between 2320 and 2380 cm^{-1}. **Figure 4-3** depicts example chronological spectra obtained by continuously exposing an ASW film to CO_2 with average translational energy of 4.1 eV. While our analysis focuses primarily on monitoring the intensity of the most prominent mode at 2341 cm^{-1} as a function of exposure and CO_2 translational kinetic energy, the overall IR response of the film encompasses detailed information about the structure of the ice film after embedding and is worth highlighting. The sharp (FWHM < 5 cm^{-1}) signal at 2341 cm^{-1} exhibits a 4 cm^{-1} redshift compared to signals observed in pure CO_2 ices, both thick and thin.[92,109,110] This observation aligns with those made in several studies; CO_2 weakly interacting with surrounding water decreases the ν_3 mode's effective force constant, making distinction between *surface adsorbed* and *bulk absorbed* CO_2 trivial.[110,111] Given that stable CO_2 deposition occurs below 90 K[91]—much lower than our experimental conditions—and that another signal does not appear near 2345 cm^{-1}, we infer that all CO_2 accumulated on the surface must be buried beneath the vacuum-solid interface, despite the fact that the ASW film is nonporous as prepared.[112] It is also important to note that we do not observe uptake when the ice film is crystalline. This observation is consistent with our prior reports of embedding and persistance occurring more readily within amorphous films, compared to crystalline films; molecular dynamics simulations of hyperthermal Xe collisions with crystalline

Figure 4-3

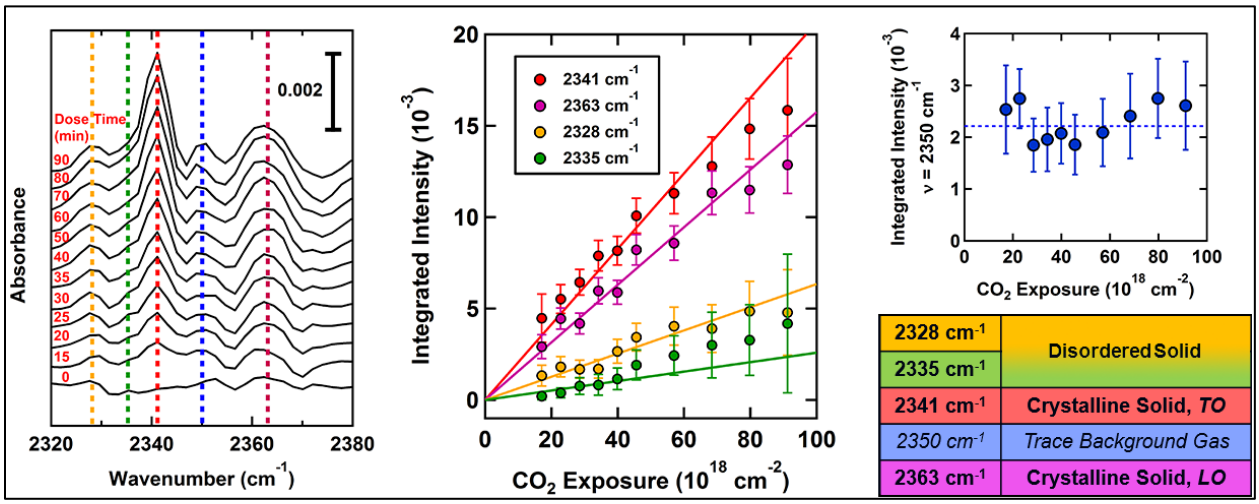

Uptake of hyperthermal CO_2 by ASW H_2O ice and spectral identification. *Representative RAIR spectra obtained during exposure of 4.1 eV CO_2 to sixty-layer-thick amorphous H_2O ice film. Boldface signals in table (2328, 2335, 2341, 2363 cm^{-1}) are associated with solid CO_2 uptake, whose integrated peaks grow linearly as a function of total exposed CO_2. The signal at 2350 cm^{-1} is associated with trace background CO_2 in the IR beam path within the sample chamber and remains essentially constant throughout the experiment as shown in the top-right plot. Copyright 2015 American Chemical Society.*[60]

ice produce trajectories whereby a Xe atom is ejected from within the selvedge on the order of picoseconds.[59,85–87]

Concurrent with growth of the 2341 cm^{-1} peak is growth of a peak at 2363 cm^{-1}, suggesting that accumulated CO_2 molecules are not homogeneously, "infinitely" diluted within the ice but concentrated into small aggregates. This is in agreement with one study concluding that CO_2 is mobile within ice above 60 K and exhibits a high degree of segregation when deposited above this temperature; CO_2 exists within ices of this nature mostly as pure crystallites.[113] This peak assignment further aligns with numerous studies of CO_2 clusters in both pure gaseous and solid phases.[114–118] The two aforementioned peaks correspond, respectively, to the transverse optical (TO) and longitudinal optical (LO) modes of the crystallites, and the peak position of the LO mode in particular (2363 cm^{-1}) suggests that CO_2 aggregates within the ice resemble rods, as opposed to large slabs (2381 cm^{-1}) or spheres (2356 cm^{-1}).[119–121] Offering insightful contrast, CF_4 showed no signs of clustering after embedding into ASW grown under identical conditions.[59] Aggregation dynamics within the ice film are expected to depend on both the mobility of the absorbed species and the relative energetic interactions between guest and host molecules. CF_4 molecules are quite similar to noble gases in terms of their intermolecular interactions; high symmetry and small size leads to CF_4's weak electrostatic interactions with itself and other molecules.[122] Interaction energies of CF_4 with itself and water are each on the order of only a few kJ mol^{-1},[123–125] while CO_2 dimer interaction energy is roughly equal to, if not greater than, that of CO_2-H_2O, and closer in magnitude (~20-25 kJ mol^{-1}) to the H_2O dimer interaction energy (~40 kJ mol^{-1}).[91,126]

Aside from an unchanging weak absorption at 2050 cm^{-1} from trace gaseous CO_2 in the IR beam path, **Figure 4-3** also tracks two weak features at 2328 cm^{-1} and 2335 cm^{-1}. The former has previously been identified in literature as belonging to amorphous or disordered CO_2,[127] although

our surface is well above the temperature at which amorphous CO_2 is stable. Indeed, extremely red-shifted spectral features have been reported in CO_2/H_2O mixtures,[128] but again, studies such as these were conducted at temperatures well below 125 K, complicating direct comparison. Literature studies suggest that, for instance, the surface and subsurface layers of water ice nanocrystals can have differing degrees of disorder compared to their cores,[129,130] and absent any confirmation by high-level theoretical simulations of this system, it remains plausible that CO_2 aggregates formed after embedding exhibit analogous behavior.

Kinetics and Dynamics of CO_2 Embedding in Ice

As noted in the experimental section, H_2O can also be generated in the seeded supersonic molecular beam at the nozzle temperatures required to obtain CO_2 with the highest translational energies studied. Consequently, H_2O is also deposited onto the ice film throughout CO_2 exposure, typically at or below a rate of $\sim 10^{-2}$ layers per second. To deconvolute our observations from this co-deposition, and to confirm no modification of our embedding results due to the presence of low water flux, a series of control experiments were executed, with results detailed in **Figure 4-4**. Ice films were exposed to either CO_2/H_2O mixtures—produced by bubbling CO_2 through an H_2O filled reservoir—or exposed to a lower energy (~1 eV) CO_2 beam during simultaneous backfilling of the sample chamber with pure water vapor. **Figure 4-4(*a*)** compares RAIR spectra from both high- and low-energy trials with equal total CO_2 exposures. In all cases, only trace gaseous background CO_2 (2050 cm^{-1}) was observed when low-energy CO_2 was used, irrespective of the total H_2O co-deposition rate and the manner in which H_2O was deposited. **Figure 4-4(*b*)** shows an embedding experiment where, beginning at the 120-minute mark, the total deposition rate of H_2O was deliberately increased by one order of magnitude *via* simultaneous backfilling of the chamber with H_2O. As evidenced by the plot, the CO_2 uptake rate remains constant despite the large differences

Figure 4-4

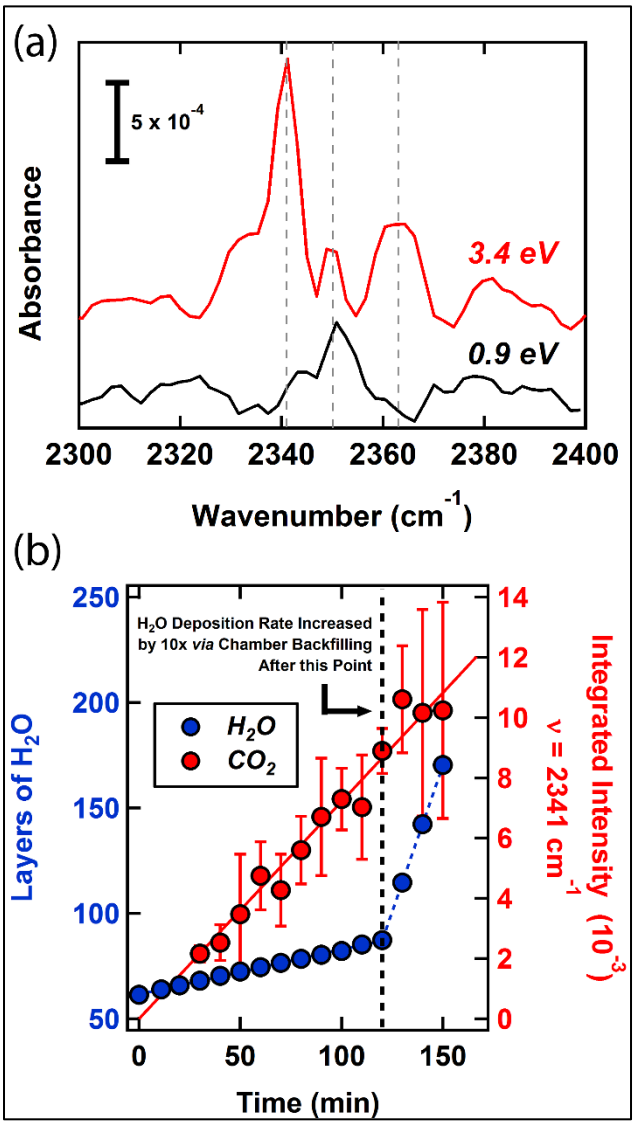

Data from control experiments confirming CO_2 embedding. ***(a)*** *CO_2 RAIRS signals obtained during exposure to a high-translational-energy seeded CO_2 beam (red) and during low-translational-energy beam co-deposition of CO_2/H_2O (black). High CO_2 translational energies are required for resolution of solid CO_2 spectroscopic signals.* ***(b)*** *Embedding experiment with two different total H_2O deposition rates over the course of exposure, showing no change in the rate of CO_2 uptake as measured by RAIRS and demonstrating the observed accumulation's independence from background water deposition. Copyright 2015 American Chemical Society.*[60]

in H_2O deposition rate. Thus, these results confirm the embedding rate's independence from the low water flux; burying does not occur. These findings are, again, further backed by temperature-programmed desorption (TPD) experiments in the literature performed on both Au(111) and H_2O ice that place stable deposition of CO_2 at surface temperatures well below 125 K.[91]

The initial CO_2 uptake rate is observed to be linear with respect to amount dosed in all measurements made with exposure to CO_2 with translational energy 3.0 eV or greater. **Figure 4-5** shows uptake rates of CO_2 by amorphous ice at three different average translational energies with the abscissae of each data set normalized to each other *via* multiplication of the total exposure time to the beam at each time point by the experiment's respective CO_2 flux. In order to approximate the total amount of CO_2 molecules embedded at any given time, the integrated intensity of the 2341 cm^{-1} peak is divided by the absorptivity of this mode for CO_2 diluted in ice (1:10), as measured *via* transmission IR by Sandford and Allamandola at 10 K.[126] The absorptivity is linearly corrected to one at 125 K, as discussed in their paper. Given this transformation, the slopes of the linear uptake curves represent initial embedding probabilities for CO_2 at the respective energetic conditions. As seen in **Figure 4-5**, the initial uptake rate is clearly highest for the most energetic CO_2 molecules.

The molecules in the beam populate a translational energy distribution with a finite width, and therefore each embedding probability measured represents a convolution of the energy distribution with a small range of probabilities. To deconvolute the data and extract the true energy dependence outlining the dynamics of the embedding process, a polynomial nonlinear least-squares fit to the data, $f(E)$, was employed as an ansatz for the actual rate dependence and deconvoluted from the incident energy distribution, $P(E)$, to give the measured dependence, $F(E)$, as plotted in **Figure 4-6** for CF_4 and **Figure 4-7(*a*)** for CO_2:

Figure 4-5

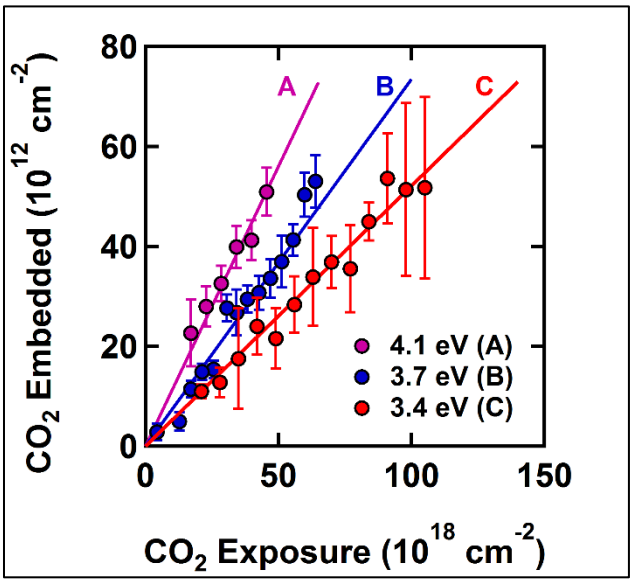

Initial CO_2 embedding probabilities for three different kinetic energies. *See text for details regarding conversion of ordinate axes from integrated peak intensity to number embedded. Over the energy range studied, as the average kinetic energy of the incident CO_2 increases, the initial embedding probability also increases. Copyright 2015 American Chemical Society.*[60]

Figure 4-6

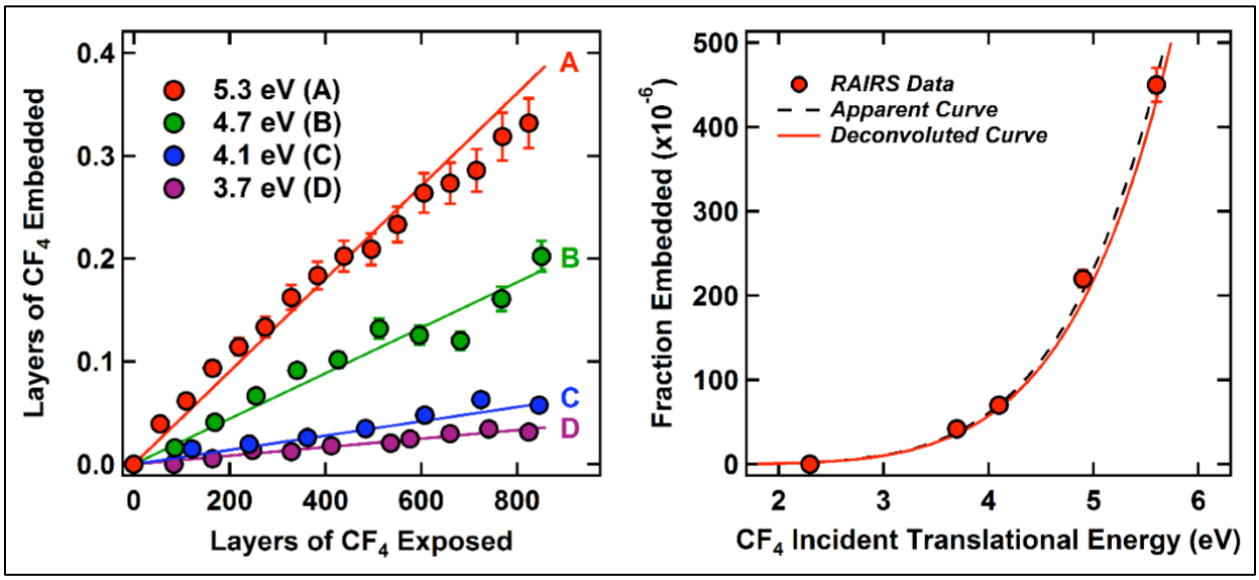

Initial CF_4 embedding probabilities and its dependence on kinetic energy. (Left) *Representative initial embedding fractions of CF_4 into 60 layers of ASW D_2O ice as measured by RAIRS. In all cases, uptake was observed to be linear, with higher rates observed for higher-energy CF_4. Error bars (where visible) take into account both the error in the conversion factor and one standard deviation with respect to the integration of peaks fit to the IR data.* ***(Right)*** *Energy dependence of embedding rate: dashed line indicates the sigmoid function fit to the apparent dependence derived from experimental data (solid circles), solid line indicates energy dependence de-convoluted from incident CF_4 energy distribution. Embedding of CF_4 is only observed to occur above a threshold near 3.0 eV. Error bars (where visible) represent 95% confidence intervals for the linear fits. Copyright 2014 American Institute of Physics.*[59]

Figure 4-7

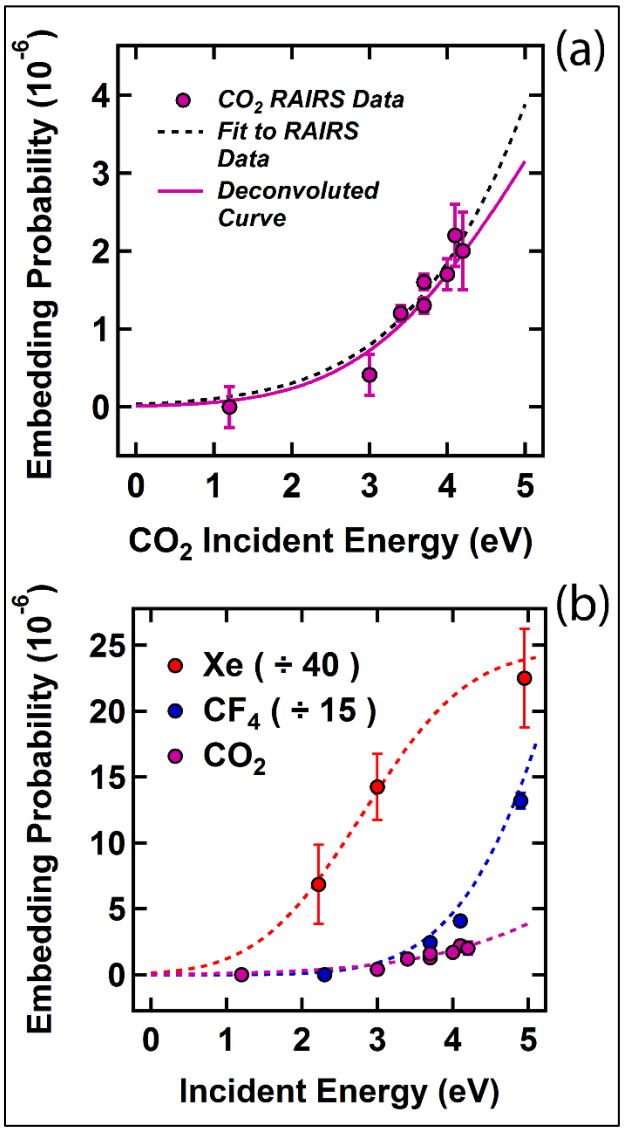

CO_2 embedding's energy dependence and comparison to Xe and CF_4. ***(a)*** *Initial CO_2 embedding probability increases as a function of incident kinetic energy. Measured data are deconvoluted from the CO_2 energy distributions using a polynomial ansatz, yielding the solid purple curve (see text for details).* ***(b)*** *Application of constrained, parameterized S-curves to the data allow for comparison of CO_2 embedding probabilities to those previously measured for CF_4 (using RAIRS) and Xe (using a different method [59]). Over a similar energy range, the embedding probability for CO_2 is measured to be smaller by roughly one and three orders of magnitude as compared to CF_4 and Xe, respectively. Copyright 2015 American Chemical Society.*[60]

$$F(E) = \int f(E')P(E')dE' \quad \textbf{(4-1)}$$

The results are consistent with conclusions made previously, namely that: (*a*) there is a rapid increase in embedding probability above some energetic threshold, and (*b*) given that the projectile is below a critical size, the mass of the projectile is important in predicting embedding efficacy.[59] **Figure 4-7(*b*)** clarifies this point, revealing the embedding probability of ~4 eV CO_2 to be roughly one and three orders of magnitude lower than that of homoenergetic CF_4 and Xe, respectively, despite similar size (radii as estimated from gas-phase van der Waals *b* parameters:[131] CO_2, 2.1 Å; CF_4, 2.9 Å; Xe, 2.7 Å).

Embedding as an Activated Process

In order for a projectile to embed, it clearly must first overcome an energetic barrier associated with travelling beyond the immediate vacuum-solid interface in order to become buried within or underneath the selvedge, and therefore embedding can be considered an activated process. As originally established by Lennard-Jones, the paradigmatic notion of a barrier formed from the crossing of repulsive and attractive states between a gaseous projectile and a metal surface sought to describe the dynamics of dissociative adsorption.[132] The underlying dynamics behind projectiles embedding into ASW draw close comparison with these processes upon inspection (e.g. rapid increase above a threshold, saturation at high energy), and application of an empirical classical barrier to this entrance channel offers an opportunity to draw useful conclusions by comparing the dynamics of all projectiles we have studied, including CO_2. To this end, we adopt an *S*-shaped, parameterized form for the embedding probability used to evaluate the dissociative adsorption dynamics of molecular hydrogen on single-crystal copper surfaces[133] and described by Harris:[134]

$$\sigma(E) = \frac{A}{2}\left(1 + \tanh\frac{E-E_0}{W}\right) \quad \textbf{(3-2)}$$

In the above equation, E_0 represents the energetic barrier, W represents the range of energies over which the curve rises—related to a distribution of barrier heights dependent upon position of impact, and A represents the saturation value for the probability.

The application of this empirical model to our data is presented in **Figure 4-7(*b*)**. We expect that ice morphology critically influences the embedding process—projectiles are more deeply embedded in amorphous ice[59,85–87]—and while ASW morphology heavily depends upon both surface temperature and deposition angle, ASW films grown at 125 K are expected to be insensitive to deposition method,[112] and thus all ice films studied here are consistent. Consequently, A and W are held constant in these fits to compare the projectiles within this framework, given their size does not prevent their embedding; they are all smaller than SF_6, the largest projectile we have investigated which did not embed at any energy examined.[59] The fits were performed with A held constant at 0.001 and W constrained between 1 and 2 eV for the case of CO_2 due to our data sampling only the low-energy region of the curve. The curves in **Figure 4-7(*b*)** clearly show that, over the examined energy range, the embedding probability of CO_2—the projectile with the lowest mass—is significantly lower than that of the heavy CF_4 and Xe projectiles. Importantly, under this treatment, the *energetic* barrier values (E_0) for the Xe, CF_4, and CO_2 projectiles all yield nearly identical values for the barrier in terms of the *momentum*. Illustrated in **Figure 4-8**, the embedding probability is plotted against the incident translational momentum for all data collected by our group, and the complete momentum space sampled appears to trace a single curve. This is the first compelling empirical evidence in support of our prior conclusion that embedding efficacy is shaped by the incident translational momentum of a projectile upon collision with ice.[59]

Figure 4-8

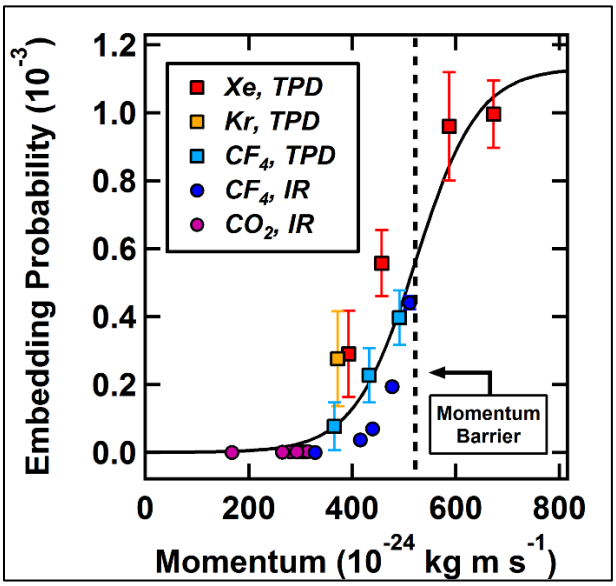

Unified classical momentum barrier model for embedding. *Accounting for the mass of each projectile yields a singular value for the barrier in terms of momentum; a plot of all amassed embedding data traces a unified barrier model across the sampled momentum space. Datasets marked TPD were taken using a different experimental method.*[59] *IR dataset error bars are smaller than the data points within the figure. Copyright 2015 American Chemical Society.*[60]

Open questions remain regarding the inherent differences in embedding efficacy involving ASW versus CI films. Ice films possess remarkable resilience to bombardment by high-energy projectiles *via* rapid energy dissipation,[100] and facile momentum transfer between projectiles and the recoiling ice matrix clearly leads to observable trapping at elevated temperatures relative to the desorption temperature of the projectiles, but perhaps *only* if the projectile drives deep enough into the ice film upon impact. Although possible that the local geometry encountered by a projectile is different between the two structures, factors affecting a projectile's persistence (i.e. extent of momentum transfer, mobility within the ice, cohesion of the surrounding ice lattice) after penetration are likely important—perhaps the most important—considerations; a higher embedding probability in ASW could possibly be linked to its structural similarities with liquid water.[135–137] While future theoretical work on this system is planned, support for this hypothesis comes in the form of prior molecular dynamics simulations of hyperthermal Xe collisions with hexagonal ice, where Xe atoms with high incident translational energy and trajectories primarily closer to normal incidence relative to the surface penetrated the vacuum-solid interface to greater depths, residing within the first one to four layers at the vacuum-solid interface and exhibiting low desorption probability at long ice residence time.[85,87]

Conclusion

Utilizing time-resolved *in situ* RAIRS we have conducted the first study of hyperthermal CO_2 capture by ASW under UHV conditions. Informed by results obtained for CF_4, these measurements were done at a temperature below but approaching its crystallization point. CO_2 is observed to directly embed underneath the vacuum-film interface and become trapped in the ice matrix at a much higher temperature than that allowed by thermal accretion, rapidly diffusing to form aggregates with primarily rod-like geometries, as suggested by the distinct spectroscopic signature

observed. Application of a classical model treating the entrance of CO_2 and other gaseous projectiles into the ice as an activated process provides empirical evidence that projectile momentum is a general defining factor for embedding probability, provided that the projectile is not too large. Molecular dynamics simulations of the CO_2/H_2O interaction presented here would be a fruitful future endeavor and could provide further insight into the embedding of gaseous molecules with strong electrostatic interactions. Additionally, examination of embedding efficacies over a wider range of surface temperatures may better define the relationship between embedding probability and an embedded projectile's persistence in terms of its mobility within an amorphous ice film; we plan to pursue this route with the future construction of instrumentation capable of achieving significantly lower ice temperatures.

The results produced herein host significance in applications pertaining to the measurement and accurate modelling of gaseous accretion by ices, both terrestrial and extraterrestrial; relevant areas of interest include comet and planetesimal formation in the interstellar medium, gas capture related to global energy and climate issues, and the icing of aircraft in high velocity gas flows. A complete account of ice modification by gases is bolstered by recognition of embedding as a pathway for the uptake of gases by water ice at temperatures which would otherwise thermodynamically prohibit surface adsorption.

Chapter 5

Oxidation, Destruction, and Persistence of Multilayer Dimethyl Methylphosphonate Films during Exposure to $O(^3P)$ Atomic Oxygen

This chapter contains an article that was reproduced in part with permission from The Journal of Physical Chemistry C, accepted for publication. Copyright 2016 American Chemical Society.[138]

We present work detailing the oxidative reactivity of the nerve agent simulant dimethyl methylphosphonate (DMMP) by atomic oxygen using time-resolved *in situ* reflection-absorption infrared spectroscopy (RAIRS) and X-ray photoelectron spectroscopy (XPS). When exposed to a supersonic beam containing $O(^3P)$ with average translational energy of 0.12 eV, thermally-annealed DMMP films (less than fifty layers) on single-crystal Au(111) are observed to react *via* hydrogen abstraction, followed by various secondary reactions with resultant hydroxyl and DMMP-derived radicals. This reaction is accompanied by the appearance of hydrogen bonding interactions with the DMMP phosphoryl (P=O) groups on the film surface, and it is also observed to result in both a loss of carbon and an uptake of oxygen by the film. These trends, when considered with the additional thermal stability of reaction products left on the surface, suggest that the mechanism entails reaction with DMMP methyl groups and the formation of various polymeric species; the presence of these polymers hinders continuous, effective destruction for films thicker than roughly ten layers. This work has specific implications for the implementation of plasma-based and oxidative decontamination methods based upon an improved fundamental understanding of the chemistry of the important class of phosphoryl containing molecules.

Introduction

The 1993 Chemical Weapons Convention prohibits the creation and stockpiling of chemical weapons, yet these dangerous compounds remain a critical social and environmental threat.[139] Whether decontaminating attack sites or destroying unused chemical weapon stores, there is a great risk to both civilians and military personnel if these agents' surface interactions are not properly understood; any new destruction strategy must, in addition to removing the toxic agent, account for volatile byproducts, secondary contamination, and waste disposal.[140] As such, it is critical to have a comprehensive grasp of the agents' destruction pathways and mechanisms, persistence, and potential re-dispersal on a myriad of representative environmental and industrial materials.

The surface interactions of nerve agents and their simulants have been investigated thoroughly on a number of surfaces to date, including metals,[141–145] metal oxides,[142,146–157] nanoparticle assemblies,[158–160] and other thin films[161–164]; complementary theoretical analyses have also been published for many of these systems.[165–172] Notably, many of these materials (particularly metal oxides) have demonstrated significant catalytic activity in the decomposition of surface adsorbed dimethyl methylphosphonate (DMMP), a common nerve agent simulant. While effective, active site poisoning often limits the practicality of these methods on a large scale. Furthermore, these oxide materials are often difficult to reactivate once poisoned.[150,152] To overcome these limitations and establish continuous decomposition activity, Mitchell *et al.* explored the reaction of DMMP and ozone on alumina-supported iron oxide and manganese oxide. Measurements of the resultant CO and CO_2 production revealed higher catalytic activity in the presence of ozone, due to the formation of reactive atomic oxygen species resulting from ozone's decomposition on the oxide surface.[173,174]

Additional nerve agent decontamination strategies involve exposure to atmospheric pressure plasma sources.[175–179] While many current decontamination methods rely on complete incineration at high temperatures[180–182] or corrosive wet chemicals (*i.e.* bleach), use of these plasmas provides a non-destructive, environmentally safe alternative that precludes mass storage and long exposure times.[140,179] Like the aforementioned continuous decomposition studies, the effectiveness of this method is also linked to the presence of both ozone and atomic oxygen in the plasmas.[177] In addition to clarifying the basic mechanisms underlying some of these destruction techniques, the results of this study may also shed light on the known flame-retarding properties of organophosphate compounds.[183,184]

Informed by recent theoretical work on gas-phase reactivity between DMMP and $O(^3P)$,[185,186] we present a detailed picture of the oxidative destruction of solid multilayer DMMP films and elucidate the mechanistic role of atomic oxygen in its destruction. Reflection-absorption infrared spectroscopy (RAIRS) and X-ray photoelectron spectroscopy (XPS) were used to demonstrate that DMMP reacts upon exposure to $O(^3P)$ under ultrahigh vacuum (UHV) conditions, and that the reaction likely generates additional reactive species on the surface. Furthermore, we present clear evidence that overall reactivity decays upon continued exposure, and results in formation of additional byproducts possessing greater thermal stability on the surface than the original DMMP. Reactive oxygen species have been shown to be important in the destruction of nerve agents and their simulants in applications ranging from preventative surface treatments to post-contamination remediation. The findings contained herein have direct implications for understanding the fate of dispersed agents subject to naturally occurring oxygen species and better inform development of safe and effective decontamination techniques.[187,188]

Experimental Details

All experiments were conducted in a molecular beam scattering instrument previously described in detail in **Chapter 2**.

DMMP was deposited on single-crystal Au(111) in the chamber *via* a directed doser located approximately two inches from the crystal front. RAIR spectra, fit to Gaussian peaks on cubic baselines, were used to characterize the surface and extent of reactivity. Spectra were obtained with a Nicolet 6700 infrared spectrometer; *p*-polarized IR radiation is reflected from the Au(111) substrate at a 75° incident angle and collected in a liquid-nitrogen-cooled MCT/A detector. Spectra were averaged over 300 scans at 4 cm^{-1} resolution, using sputtered/annealed Au(111) as the background reference signal. A representative spectrum of a DMMP film is shown in **Figure 5-1**. The intense P-O-C and P=O modes, highlighted in the inset of **Figure 5-1**, are most frequently referenced herein, with observed peak positions and assignments informed by and consistent with the literature.[144,148,149,154,164] For all experiments involving reaction of DMMP with $O(^3P)$, the surface temperature was held at 155 K during dosing, where DMMP desorption is observed to be negligible. After dosing, the films were annealed at 175 K until desired thicknesses were reached.

A series of isothermal desorption experiments allowed for initial DMMP film thickness quantification *via* RAIRS (**Figure 5-2**). DMMP films were subjected to desorption at surface temperatures ranging from 163-165 K, and the integrated areas of the P-O-C stretching modes were tracked as a function of time. Total integrated peak intensity is observed to decay linearly at two different rates, corresponding to a difference in multilayer and monolayer desorption rates, respectively.[189] As displayed in each panel of **Figure 5-2**, the spectroscopic signature of the monolayer is determined from the point at which the rate abruptly changes. Using our experimental

Figure 5-1

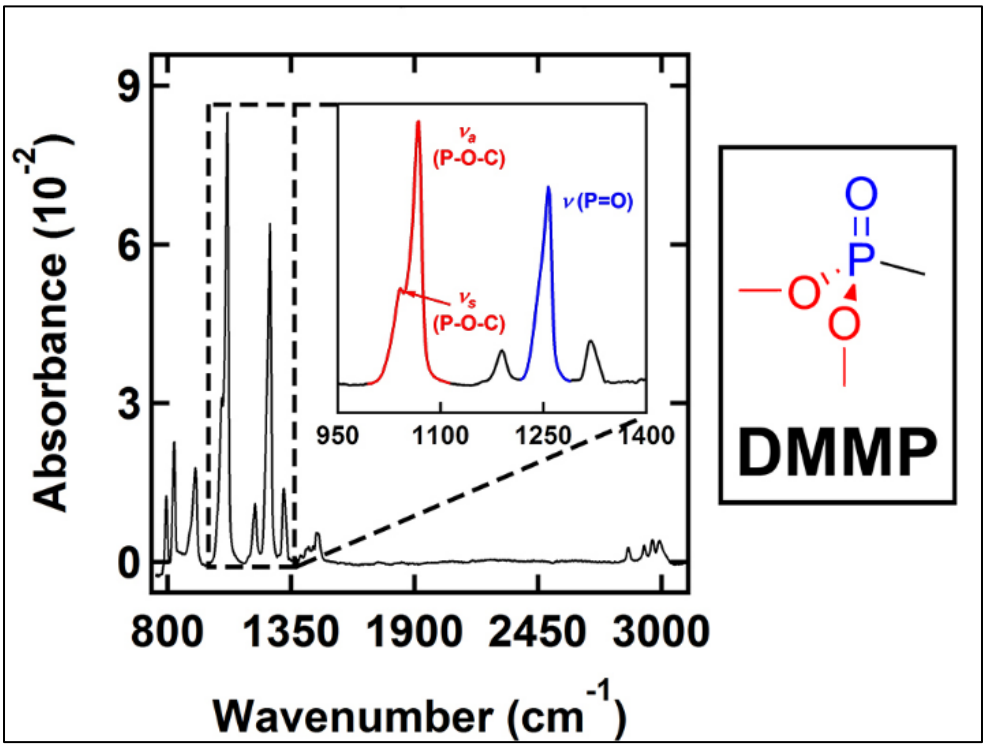

Representative RAIR spectrum of DMMP film. *RAIR spectrum of forty-layer thick DMMP film on single-crystal Au(111). Notable signals discussed throughout text include the P-O-C (red, 1041 and 1066 cm^{-1}) and P=O (blue, ~1240-1260 cm^{-1}) stretching modes; these are highlighted in the DMMP molecule and spectrum inset.*

Figure 5-2

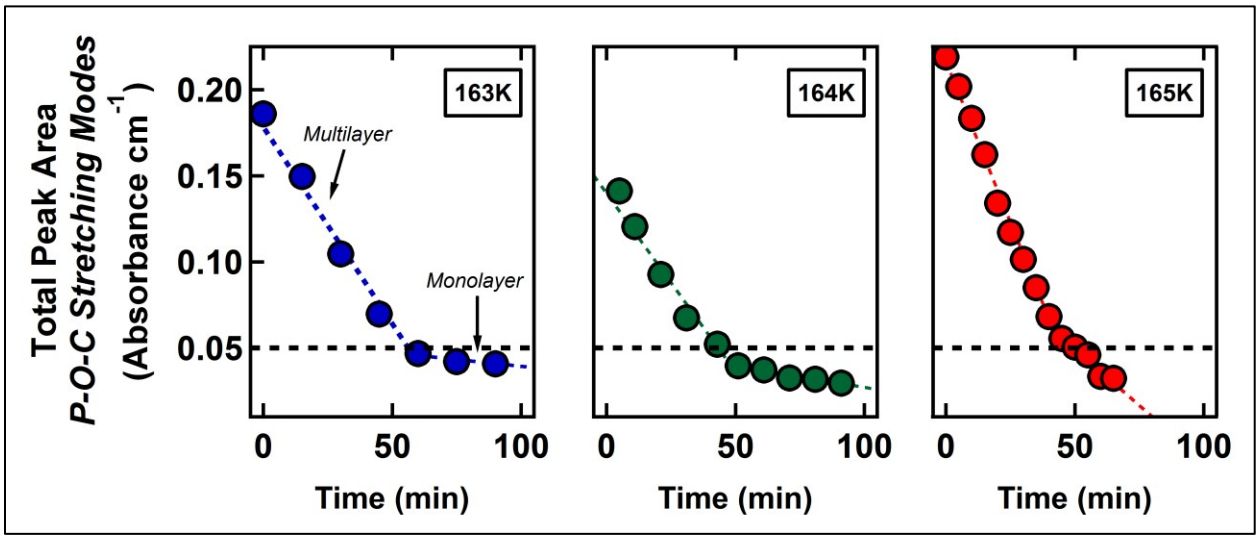

DMMP absorptivity quantification via isothermal desorption. *Isothermal desorption of DMMP films allows for quantification of initial film thicknesses via integrated P-O-C signal intensity. Transitioning from multilayer to monolayer desorption exhibits a marked decrease in desorption rate; the value where this occurs correlates with the infrared intensity of a single layer of DMMP.*

setup, one layer of DMMP corresponds to a total integrated P-O-C peak intensity of 0.05 Absorbance units cm^{-1}. Initial film thicknesses reaching upwards of fifty layers were quantified using this procedure, given that peak line shapes remained consistent with continued DMMP exposure.

The previously-described radio frequency plasma source (**Chapter 2**) generated supersonic expansions containing atomic oxygen. A gas mixture of 5% O_2 in neon flowed through a water-cooled quartz nozzle, with 35-60% of the O_2 subsequently dissociating to $O(^3P)$ in the high temperature plasma localized at the end of the nozzle. We note that under certain conditions, this type of discharge source may also produce trace concentrations of O^+ ions and $O(^1D)$, both of which exhibit different reactivity in comparison to $O(^3P)$, such as insertion as opposed to abstraction. However, the presence of a 2000 V cm^{-1} deflecting field region in our instrument for the incident beam filters out any ionic species downstream, and the RF power and gas pressure used in the current study (100 W and 75 Torr, respectively) are both significantly lower than the conditions typically used when one seeks to intentionally produce $O(^1D)$ beams for reactive studies.[6–8]

Time-of-flight experiments quantified $O(^3P)$ translational energy and flux. Total $O(^3P)$ flux was determined from the integrated peak areas of time-of-flight spectra obtained for the O_2 component of the expansion as measured by an in-line quadrupole mass spectrometer (QMS) calibrated to the flux of a neat O_2 beam.[59] The pressure rise in the chamber for the neat beam was measured with a nude Baynard-Alpert ion gauge, and the flux was calculated using this pressure rise, the chamber pumping speed, the relative sensitivity of the gauge to O_2,[104,190] and the spot size on the Au(111) crystal. The $O(^3P)$ flux is related to the O_2 flux through the O_2 dissociation percentage. Typical values for the average translational energy and flux of $O(^3P)$ from the beam impinging at normal

incidence are, respectively, 0.12 eV and 5 x 10^{16} atoms cm^{-2} s^{-1}. Beam energy widths are approximately 0.06 eV.

During XPS experiments, X-rays from an Al Kα (1486.6 eV) X-ray source operating at 10 kV and 20 mA irradiated the sample at a 45° incident angle. Spectra in the C(1s), O(1s), and Au(4f) regions were obtained using a double pass cylindrical mirror analyzer (PHI model 15-255G) with a 50 eV pass energy and 0.4 eV step size, with peaks fit in the same manner as that used in RAIRS analyses. The binding energy scale was calibrated in reference to the intense pair of Au(4f) peaks at 87.63 eV and 83.95 eV.[5]

Results and Discussion

Spectral Assignment and Film Reactivity

A number of spectral changes are clearly observed upon exposing DMMP films to O(^{3}P). **Figure 5-3** depicts, chronologically, changes in the methoxy group signals (1041 and 1066 cm^{-1}) of the film as a function of total O(^{3}P) exposure. While the peak locations, consistent with reported values for the symmetric and antisymmetric P-O-C stretches,[149,161,162] remain unchanged, both peaks are observed to decrease in intensity in **Figure 5-3(*a*)**. Given the multilayer character of the films studied, this behavior cannot be attributed to a change in average orientation of these groups, and is instead ascribed to reactive destruction. In contrast, the total integrated intensity of the P=O stretching modes of a given film P=O (~1200-1270 cm^{-1}) does not exhibit the same behavior. As seen in **Figure 5-3(*b*)**, total P=O intensity is left unchanged by extended O(^{3}P) exposure.

Spectra highlighting the individual peaks that comprise the P=O stretching region are depicted in **Figure 5-4(*a*)**. P=O peak positions are highly sensitive to coordination environment, whether *via*

Figure 5-3

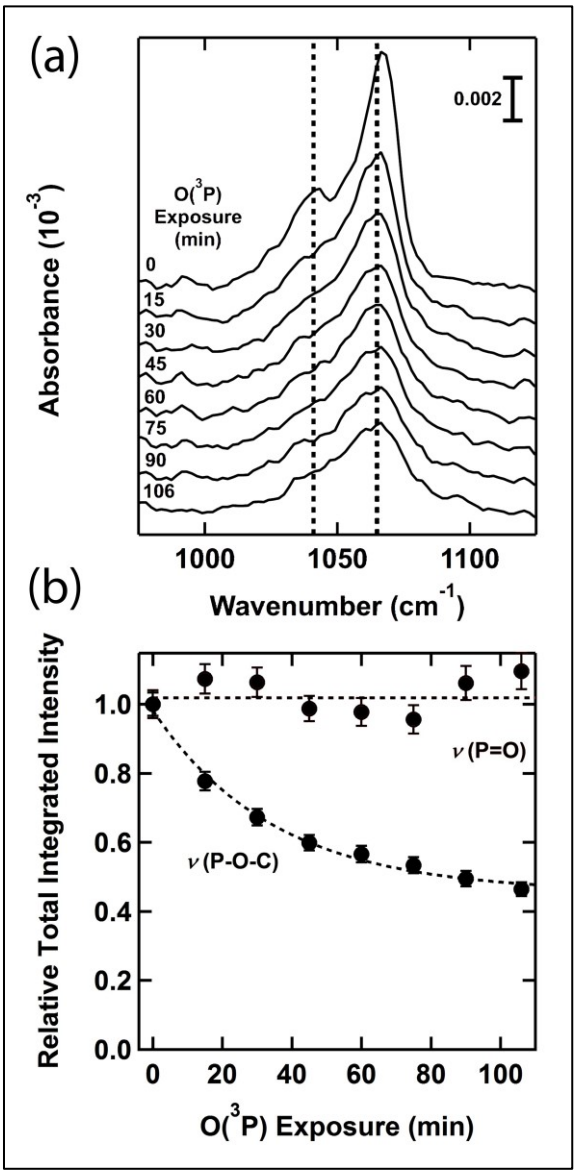

Comparison of P-O-C and P=O modes of DMMP during exposure to O(^{3}P). (a) *RAIRS signal in the P-O-C region of a six-layer thick DMMP film obtained during exposure to a molecular beam containing 0.12 eV O(^{3}P) (flux = 2.9 x 10^{16} cm^{-2} s^{-1}); total intensity is observed to decay as a function of total O(^{3}P) exposure.* ***(b)*** *Total integrated RAIR peak intensities normalized to their initial values show that, unlike the P-O-C signal intensity, the total P=O intensity is left unchanged by O(^{3}P) exposure. Dotted lines are drawn with intent to guide the eye. Error bars, where visible, indicate one standard deviation with respect to the peak fitting.*

Figure 5-4

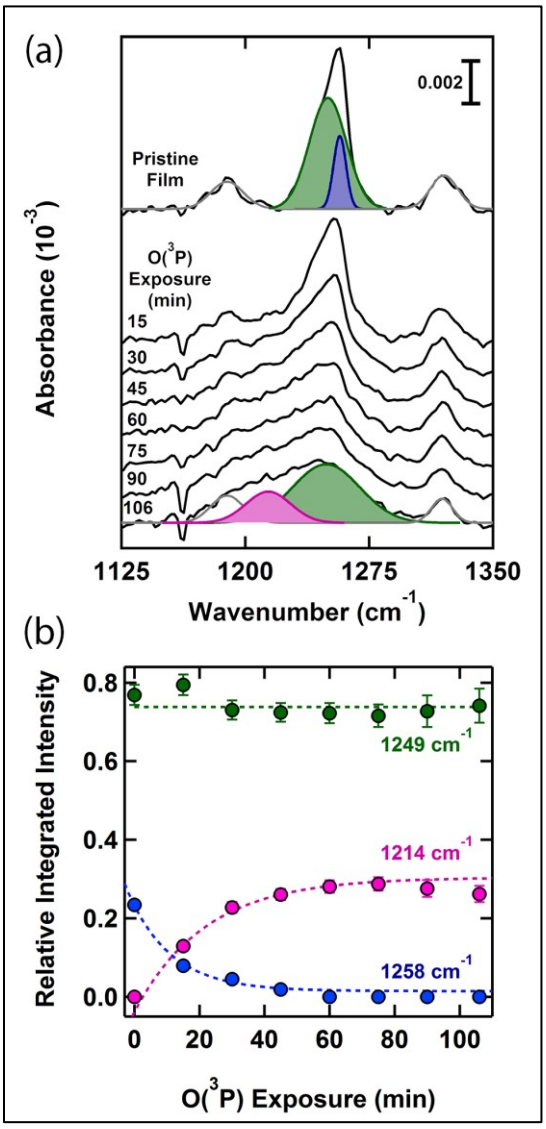

Behavior of P=O modes of DMMP during exposure to O(^{3}P). (a) *P=O signals throughout exposure are deconvoluted into contributions from three signals at 1258 cm^{-1}, 1249 cm^{-1}, and 1214 cm^{-1}. Individual peaks are shown to illustrate the decay of the 1258 cm^{-1} peak coupled with the emergence of the 1214 cm^{-1} peak during exposure (O(^{3}P) flux = 2.9 x 10^{16} cm^{-2} s^{-1}).* ***(b)*** *Corresponding integrated areas of the P=O stretching peaks demonstrate that the 1249 cm^{-1} peak is unaffected by O(^{3}P) exposure, while 1258 cm^{-1} and 1214 cm^{-1} peaks exchange intensity. Dotted lines are drawn to guide the eye. Error bars, where visible, indicate one standard deviation with respect to the peak fitting.*

hydrogen bonding or direct physisorption to surface metal (Lewis acid) sites.[144,153,157,161,191] While the overall intensity in this region is unchanged during exposure, there are a number of significant changes in the peak shape. Prior to O(^{3}P) exposure, the P=O stretch can be deconvoluted into separate signals at 1249 cm^{-1} and 1258 cm^{-1}. These peak locations are consistent with recorded values for DMMP adsorbed on unreactive, non-hydroxylated surfaces.[161–163] Exposure to O(^{3}P) causes the intensity of the 1258 cm^{-1} peak to decrease, replaced by a new signal at 1214 cm^{-1}, highlighted in **Figure 5-4(*b*)**. This shift is consistent with DMMP coordination with hydroxlyated metal oxides or other hydroxyl-terminated surfaces, in which the P=O stretch is weakened and red-shifted by the formation of one or two hydrogen bonds.[149,150,161] Further corroborating this assignment is a separate control experiment performed where a DMMP monolayer was deposited on a fifty- to sixty-layer thick amorphous solid water film at 125 K. Detailed in **Figure 5-5**, a comparison of the P=O signals of one DMMP layer deposited on Au(111) versus water ice shows a red shift identical to that observed upon exposure of a multilayer film to O(^{3}P). Finally, this shift is also consistent with DMMP solvation in the liquid phase.[163,192]

Importantly, only one of the two initial P=O peaks is impacted by O(^{3}P) exposure; the 1249 cm^{-1} peak remains essentially unchanged (**Figure 5-4(*b*)**) except for some broadening. In order to explain this disparity, it is important to identify the two initial peaks. One possible explanation is conformational; DMMP is reported to have at least two low energy conformers in both the solid and gas phase.[144,170,193–196] Electronic structure calculations predict that the P=O peaks for the two lowest-energy conformers in the gas phase could be as little as 2 cm^{-1} apart.[196] On the other hand, a splitting of 20 cm^{-1} between conformers has been interpreted from FTIR spectra of solid- and liquid-phase DMMP.[194] Our observed splitting of ~9 cm^{-1} is within this range, but the lack of agreement complicates definitive assignment. A supplemental explanation may involve the

Figure 5-5

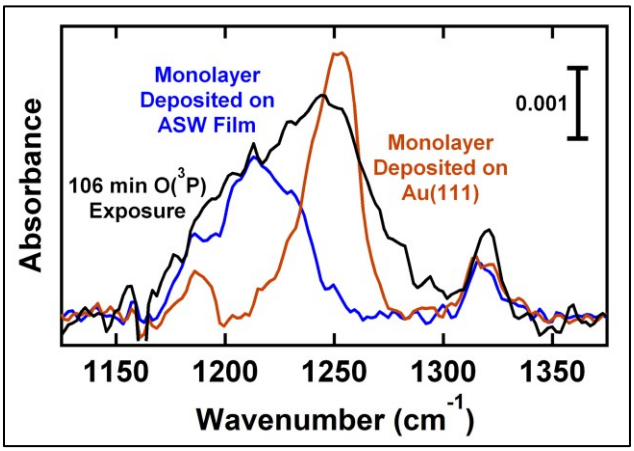

Experimental justification for post-exposure DMMP's P=O peak assignment. *The appearance of the 1214 cm^{-1} peak in the spectrum of a six-layer DMMP film exposed to $O(^3P)$ for 106 minutes (black, 2.9 x 10^{16} atoms cm^{-2} s^{-1}) is compared to the spectra of a DMMP monolayer deposited on clean Au(111) (gold) versus on thick amorphous water ice (blue). This peak's position is consistent with the observed red-shift of the monolayer deposited on water ice, indicative of new hydrogen bonding interactions with the phosphoryl group of DMMP as a result of $O(^3P)$-induced reactivity.*

organization of DMMP in the solid film. It has been suggested that spectroscopic signals associated with DMMP aggregates appear between 1240-1250 cm^{-1}.[194] A consequence of DMMP aggregates would likely be two general molecular environments. The reactive 1258 cm^{-1} peak could potentially represent molecules at the boundaries of such aggregates, while the 1249 cm^{-1} peak, mostly unchanging during exposure to $O(^3P)$, could correspond to DMMP molecules within the interior of these aggregates. This latter notion is supported by spectroscopically observing DMMP growth, in which the two peak intensities were tracked as DMMP was deposited. The 1258/1249 integrated intensity ratio remains constant from one layer and beyond, eliminating the possibility that the 1258 cm^{-1} peak corresponds simply to DMMP at the vacuum- or substrate-film interfaces.

Product Formation

Evidence of partial DMMP film destruction is given by the decrease in intensity of the P-O-C stretching modes; this is corroborated by consistent decreases in the C-H stretching mode region below 3000 cm^{-1} upon $O(^3P)$ exposure. At the film thicknesses studied, however, the IR intensity for these modes are weak and preclude more detailed spectral analysis. We support the proposed mechanism by citing recent theoretical calculations for collision dynamics between DMMP and $O(^3P)$ in the gas phase, the results of which indicate that hydrogen abstraction is the most energetically accessible reaction channel. The calculated upper limit for the gas phase barriers are 0.14 and 0.36 eV for abstraction from the methoxy or methyl groups, respectively.[185,186] These barriers are, however, likely lower in the solid phase due to formation of longer-lived collision complexes in the film. Furthermore, experimental evidence suggests that reactions between $O(^3P)$ and organic or hydrocarbon-based films does proceed largely through the abstraction mechanism.[197–199] In the present study, hydrogen abstraction would naturally yield hydroxyl radicals as products:

$$O{=}P(CH_3)(OCH_3)_2 + O(^3P) \longrightarrow O{=}P(CH_3)(OCH_3)(OCH_2)^{\bullet} + {}^{\bullet}OH \qquad \textbf{(5-1)}$$

These reactive species can be expected to undergo further reactions within the film. For example:

$$O{=}P(CH_3)(OCH_3)(OCH_2)^{\bullet} \longrightarrow O{=}P(CH_3)(OCH_3)^{\bullet} + OCH_2 \qquad \textbf{(5-2)}$$

Reaction (5-2), in particular, could help explain the observed methoxy group loss during exposure. **Figure 5-6** contains a plot of all aggregated data collected, arranged to show methoxy group loss as a function of $O(^3P)$ exposure. The ordinate axis values estimate that a DMMP monolayer is comprised of 6 x 10^{14} molecules cm^{-2} *via* its gas phase geometry,[143] and take into account that there are two methoxy groups per DMMP molecule. The observed reactivity does not follow simple first-order, or even half-order kinetics with respect to $O(^3P)$ exposure; the observed behavior is likely the product of numerous reactions contributing to the observed spectroscopic changes. We can, however, consider the initial reactivity to get a sense for the initial reaction probability. A linear fit to the data early in the exposure (solid circles in **Figure 5-6**) shows that in the first stages of reaction, a methoxy group is lost for roughly every 50,000 $O(^3P)$ dosed onto the surface. If direct reaction occurs, this rather low probability could be a result of only a fraction of the incident $O(^3P)$ having sufficient energy to overcome the barrier. Otherwise, after collision and exchange of energy with the film, $O(^3P)$ would then have to diffuse both along and through the vacuum-film interface to encounter a methyl group.

Changes in the P=O region of the spectra during reaction also suggest formation of hydroxyl species, given that conversion of signal from 1258 cm^{-1} to 1214 cm^{-1} is consistent with "solvation" of phosphoryl oxygens *via* hydrogen bonding.[163,192] It is worth noting that phosphoryl stretching modes of organophosphorus compounds are also influenced by inductive effects from other functional groups attached to the central phosphorus atom.[200] However, all reaction routes

Figure 5-6

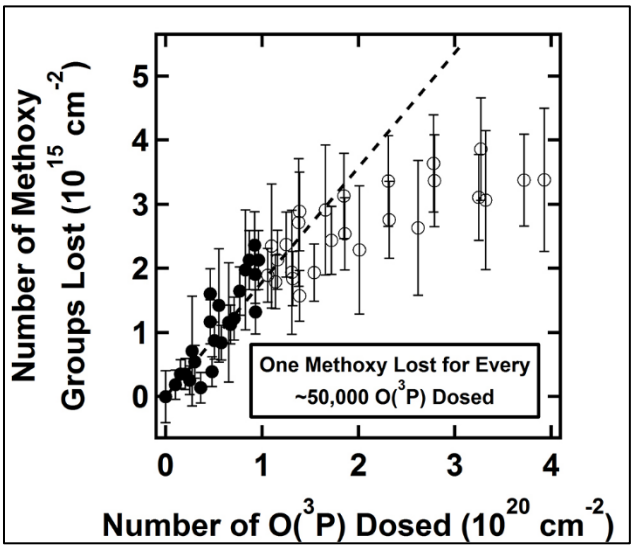

Approximation of DMMP's initial methoxy group destruction probability. *Aggregated data for all experiments showing methoxy group loss from DMMP as a function of $O(^3P)$ exposure. A linear fit to the data early in the exposure (solid circles) shows that one methoxy group reacts for approximately every 50,000 $O(^3P)$ dosed onto the surface. See text for details regarding the estimation of the ordinate data from the infrared spectra.*

considered in the aforementioned theoretical studies—hydrogen abstraction, hydrogen elimination, and methyl elimination—would not result in a redshift of this mode.

XPS data displayed in **Figure 5-7** suggest that in addition to carbon loss, possibly as gaseous CO or CO_2,[174] the reaction results in incorporation of oxygen into the film. Comparison of C(1s) and O(1s) signals between a reacted film and a pristine film, normalized to respective film thicknesses, shows a definitive increase in the relative N_O/N_C ratio at the surface. Reactions with $O(^3P)$ and OH radicals would leave radical intermediates that could also react with non-dissociated O_2 present in the molecular beam.[201] Thus, there are at least three sources of oxygen resulting from exposure to the beam that are likely contributing to the observed uptake of oxygen in the DMMP film upon beam exposure. These various uptake pathways are further supported by the O(1s) peak shapes before and after $O(^3P)$ exposure. On a pristine DMMP film, the O(1s) spectrum is comprised of two signals, attributed to the methoxy and phosphoryl oxygens in DMMP. After $O(^3P)$ exposure, however, the O(1s) signal is no longer so neatly deconvoluted into distinct oxygen chemical environments.

A slight signal increase near 3300 cm^{-1}, indicative of hydroxyl group formation, is observed during exposure to $O(^3P)$, but the rate of growth is convoluted with the small amount of background water deposition expected under our conditions (4-8 x 10^{-11} Torr based on readings from a residual gas analyzer). It is important to note, however, that the observed P=O shift does not take place without exposure to $O(^3P)$. DMMP films left in the chamber for periods of time equal to that of an experiment (two hours on average) show no spectroscopic change except for slight growth in the OH region amounting to less than half a layer of water (one layer = 1.07 x 10^{15} H_2O molecules[97]). Moreover, the films remain unchanged when exposed to a pure neon plasma and a mixture of 5%

Figure 5-7

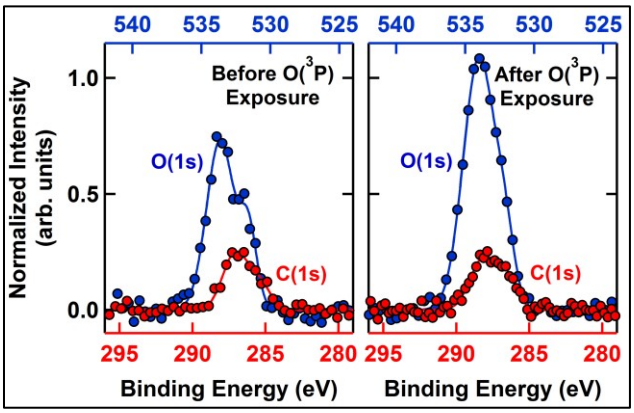

XPS of post-exposure DMMP film showing uptake of oxygen. *Representative XPS data comparing DMMP films as deposited and after exposure to $O(^3P)$ show that the N_O/N_C ratio increases as a result of oxygen uptake by the film. To emphasize this effect, the data are scaled such that the carbon 1s peak areas are equivalent; this accounts for the fact that some carbon is also lost as gaseous species during reaction.*

O_2 in helium (no plasma; approximation of O_2 with higher translational energy present in O_2/Ne plasma). We thus conclude that these changes are initiated by reaction of the film with $O(^3P)$ and cannot simply be attributed to background water sticking to the vacuum-film interface.

The remaining P-O-C and P=O stretching mode signals of films having an initial thickness below ten layers (*e.g.* **Figures 5-3 and 5-4**) are clearly broadened with respect to the pristine peaks, indicating disordering. The close spatial proximity of radical intermediates could promote formation of polymeric species on the surface, which have been reported at least once in the literature under related circumstances.[176] To test this hypothesis and monitor the thermal stability of the reaction products on the surface *in situ*, isothermal desorption experiments were performed by increasing the surface temperature in a stepwise fashion and obtaining RAIR spectra at each temperature. The surface temperature was ramped up from 155 K in 10 K increments at 1 K s^{-1} and held constant during the duration of an IR scan (roughly three minutes) between each step. Results were compared to a pristine film subjected to identical treatment, and a summary is given in **Figure 5-8**. From these data we can conclude that a reacted film's thermal stability on the Au(111) substrate differs dramatically from that of the pristine film. Whereas the total P-O-C and P=O integrated intensities of the pristine film are effectively zero by the time the surface temperature reaches 195 K, these peaks are readily observable at 245 K and beyond for the reacted film. Indeed, the most dramatic changes occur during the ramp from 185 K to 195 K for a pristine DMMP film, as emphasized in **Figure 5-9(*a*)**. This behavior is mirrored in the reacted DMMP film shown in **Figure 5-9(*b*)**, where the non-reacted DMMP molecules freely desorb, leaving behind the polymeric species, and therefore some intensity at 1249 cm^{-1}. The new signal at 1214 cm^{-1} stays essentially constant during the ramp (**Figure 5-9(*c*)**) and therefore directly corresponds to the

Figure 5-8

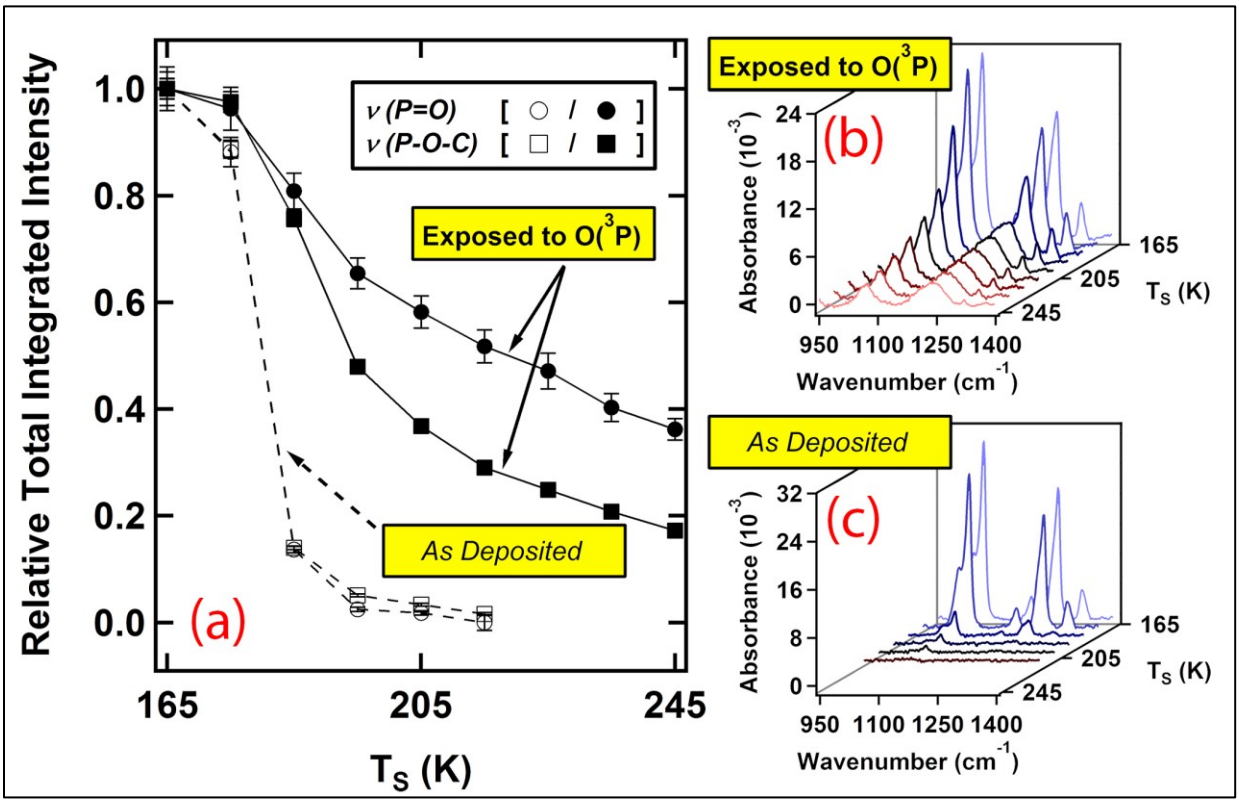

Enhanced post-exposure thermal stability of DMMP. (a) *Stepped isothermal desorption experiments (see text for details) show that after reaction of a DMMP film with O(^{3}P), a portion of the film exhibits substantially greater thermal stability on the substrate. The P-O-C and P=O modes still exhibit appreciable intensity in spectra of reacted films collected at surfaces temperatures above ~195 K as compared to the pristine film as deposited on Au(111). The respective spectra are given in waterfall plots* ***(b)*** *and* ***(c)****.*

Figure 5-9

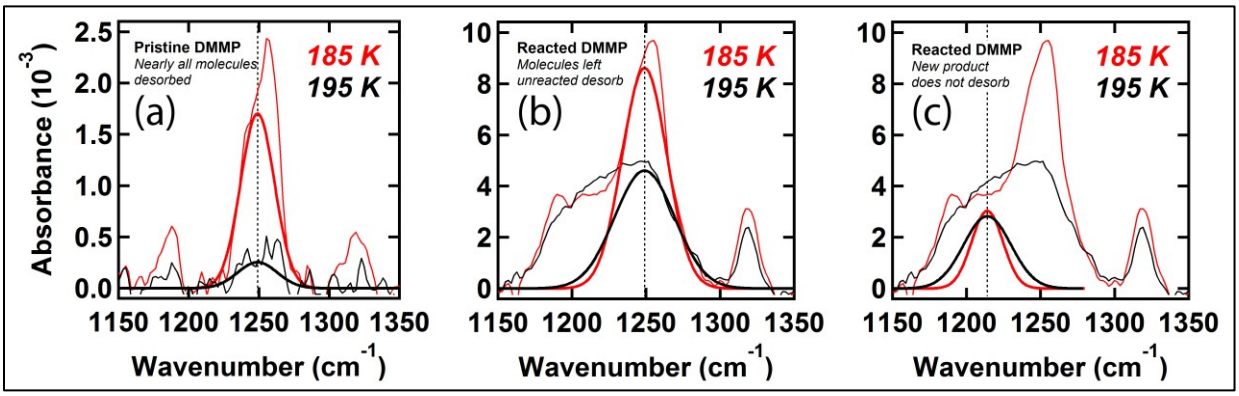

Behavior of DMMP's deconvoluted P=O signals during isothermal desorption. *Behavior of the deconvoluted P=O spectroscopic signals of DMMP during isothermal desorption of films both pristine and exposed to $O(^3P)$. The majority of a pristine DMMP film desorbs on the ramp from 185 K to 195 K, as shown in* ***(a)****. This behavior, shown in* ***(b)****, is mirrored in a reacted DMMP film, where the non-reacted DMMP is free to desorb, leaving behind the polymeric species, and therefore some intensity at 1249 cm^{-1}. Given that its intensity stays essentially constant during the ramp, the new signal at 1214 cm^{-1} is therefore directly related to formation of the new, more thermally stable polymeric product, shown in* ***(c)****.*

presence of the new, more thermally stable polymeric product. Reacted films further show a clear difference in desorption kinetics between the P-O-C and P=O groups (**Figure 5-8(*a*)**), and we propose that the combination of increased surface energy and trapped oxygen species induces additional secondary reactions within the film during thermal annealing. These reactions further destroy DMMP methoxy groups, leading to a faster observed rate of decay in those particular infrared signals.

Hydrogen-bonded phosphoryl groups (1214 cm^{-1}), as mentioned previously, are products of the reactions taking place on the surface, and based on the desorption evidence they are likely part of a hydroxylated polymerized species that has significantly greater thermal stability on the surface. In **Figure 5-10**, product formation resulting from reactions of $O(^3P)$ with six, twelve, and thirty-six layer DMMP films begins to terminate at similar absolute signal intensities on all films studied. If the reaction begins at the vacuum-film interface and progresses layer-by-layer into the bulk DMMP, this trend suggests a limit to the penetration depth of the reactive species. Given substantial film thickness, a fraction of the DMMP—presumably underneath—is unchanged under our reaction conditions and is left free to desorb from the surface normally upon heating. Coupled with the decay kinetics mentioned previously, reaction energetics presented here seem to preclude the ability for $O(^3P)$ to erode thicker DMMP films all the way down to the substrate; we hypothesize that the polymeric overlayer formed hinders continued destruction. It is therefore likely that the effectiveness of surface DMMP decontamination through use of atmospheric plasmas cited in the literature[175–179] is facilitated by thermal desorption or sputtering in addition to reactivity with oxygen species.

Figure 5-10

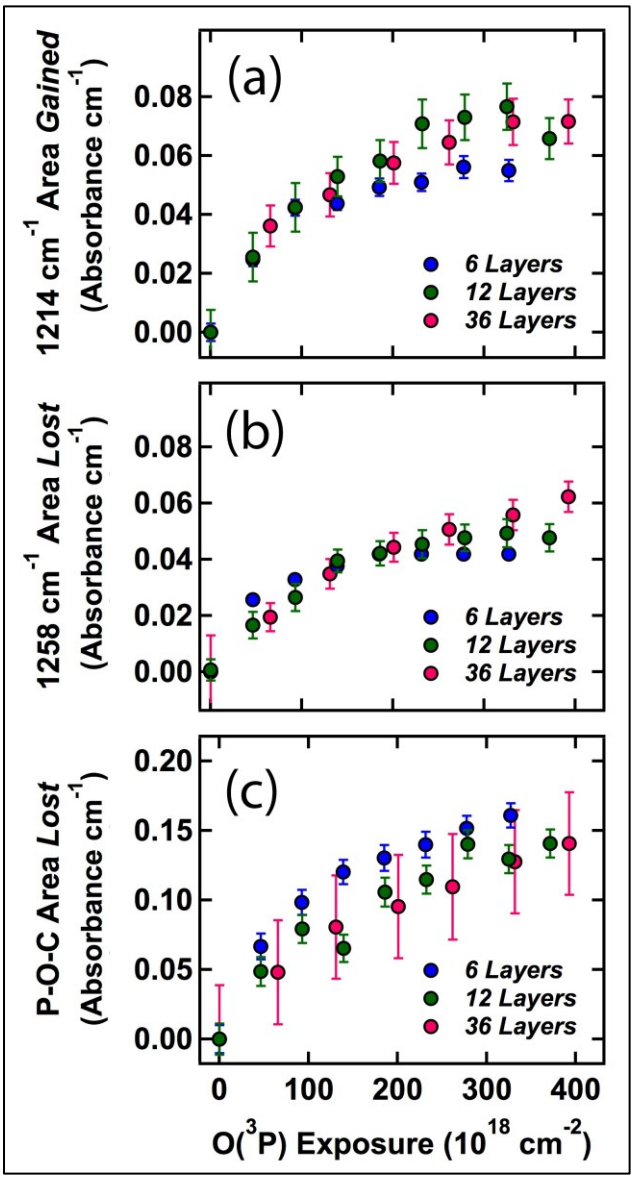

Independence of reactivity from initial DMMP film thickness. *RAIR spectra obtained for six, twelve, and thirty-six layer DMMP films during exposure to $O(^3P)$ suggest that reaction probability decreases as exposure continues, but does not follow half- or first-order kinetics. Panels depict (a) intensity gained in the 1214 cm^{-1} peak, (b) intensity lost from the 1258 cm^{-1} peak, and (c) total intensity lost from the P-O-C stretching modes. Overlap of the data asserts that reactivity is independent of initial film thickness and originates at the vacuum-film interface. Error bars, where visible, indicate one standard deviation with respect to the peak fitting.*

Conclusion

The oxidative reactivity of solid multilayer DMMP by $O(^3P)$ has been characterized using time-resolved RAIRS and complemented by XPS. Our analysis suggests that destruction is initiated *via* hydrogen abstraction from methyl or methoxy groups. In turn, resultant hydroxyl and DMMP radical intermediates formed subsequently react with surrounding DMMP molecules, and also potentially with additional O_2 present in the beam under our conditions. While XPS confirms that some carbon is lost from the surface, it also shows oxygen incorporation within the film resulting from continued exposure. At 155 K, 0.12 eV $O(^3P)$ atoms do not destroy thicker ($\gtrsim$ ten layers) DMMP films all the way down to the substrate on which they are deposited. We propose that the radical side-reactions initiated by $O(^3P)$ under our experimental conditions yield hydroxylated polymers whose presence hinders continuous destruction of a significant fraction of thicker DMMP films. Despite this observed resistance, unreacted DMMP can freely desorb from the Au(111) surface upon thermal annealing, leaving the polymeric products behind.

These findings better inform the exploration of oxidative decontamination and destructive methods for nerve agents. Based on our observations, the observed efficacy of atmospheric plasma decontamination treatments possibly stems from a combination of the presence of $O(^3P)$, local heating, and sputtering. Additionally, the oxidation-induced formation of a thermally stable polymeric coating may supplement the understanding of these compounds' known flame retarding properties. To this end, our work naturally leads to further investigation into the role of local heating on the destruction of DMMP on surfaces both reactive and inert. Moreover, fruitful extension of this work would involve examining reactivity on model environmental surfaces such as SAMs, ices, and biopolymers, leading to better understanding regarding the limits of effective decontamination following dispersal in a chemical/biological warfare environment.

Chapter 6

Oxidative Destruction of Multilayer Diisopropyl Methylphosphonate Films by O(^{3}P) Atomic Oxygen

We present work detailing the oxidative destruction of the nerve agent simulant diisopropyl methylphosphonate (DIMP) with O(^{3}P) using time-resolved, *in situ* reflection absorption infrared spectroscopy (RAIRS) and x-ray photoelectron spectroscopy (XPS). Thermally annealed DIMP films deposited on Au(111) are observed to react upon exposure to a supersonic beam containing O(^{3}P) with average translational energies of 0.12 eV. The reaction is initiated by a hydrogen abstraction from one of three possible sites on DIMP, and then progresses through various secondary reactions with resultant hydroxyl radicals, carbon-centered DIMP-derived radicals, and non-dissociated O_2 in the beam. These reactions are accompanied by uptake of oxygen into the film, leading to new hydrogen bonding with the DIMP phosphoryl group. The generated product also presents greater thermal stability than pristine DIMP, suggesting the formation of a polymeric product. As reactivity is observed to decrease upon continued O(^{3}P) exposure, this polymeric product likely forms a protective layer at the vacuum-film interface, hindering destruction of thicker films. Importantly, the rate of reaction and general reactivity trends are the same between DIMP and the smaller simulant dimethyl methylphosphonate (DMMP). The comparable reaction rates of the two molecules coupled with oxygen's inability to erode thick films all the way down to the substrate have specific implications for the development of oxidation-based decontamination strategies for these and other organophosphates in the solid phase.

Introduction

Understanding the oxidative destruction of organophosphates is increasingly essential for national defense and environmental protection.[140,202] Organophosphonate nerve agents like Soman and Sarin remain a significant threat in modern warfare, despite the multi-national treaty aimed at preventing their creation and stockpiling.[139] Additionally, less toxic organophosphates are widely used as pesticides and fire-retardant additives.[203,204] Whether combating dangerous exposure to nerve agents, modeling the environmental impact of pest control measures, or exploring the efficacy of flame retardant coatings, it is critical to understand both the atmospheric and condensed phase destruction pathways, persistence, and dispersal of these compounds.[184,205–207]

In studies of both gas phase and surface adsorbed organophosphate reactivity, it has become clear that oxygen plays a crucial role in the effective destruction of these compounds. Under atmospheric conditions, for example, it is widely accepted that reaction with hydroxyl radicals is the dominant loss process for organophosphates.[201,207–210] The surface-induced, photocatalytic, or thermal destruction of these compounds has also been extensively studied on metals,[141,144,145] metal oxides,[146–155] and nanoparticle assemblies.[158–160] While metal oxides in particular are often successful in decomposing organophosphates through coordination to surface-bound hydroxyl groups, many are limited by the number of active sites and significantly decreased activity upon repeat cycles of adsorption and reaction. Recently, these limitations were partially alleviated by the addition of ozone to the reaction,[173,174] which again highlights the importance of oxygen in the reliable destruction of these compounds. Even in larger-scale decontamination strategies that involve the use of atmospheric pressure plasma sources,[175–179,211] the presence of molecular and atomic oxygen species has been shown to improve overall efficacy.[177,211]

In the current study, we present a detailed picture of the oxidative destruction of multilayer diisopropyl methylphosphonate (DIMP) exposed to $O(^3P)$. This work is, in part, a continuation of a previous publication from our lab examining the oxidative destruction of dimethyl methylphosphonate (DMMP).[138] The mechanistic conclusions presented here for the oxidative reactions of both simulants are additionally informed by theoretical investigations of the interaction between organophosphates and reactive oxygen species.[185,186,207,212] The isopropyl groups in DIMP provide an additional structural similarity with the nerve agent Sarin as well as the possibility of observing alkyl reaction channels unseen in DMMP.[208] Through the use of *in situ* reflection-absorption infrared spectroscopy (RAIRS) and x-ray photoelectron spectroscopy (XPS), we are able to conclusively demonstrate oxidative destruction between adsorbed DIMP and $O(^3P)$ under ultra-high vacuum (UHV) conditions, and compare that to the analogous reaction with DMMP. For both simulants, an oxygen-enriched, thermally stable product is formed upon exposure to $O(^3P)$. Additionally, the overall rate of oxidative destruction is identical between the two molecules, despite the differences in functional groups. As such, the findings contained herein have important implications for the solid phase destruction of organophosphates; future decontamination and environmental modeling techniques will have to take into account the fact that the relative rates, byproducts, and persistence of these compounds may vary greatly between the condensed and gaseous phases.

Experimental Details

All experiments described in this work were performed in a molecular beam scattering instrument described in detail in **Chapter 2**. A triply-differentially-pumped molecular beamline exits into a UHV chamber, in which a single-crystal Au(111) sample is exposed to the beam and the subsequent interfacial changes are monitored in real time using *in situ* RAIRS and XPS.

Most of the experimental details described here are identical to those used in a recent paper on the analogous reaction between O(^{3}P) and DMMP films.[138] One difference, however, is in the method for simulant film deposition. For these experiments, DIMP was dosed on the Au(111) crystal surface through the beam source; 5% O_2 in neon was used as the carrier gas for dosing, and all beam lines were pumped out to remove trace DIMP prior to turning on the O(^{3}P) source for reaction. RAIR spectra were collected with a Nicolet 6700 infrared spectrometer: *p*-polarized IR radiation is reflected from the Au(111) substrate at a 75° incident angle and collected in a liquid-nitrogen-cooled MCT/A detector. Spectra, averaged over 200 scans at 4 cm^{-1} resolution and fit to Gaussian peaks with linear baselines, were used to quantify DIMP film thickness and characterize products and reaction progress during exposure. A representative spectrum of a 27-layer DIMP film is shown in **Figure 6-1**, with the three characteristic regions most frequency referenced herein (P-O-C, P=O, and C-H stretches) highlighted in color. The respective peak assignments are consistent both with expectations and values previously reported in the literature.[153,213–216]

Films were prepared by first dosing DIMP onto the substrate at 165 K, where DIMP desorption is negligible. Immediately following the dosing, films were annealed at 182 K until the desired initial thickness was reached. In order to correlate RAIRS signal with a particular DIMP film thickness, isothermal desorption experiments were performed within the range 173-175 K. By tracking the integrated area of the P-O-C signals over time, it was possible to distinguish multilayer from monolayer DIMP. As shown in **Figure 6-2**, the rate of desorption changes abruptly upon reaching the monolayer, which allows for the quantitative determination that a monolayer of DIMP corresponds to an average total integrated P-O-C intensity of 0.07 Absorbance units cm^{-1} using our current setup. This value was used to quantify initial DIMP film thicknesses for all trials; peak line shapes remained consistent beyond 30 layers, the maximum thickness referenced in this study.

Figure 6-1

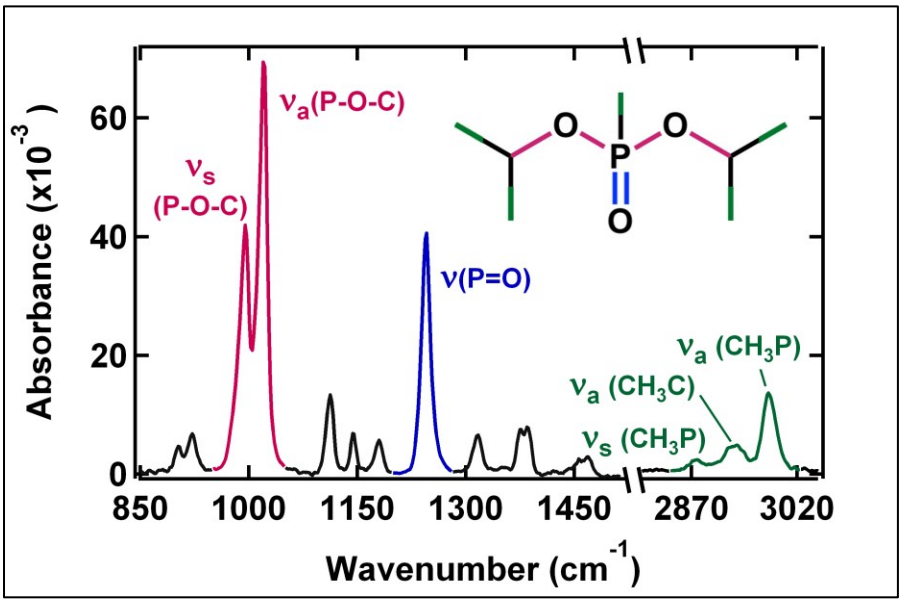

Representative RAIR spectrum of DIMP film. *RAIR spectra of a 30-layer thick DIMP film deposited on single-crystal Au(111). Signals referred to in the text include the P-O-C (pink; 995 and 1020 cm^{-1}), P=O (blue; 1245 cm^{-1}), and C-H (green; 2880, 2931, and 2981 cm^{-1}) stretching modes. All modes are highlighted in the DIMP spectrum and molecule inset.*

Figure 6-2

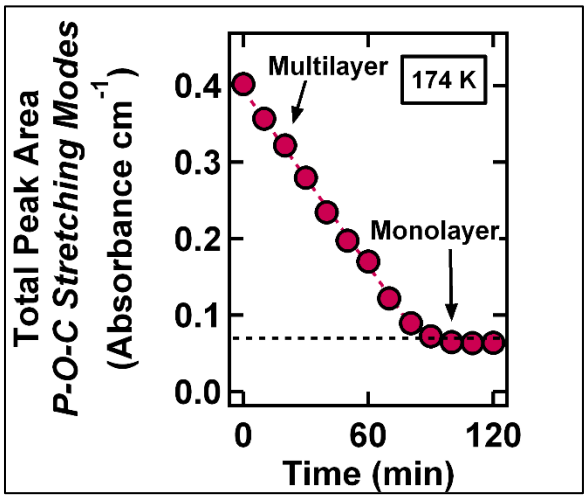

DIMP absorptivity quantification via isothermal desorption. *Isothermal desorption of a DIMP film at 174 K shows a clear distinction between multilayer and monolayer desorption rates, as tracked via integration of P-O-C signals. The value at which the rate changes corresponds to the infrared intensity of a single layer of DIMP.*

Supersonic expansions of atomic oxygen were generated through the use of a radio frequency plasma source described previously.[6] In brief, ignition of a starting gas mixture of 5% O_2 in neon results in expansions containing 35-60% $O(^3P)$. We conclude that our beam is virtually devoid of the potentially reactive species O^+ and $O(^1D)$ due to the use of a 2000 V cm^{-1} deflecting field region and careful selection of low RF power and gas backing pressure. $O(^3P)$ flux and translational energy is calculated *via* time-of-flight experiments. The pressure rise in the chamber (as measured with a nude Bayard-Alpert ion gauge), the chamber pumping speed, the relative sensitivity of the gauge to O_2,[104,190] and the spot size on the Au(111) crystal were used to calculate the flux of a neat O_2 beam.[59] Once the fraction of O_2 dissociation was determined for a particular experiment, the integrated peak areas of O_2 time-of-flight spectra obtained with an in-line quadrupole mass spectrometer were used to calculate the total $O(^3P)$ flux. Typical average translational energies and fluxes of $O(^3P)$ from the beam impinging at normal incidence were, respectively, 0.12 eV and 2 x 10^{17} atoms cm^{-2} s^{-1}. The average beam energy distribution width was 0.07 eV.

It is important to note that while the experimental conditions for $O(^3P)$ exposure are the same as our recent study, all of the DIMP reactivity experiments discussed herein involved significantly greater *total* $O(^3P)$ exposures than those in the aforementioned DMMP publication.[138] As such, DMMP experiments were repeated with this increased exposure to better compare the two molecules. This change did not significantly alter any of our previous conclusions; the details of any minor refinements are referenced in the discussion section.

For XPS experiments, an Al Kα (1486.6 eV) X-ray source operating at 10 kV and 20 mA irradiated the sample with X-rays at a 45° incident angle. Spectra in the C(1s), O(1s), and Au(4f) regions were collected using a double pass cylindrical mirror analyzer with a 50 eV pass energy and 0.4 eV step size. Resultant peaks were fit in the same manner as that used in RAIRS analyses, and the

binding energy scale was calibrated in reference to the intense pair of Au(4f) peaks at 87.63 eV and 83.95 eV.[5]

Results and Discussion

Spectral Evidence of Reaction

As with DMMP, numerous transformations are observed in the RAIR spectra of a DIMP film exposed to $O(^3P)$. Changes in four important spectral regions are highlighted in **Figure 6-3** for a 7-layer film. The original peaks associated with pristine DIMP are clearly observed to decrease in intensity upon exposure. In the P-O-C region (**Figure 6-3(*a*)**), it is the 995 and 1020 cm^{-1} signals that decay; these peak locations match reported values for the asymmetric and symmetric P-O-C stretches[153,213–216]. This decay corresponds to reactive destruction of these modes.[138] Concurrent with this destruction, however, two new peaks are observed to grow in at 1041 and 1063 cm^{-1}. The first possibility for the identities of these new signals is that they correspond to the same asymmetric and symmetric P-O-C stretches in a phosphonate ester with smaller alkyl groups. It is reported, for example, that the P-O-CH_3 peak locations are 40-60 cm^{-1} greater than those associated with P-O-iPr,[200] and indeed 1041 and 1063 cm^{-1} are nearly identical to our recorded values for adsorbed DMMP.[138] Alternatively, these signals may be due to the formation of new P-O or P-O-H groups. The locations and broadness of these modes are consistent with reported values for various amorphous or glassy phosphate species.[211,217–221]

The P=O region (**Figure 6-3(*b*)**) undergoes a similar transformation on exposure to $O(^3P)$. The pristine DIMP film has a single peak at 1245 cm^{-1}, which is consistent with reported values for the P=O stretch in gas and liquid phases or adsorbed on unreactive, non-hydroxylated surfaces.[213–216]

Figure 6-3

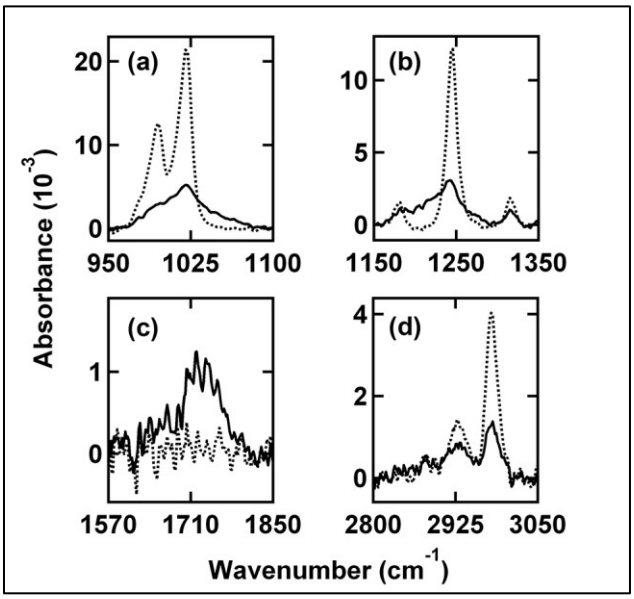

Behavior of DIMP's IR modes during exposure to O(^{3}P). *RAIR spectra of characteristic regions of a 7-layer DIMP film before (dashed line) and after exposure to O(^{3}P) (solid line; total exposure of ~1 x 10^{21} atoms cm^{-2}). Total signal intensity is observed to decrease in the P-O-C* ***(a)****, P=O* ***(b)****, and C-H* ***(d)*** *regions, but new signal growth is also observed in* ***(a)*** *and* ***(b)****. New peaks grow in upon exposure in between 1650-1750 cm^{-1}* ***(c)****. Further explanation of all peak intensity changes and shifts is given in the text.*

With O(^{3}P) exposure, the 1245 cm^{-1} mode decays and is replaced by a new signal at 1216 cm^{-1}. As was reported for DMMP, this red-shifted peak location is the result of the P=O moiety coordinating to surface hydroxyl groups, water, or other hydroxyl-terminated species through hydrogen bonding.[149,167,200,214,222] Therefore, unlike the P-O-C region, the decrease in intensity of the original P=O peak does not correlate with reactive destruction of P=O modes. Rather, the reaction of DIMP with O(^{3}P) generates hydrogen bonding sites within the film, resulting in some fraction of the DIMP becoming partially solvated by hydrogen bonds. This is supported by **Figure 6-4**, which shows the absolute areas lost and gained by peaks in the P-O-C and P=O regions. Clearly, the loss of area in the 1245 cm^{-1} signal tracks almost exactly with the area gained in 1216 cm^{-1}. This is unlike the behavior of the P-O-C peaks, for which area growth and loss appear unrelated. Therefore, the P=O region is exhibiting a red shift in the original band.

In the C-H region (**Figure 6-3(*d*)**), the three original peak locations are consistent with literature values for asymmetric P-CH_3 (2981 cm^{-1}), asymmetric C-CH_3 (2931 cm^{-1}), and symmetric P-CH_3 stretches (2880 cm^{-1}).[153,214,216] All three peaks decrease in intensity during the reaction but no new peaks or shifts are observed, supporting reactive destruction of DIMP. The fact that all three of these modes are observed to decrease in intensity indicates that the system has enough energy to overcome the barriers for reaction at each of the C-H sites visible in the RAIR spectra (P-CH_3 and C-CH_3). The tertiary C-H stretch of the isopropoxy group is unresolved in our spectra, but theoretical barriers for hydrogen abstraction are comparable for both possible sites on the isopropoxy groups, so the reaction is likely occurring at the tertiary site as well.[185,186,207]

The final change observed in the reacted DIMP RAIR spectra yet to be discussed is the growth of a broad pair of peaks at 1645 and 1724 cm^{-1} (**Figure 6-3(*c*)**). Carbonyl-containing species with similar peak locations have been identified as products or intermediates in a number of prior

Figure 6-4

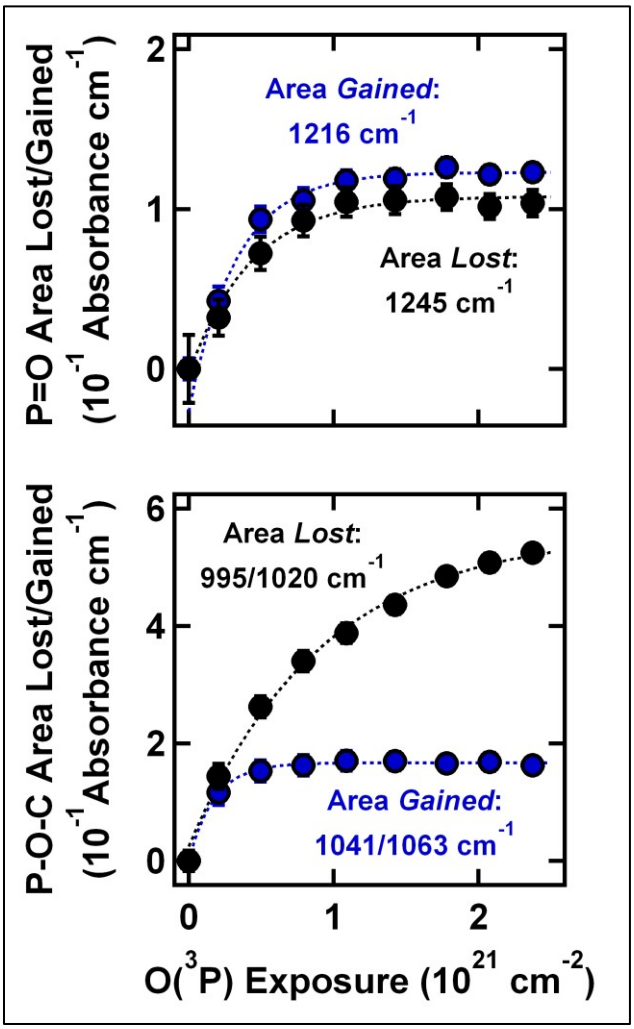

Comparison of P-O-C and P=O modes of DIMP during exposure to O(^{3}P). *Changes in integrated peak areas are shown for the P-O-C and P=O regions of a 27-layer DIMP film. The area lost from peaks associated with pristine DIMP is shown in black (995 and 1020 cm^{-1} for P-O-C and 1245 cm^{-1} for P=O), while the area gained by new peaks is shown in blue (1041 and 1063 for P-O-C and 1216 cm^{-1} for P=O). In the P=O region, intensity shifts away from the original peak due to solvation by new hydrogen bonds. Conversely in the P-O-C region, the original peaks continue to decay in intensity long after the new peaks have stopped growing in.*

organophosphate studies, including destructive adsorption on metal oxides,[150,159,223] gas-phase reactions with hydroxyl radicals under atmospheric conditions,[208] and destruction with a radio frequency plasma source.[211] Probable sources of these new C=O bands are addressed in the next section.

Product Formation

Oxidative destruction of both DIMP and DMMP begins with a hydrogen abstraction step leading to formation of a carbon-centered radical. This is supported by a myriad of both theoretical and experimental work concluding that hydrogen abstraction is the most energetically accessible channel for these organophosphates. We cite, for example, recent theoretical gas phase calculations for $O(^3P)$ and Sarin (nerve gas for which DMMP and DIMP are both simulants), which report that the upper limit for hydrogen abstraction barriers are 0.47, 0.20, and 0.19 eV for abstraction from the methyl, isopropoxy tertiary C-H, and CH_3 sites, respectively.[185,186] While some of these projected barriers are larger than the current study's mean beam energies (accounting for the energy distributions), there are a few reasons why hydrogen abstraction is nevertheless feasible. First, the barriers are likely lower in the solid phase due to formation of longer-lived collision complexes in the film. This assertion is reinforced by experimental evidence indicating that reactions between $O(^3P)$ and organic or hydrocarbon-based films proceed largely through such abstraction mechanisms.[197–199] Second, and perhaps more importantly, while the initial abstraction by $O(^3P)$ may be energetically- or rate-limiting, once a hydrogen has been abstracted, hydroxyl radicals are produced. These hydroxyl radicals can continue reacting within the film, and the barriers for hydrogen abstraction from DIMP by hydroxyl radicals are significantly lower.[207,224] One theoretical study concluded that abstraction from all three possible sites by hydroxyl radicals is facile under atmospheric conditions, with barriers at or below 2kT for our system.[207] These low-

barrier, secondary abstractions help explain why all of the DIMP C-H stretching peaks are observed to decrease concurrently despite the disparity in barriers for direct abstraction by $O(^3P)$.

Spectral changes in the P=O region, as well as XPS analysis, confirm the continued reaction and retention of oxygen-containing species within the film. In the P=O region, the shift in intensity from 1245 cm^{-1} to 1216 cm^{-1} is consistent with the analogous shift observed for DMMP and indicates solvation of the P=O moiety by new hydrogen bonds.[138,163,192] Additionally, XPS data in **Figure 6-5** verify that even when accounting for the loss of gaseous carbon-containing products such as CO and CO_2,[174] comparison of C(1s) and O(1s) signals between pristine and reacted DIMP films shows a substantial increase in the relative N_O/N_C ratio at the surface.

A number of studies have examined the radical reactions of organophosphates under atmospheric and aqueous conditions, and have proposed relevant pathways that provide a useful mechanistic foundation for this work.[201,207–210,212,225–227] Following the rate-determining hydrogen abstraction by $O(^3P)$ or hydroxyl radical, it is likely that O_2 from the beam adds to the resultant carbon-centered radicals, forming peroxy radicals (RO_2•).[207,228–231] These radicals have a number of possible subsequent reaction pathways, including Reactions (1) and (2) detailed in **Figure 6-6**.[228,232,233] Reaction (1) presents a clear explanation for the uptake of oxygen in the film that is observed with XPS, since both of the non-radical products have new oxygen-containing functional groups. Additionally, these products account for both the observed increase in hydrogen bonding within the film and the appearance of bands in the C=O stretching region of the RAIR spectra. Reaction (2), on the other hand, is not a termination reaction and therefore presents yet another set of possible reaction pathways, detailed in Reactions (3) and (4) in **Figure 6-6**.[234–237]

These latter reactions provide further evidence for carbonyl-containing products, as well as a

Figure 6-5

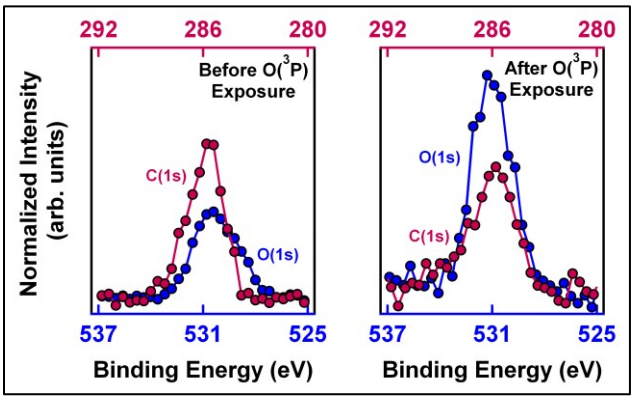

XPS of post-exposure DIMP film showing uptake of oxygen. *XPS data of 17-layer DIMP films as deposited and after $O(^3P)$ exposure demonstrate that the N_O/N_C ratio increases, confirming oxygen is incorporated into the film. The data are scaled such that the carbon (1s) peak areas are equivalent in both films, which accounts for the fact that some carbon is also lost as gaseous species during reaction.*

Figure 6-6

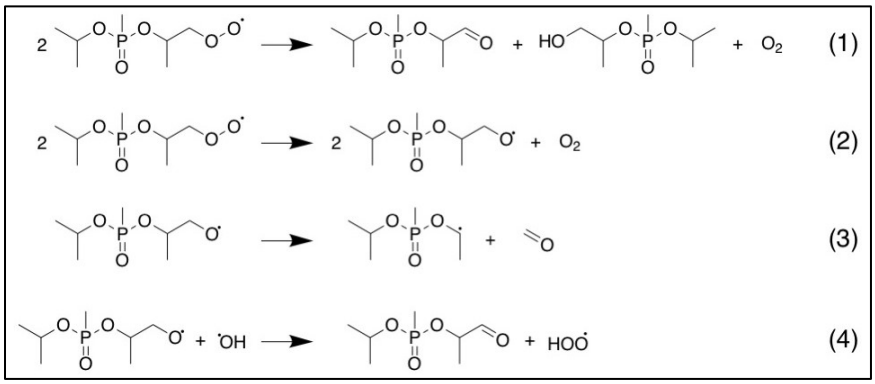

Possible reaction pathways during exposure of DIMP to O(^{3}P). *Possible reaction pathways following the hydrogen abstraction from a primary isopropyl carbon in DIMP and subsequent addition of O_2. Reactions include disproportionation (1) to form carbonyl- and hydroxyl-containing products, as well as conversion to alkoxy radical species (2). Alkoxy radicals can undergo unimolecular decomposition (3) or further reaction with hydroxyl radicals in the film (4).*

product with a smaller alkoxy group, possibly accounting for the new bands observed in the P-O-C region of reacted DIMP. Because the initiating hydrogen abstraction step can occur at all three possible sites, there are, of course, a great many more possible reaction pathways than just those discussed here, including combinations and cross-reactions between different radical species. While gas phase barriers, rate constants, and branching ratios have been reported for many of the analogous alkoxy and peroxy radical reactions and decompositions, they are difficult to reliably apply to such a complex solid phase system, whose spectroscopic bands tend only to broaden and convolute. The spectroscopic evidence and mechanisms presented here do, however, largely align with atmospheric studies of DMMP and IMMP (isopropyl methylphosphonate). The products of the reaction between hydroxyl radicals and IMMP, for example, include formaldehyde and acetone as well as the carbonyl-containing phosphonate, $iPrOP(O)(CH_3)OC(O)CH_3$.[208] A distinct P-O-C=O band is unidentifiable in the data presented here, but this mode possibly overlaps with DIMP's P-O-C stretches or may also simply be too small and broad to detect on top of the lower wavenumber DIMP peaks.[200]

Another consequence of the reactions taking place in a solid film is that reaction products and intermediates are in close spatial proximity. Therefore, it can be expected that some of the combination reactions may lead to larger, polymeric products. Polymeric byproducts have been reported during investigations of the decomposition of organophosphates under both gaseous and surface-adsorbed conditions.[176,180] It is often difficult, spectroscopically, to conclusively identify evidence of P-O-P or P-R-P stretching modes, because they either overlap with other absorption bands or appear as smaller, broader peaks.[200] Instead, evidence of a polymeric product is found by monitoring the thermal stability of the film after reaction. After a DIMP film has been exposed to $O(^3P)$, the surface temperature is systematically increased from 165 K to 350 K at 0.05 K s^{-1} and

held constant at a series of intermediate temperatures for the duration of a spectrum acquisition. For comparison, a pristine film is subjected to identical treatment. A representative summary of this data for the P-O-C region is given in **Figure 6-7**. Clearly, the thermal stability of a reacted DIMP film is much greater than that of a pristine film. As the RAIR spectra inset shows, unreacted DIMP is fully desorbed by 200 K, whereas a reacted film retains appreciable intensity at 350 K and beyond. Moreover, when the reacted film does begin to desorb, intensity is lost from the original P-O-C peaks first, indicating that unreacted DIMP is eventually freed. This increase in product stability cannot be explained fully with the initial unimolecular and bimolecular reactions given in **Figure 6-6**. Rather, radical intermediates likely react in a series of steps, forming the observed oxygen-containing species of higher molecular weight.

As observed in **Figure 6-7**, the full retention of spectral intensity for an additional 30 K in a reacted film suggests that even the *unreacted* DIMP possesses some increased thermal stability on the substrate following $O(^3P)$ exposure. A possible explanation for this is that the oxidative reaction begins at the vacuum-film interface and progresses layer-by-layer into the film. The subsequent reactions lead to the formation of a thermally stable, polymeric overlayer on top of the remaining unreacted DIMP. Until the surface temperature is high enough to destroy or increase the mobility of this polymeric overlayer, the unreacted DIMP is effectively trapped on the surface. Evidence for this type of "top-down" reactivity is presented in **Figure 6-8**, which shows the absolute area lost from the original P-O-C peaks in a 7, 17, and 27-layer DIMP film as they are exposed to $O(^3P)$. Regardless of initial film thickness, the reaction progresses at the same rate. The reaction then begins to slow as either the film is completely eroded or, in the case of thicker films, the $O(^3P)$ is simply unable to penetrate and continue reacting in the bulk. This decay, like for DMMP, therefore does not follow simple first or half-order kinetics with respect to $O(^3P)$ exposure. The formation

Figure 6-7

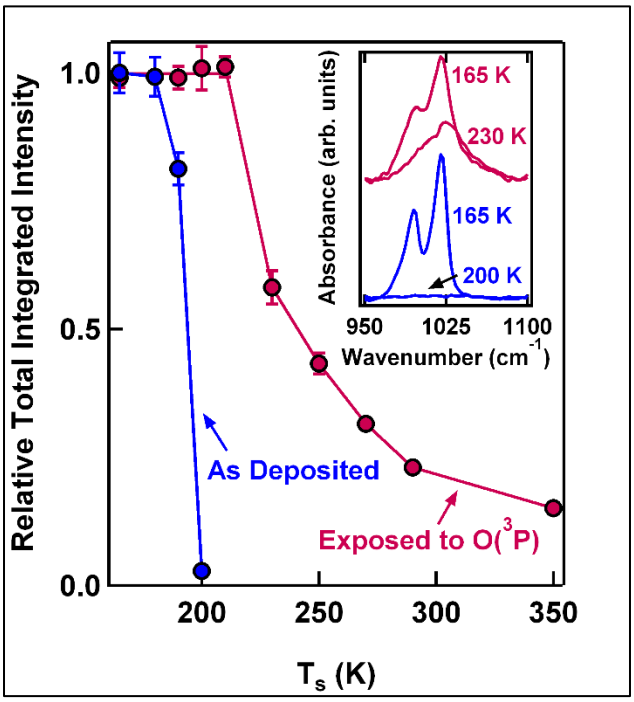

Enhanced post-exposure thermal stability of DIMP. *Stepped isothermal desorption experiments on pristine (blue) and reacted (pink) films show that DIMP exposed to O(^{3}P) exhibits much greater thermal stability on the substrate. In the reacted film, the integrated intensity of the P-O-C region (normalized to original film thickness) begins to decrease at a surface temperature approximately 30 K higher than the point at which the pristine film decreases. RAIR spectra in the corresponding region of each of the simulants are displayed in the inset.*

Figure 6-8

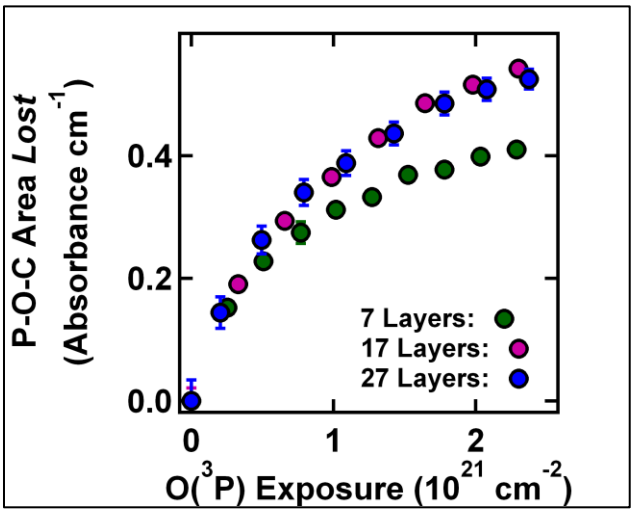

Independence of reactivity from initial DIMP film thickness. *RAIR spectra for 7, 17, and 27-layer DIMP films show that reaction probability decreases with continued $O(^3P)$ exposure. The data shown are the integrated areas lost from the original P-O-C peaks (995 and 1020 cm^{-1}) upon $O(^3P)$ exposure. The overlap of the data confirms that multilayer reactivity is independent of original film thickness and likely initiates at the vacuum-film interface. The earlier turnover of the 7-layer film likely reflects the reaction front beginning to terminate as it approaches the film-substrate interface.*

of the polymeric overlayer thus hinders not only desorption of unreacted DIMP, but also the destruction of thicker films all the way down to the substrate. This experiment was repeated with DMMP under the same heating rate conditions for exact comparison. The same trends emerge: a stark increase in thermal stability of the reacted product, and when desorption begins, it is the unreacted simulant that desorbs first.

Comparison of DIMP and DMMP Reactivity

Qualitatively, there are many similarities in the behavior of DIMP and DMMP films exposed to $O(^3P)$. In **Figure 6-9**, the RAIR spectra of both reacted films show: a decrease in intensity of the asymmetric and symmetric P-O-C stretches, a red shift of intensity in the P=O stretch, and a broad growth between 1650 and 1750 cm^{-1} that we attribute to new C=O stretching modes. The only key difference is the growth of two new, bluer peaks at 1041 and 1063 cm^{-1} in the P-O-C region of DIMP. These peaks are attributed to products or intermediates in the oxidative destruction of

DIMP and are unobserved in DMMP. As such, total reactivity of the two molecules is compared exclusively *via* decay of the original P-O-C peaks. Such a comparison is shown in **Figure 6-10**. Once the P-O-C peak decay is scaled to the integrated intensity of the monolayer (**Figure 6-2**), the reactivity of DIMP and DMMP are clearly identical.

Many of the reaction channels presented here for DIMP are possible for DMMP as well. Differences may, however, be expected in the overall reaction rates for the two molecules, due in part to differences in both initial hydrogen abstraction rates and preference for tertiary hydrogen abstraction in the gas phase.[208,228,231] However, the barriers for all possible hydrogen abstractions in DIMP *and* DMMP are comparable in magnitude, especially when considering abstractions by generated hydroxyl radicals.[185,186,207,224] The replicable decay observed in the C-H peaks of both

Figure 6-9

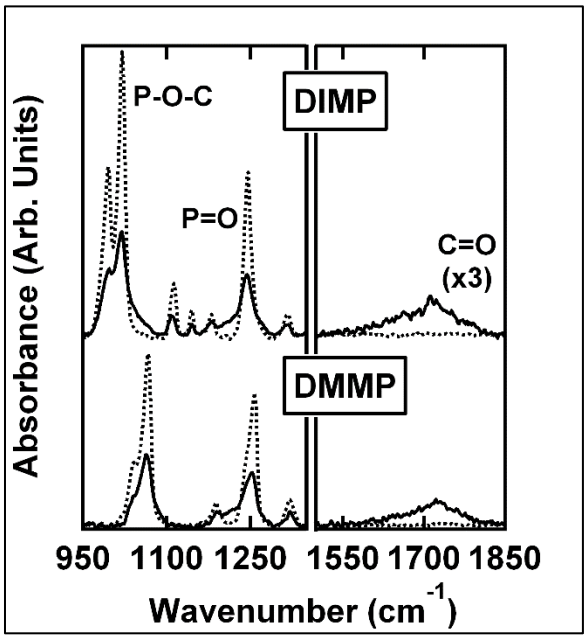

Comparison of changes in DMMP and DIMP films exposed to O(^{3}P). *Analogous changes are observed in the RAIR spectra of pristine (dashed) and reacted (solid) 17-layer DIMP and 12-layer DMMP films. C-H modes are not included here due to their low intensity in DMMP spectra.*

Figure 6-10

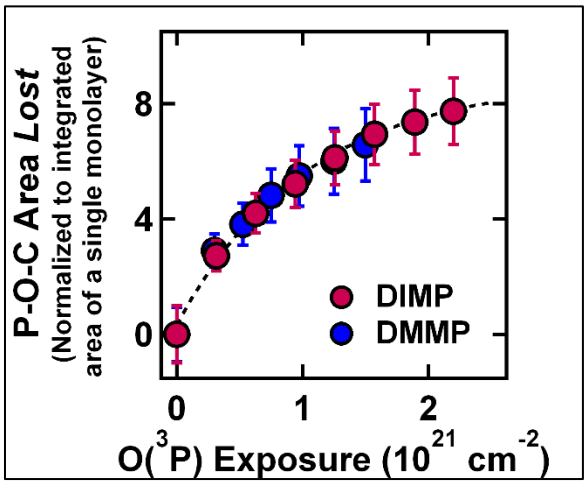

Comparison of reaction rates for O(^{3}P) with DMMP and DIMP. *The integrated area lost from the two original P-O-C peaks of both molecules (995 and 1020 cm^{-1} for DIMP, 1041 and 1066 cm^{-1} for DMMP), scaled to respective monolayer areas. The scaled reaction rates for the two simulants are indistinguishable.*

molecules upon O(^{3}P) exposure attest to the fact that these barriers are indeed accessible by the system. Furthermore, once radicals have begun forming, the close spatial proximity of radical species in the film will likely contribute to a high rate of secondary reactions.[238,239] The multitude of channels available, as well as the accessibility of initial abstractions, leads to the comparable observed overall rates of reaction for DIMP and DMMP in this study.

Conclusion

The oxidative destruction of solid multilayer DIMP by O(^{3}P) has been characterized using time-resolved RAIRS and XPS. The reaction begins with hydrogen abstraction from one of three possible sites on the DIMP molecule by an incident O(^{3}P) or hydroxyl radical intermediate. The resultant carbon-centered radicals go on to either unimolecularly decompose or further react with non-dissociated O_2 in the beam or a neighboring radical in the film. The overall destruction per unit dose decays upon continued O(^{3}P) exposure, independent of film thickness. The products formed during reaction possess greater thermal stability on the substrate than unreacted DIMP, which leads to the conclusion that that at 165 K, 0.12 eV O(^{3}P) erodes the top layers of a DIMP film, forming an oxygen-containing polymeric overlayer that hinders the continued reaction of DIMP fully down to the substrate. Interestingly, the reactions of O(^{3}P) and both DIMP and DMMP progress at the same overall rate and lead to similarly persistent polymeric products. This is in contrast to gas phase analyses that find faster rates of oxidation for DIMP.

These findings aid our understanding of condensed phase organophosphate destruction. For example, protection of unreacted compounds afforded by a polymeric overlayer could explain why organophosphates coating inert particles in the atmosphere have longer lifetimes than their gas phase counterparts.[210] Additionally, the clear importance of organophosphate reactions with

hydroxyl radicals observed here serves to reinforce our understanding of these compounds' known flame retarding properties.[240]

Extension of this work could employ other *ex situ* techniques (*i.e.* MALDI mass spectrometry) to attempt identification of the polymerice overlayer, given its stability at room temperature Another could examine the oxidative destruction of these compounds on a variety of representative environmental surfaces, both reactive and inert (SAMs, water ice, biopolymers). This will aid in developing nerve agent decontamination strategies and refining existing models for the dispersal and destruction of organophosphates in the environment.

Appendix

Raw Data Referenced in All Figures

This appendix contains figures showing the raw data as collected for figures used throughout the thesis. The naming scheme for each figure follows the following convention: '**A**', followed by the chapter where the data appears in a figure (*i.e.* '**2**'), followed by a dash and the number of the raw data figure in the order it appears in the appendix (*i.e.* '**-1**' for the first, '**-2**' for the second, etc.). This number **does not necessarily correspond** to the associated figure's number in the thesis.

In all cases, the figure(s) in which the raw data appear is indicated in the appendix figure's caption.

Figure A2-1

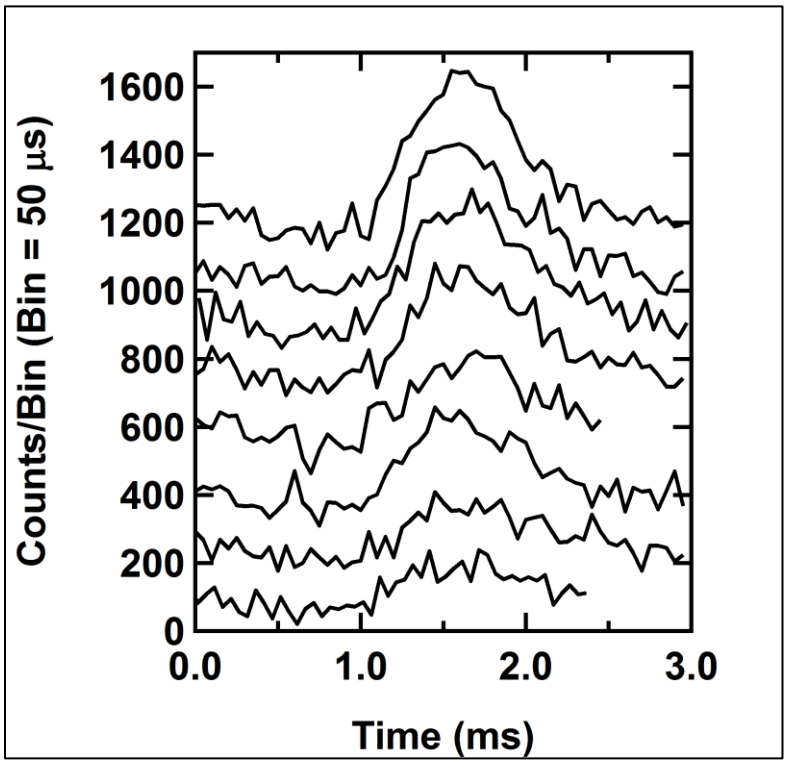

Raw data files: 110316T.F02 – 09. *Raw TOF data captured for O_2 (m/z=32), integrated and used in* **Figure 2-5**, *offset for clarity.*

Figure A3-1

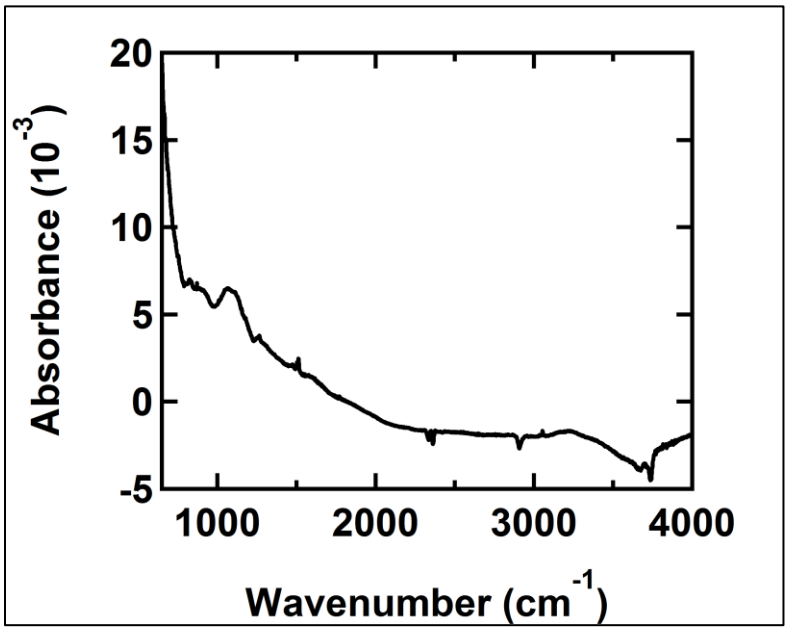

Raw data file: 032513A.IR01. *Raw RAIR spectrum of oPE-SAM, sections of which were used in* **Figure 3-1**, *corrected for background.*

Figure A3-2

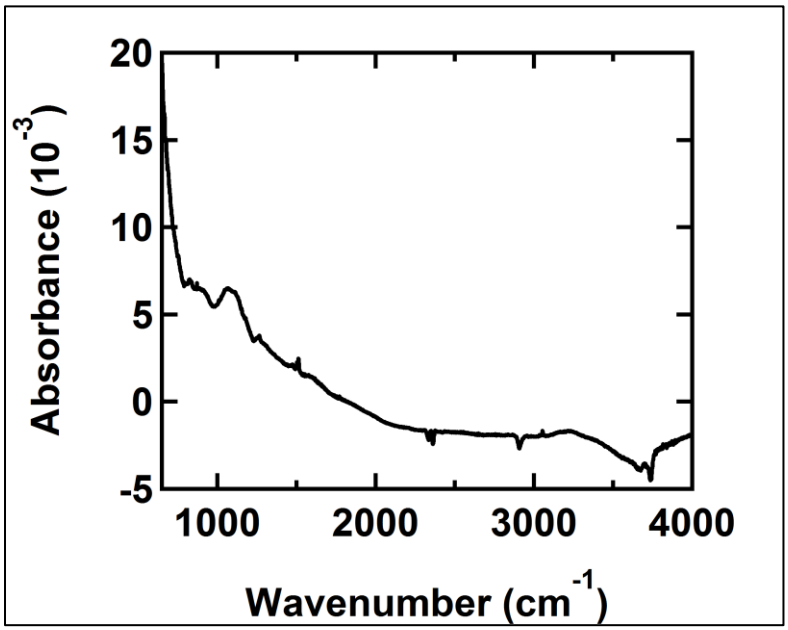

Raw data file: 032513A.IR02. *Raw RAIR spectrum of oPE-SAM after 2-minute exposure to $O(^3P)$ beam (6.3×10^{13} cm^{-2} s^{-1} flux), sections of which were used as the red traces in* **Figure 3-3**, *corrected for background. The black traces in* **Figure 3-3** *are taken from the same raw data as shown in* **Figure A3-1**.

Figure A3-3

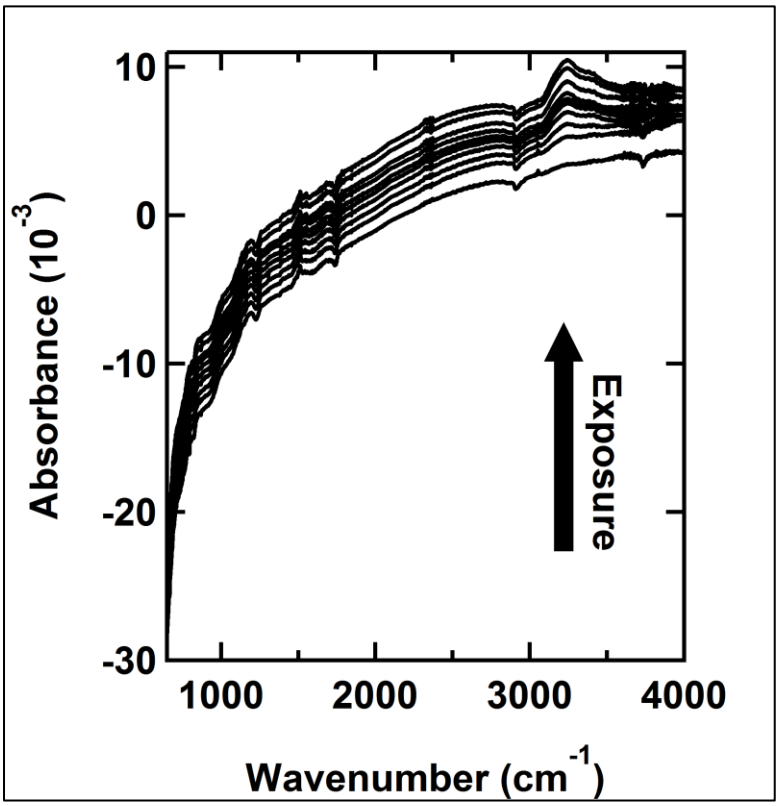

Raw data files: 040813A.IR01 – 10. *Raw RAIR spectra of oPE-SAM before and after 0.5-, 1-, 1.5-, 2-, 3-, 4-, 6-, 8-, and 10-minute exposures to $O(^3P)$ beam (6.2 x 10^{13} cm^{-2} s^{-1} flux), the C-H mode of which were integrated and serve as the data in* **Figure 3-6**.

Figure A4-1

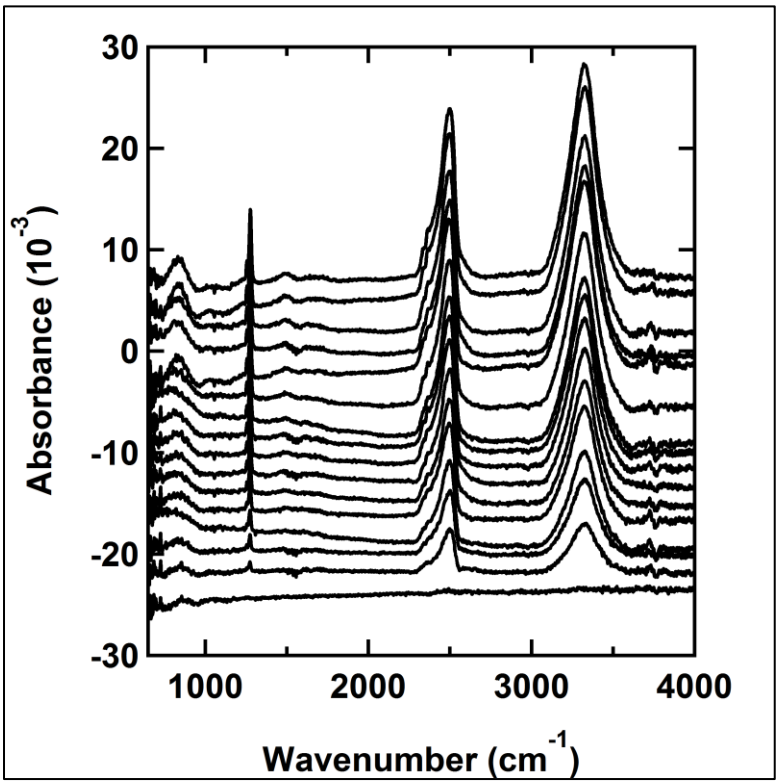

Raw data files: 060914B.IR01 – 16. *Raw RAIR spectra of 60-layer D_2O film before and after 0.5-, 1-, 1.5-, 2-, 2.5-, 3-, 3.5-, 4-, 4.5-, 5-, 5.5-, 6-, 6.5-, and 7-hour exposures to 5.3 eV CF_4 beam (1.9 x 10^{13} cm^{-2} s^{-1} flux), the C-F modes of which were integrated and serve as the data in* **Figure 4-1**. *These data are also curve* **(a)** *in* **Figure 4-6**. *Data are offset for clarity.*

Figure A4-2

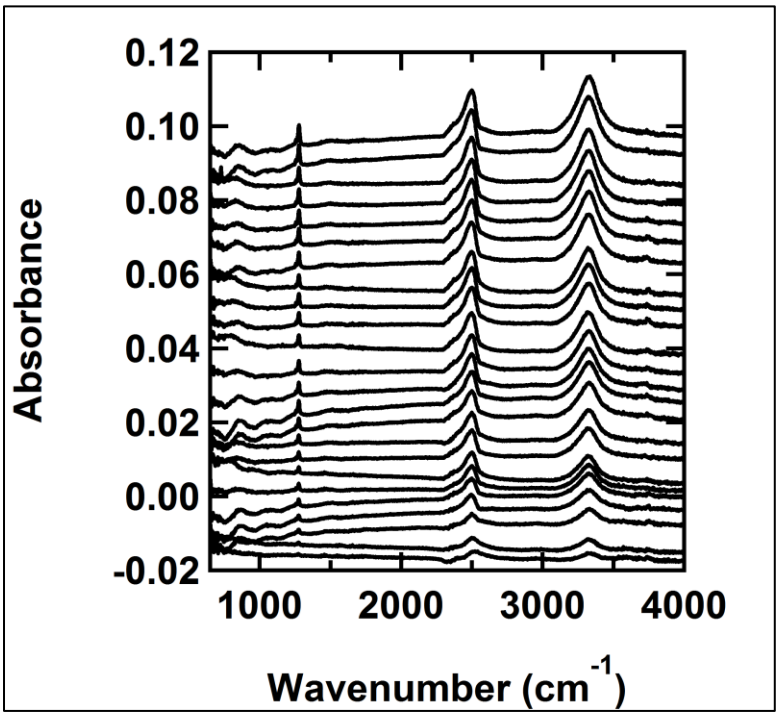

Raw data files: 052214B.IR01 – 25. *Raw RAIR spectra of 200-layer ASW D_2O film after 20-, 42-, 60-, 80-, 100-, 120-, 140-, 160-, 180-, 200-, 220-, 240-, 261-, 280-, 300-, 320-, 340-, 360-, 380-, 401-, 420-, 440-, 460-, and 480-minute exposures to 3.8 eV CF_4 beam (5.9 x 10^{14} cm^{-2} s^{-1} flux), the C-F modes of which were integrated and serve as the data in* **Figure 4-2**. *Data are offset for clarity.*

Figure A4-3

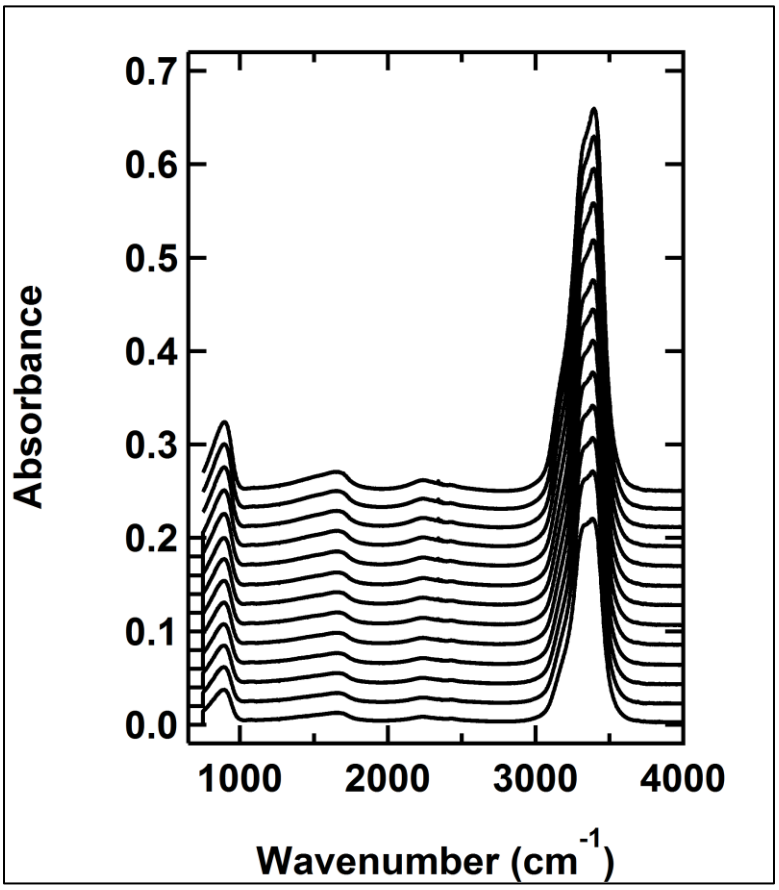

Raw data files: 121114A.IR01 – 13. *Raw RAIR spectra of 60-layer ASW H_2O film before and after 10-, 15-, 20-, 25-, 30-, 35-, 40-, 50-, 60-, 70-, 80-, and 90-minute exposures to 4.1 eV CO_2 beam (1.9 x 10^{16} cm^{-2} s^{-1} flux), whose O=C=O modes at 2341 cm^{-1} were integrated and serve as the data in* **Figure 4-3**. *These data are also curve* **(a)** *in* **Figure 4-5**. *Data are offset for clarity.*

Figure A4-4

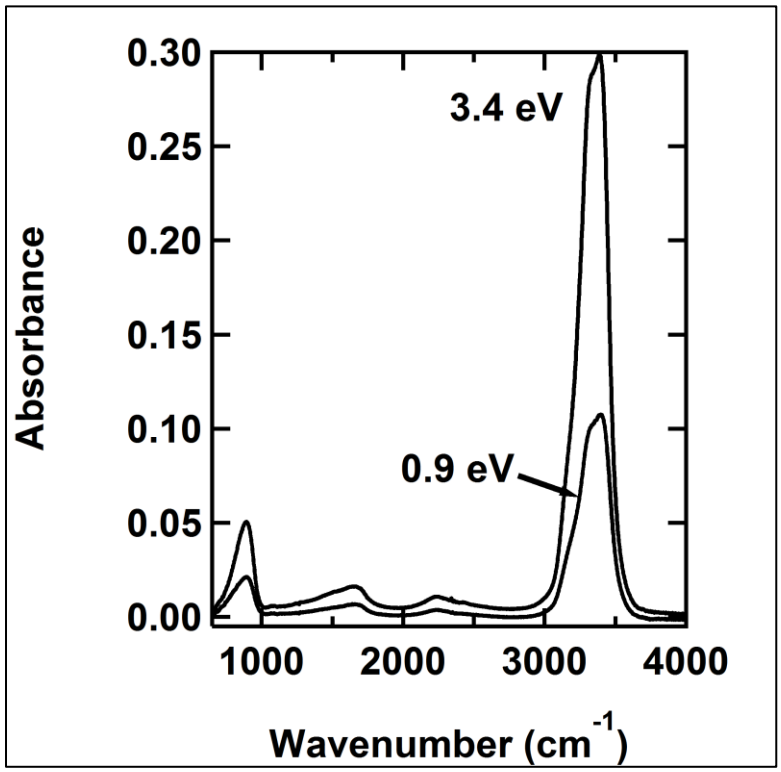

Raw data files: 101314A.IR04, 111314A.IR13. *Raw RAIR spectra of 60-layer ASW H_2O films before and after equivalent total exposures to 0.9 and 3.4 eV CO_2 beams, shown in* **Figure 4-4(a)**.

Figure A4-5

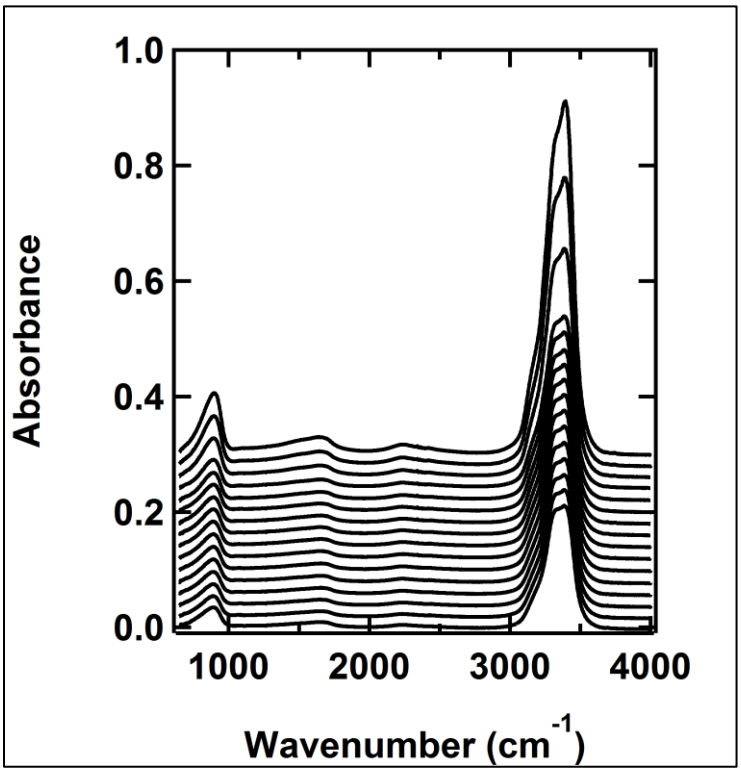

Raw data files: 111314A.IR01 – 16. *Raw RAIR spectra of 60-layer ASW H_2O film before and after 11-, 20-, 30-, 40-, 50-, 60-, 70-, 80-, 90-, 100-, 110-, 120-, 130-, 140-, and 150-minute exposures to 3.4 eV CO_2 beam (4.1 x 10^{15} cm^{-2} s^{-1} flux), whose O=C=O modes at 2341 cm^{-1} and H_2O bands near 3300 cm^{-1} were integrated and serve as the data in* **Figure 4-4(b)**. *These data are also curve* **(c)** *in* **Figure 4-5**. *Data are offset for clarity.*

Figure A4-6

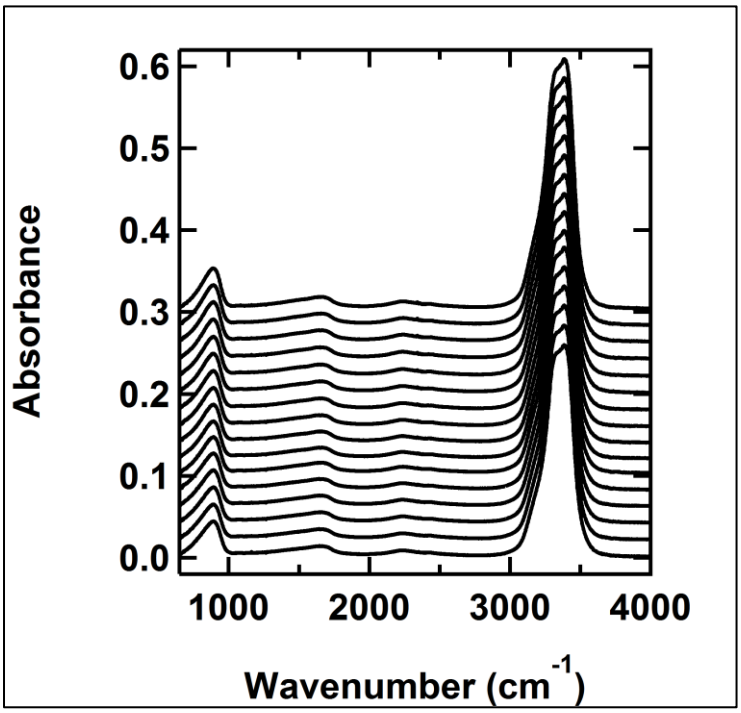

Raw data files: 111114A.IR01 – 16. *Raw RAIR spectra of 74-layer ASW H_2O film before and after 5-, 10-, 15-, 20-, 25-, 30-, 36-, 40-, 45-, 50-, 55-, 60-, 65-, 70-, and 75-minute exposures to 3.7 eV CO_2 beam (5 x 10^{15} cm^{-2} s^{-1} flux), whose O=C=O modes at 2341 cm^{-1} were integrated and serve as the data in curve* **(b)** *in* **Figure 4-5**. *Data are offset for clarity.*

Figure A4-7

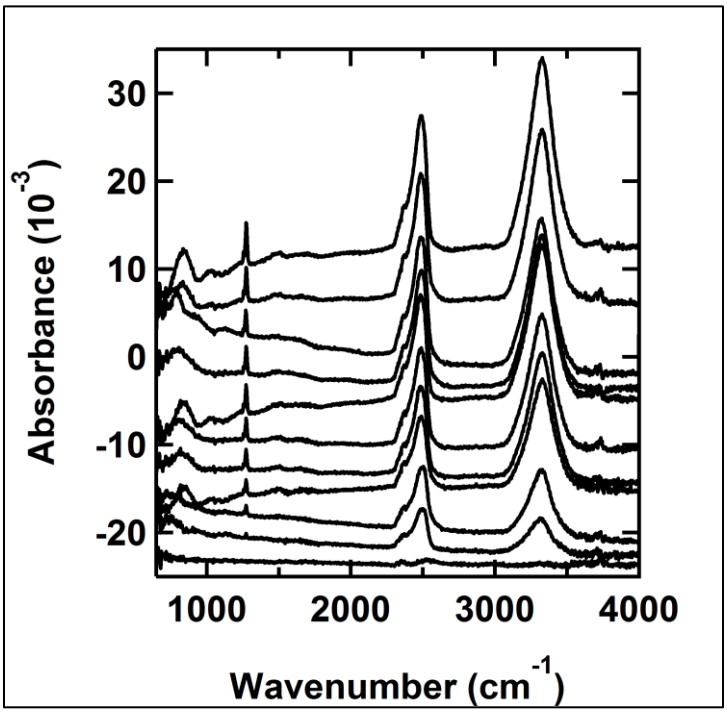

Raw data files: 060314B.IR01 – 11. *Raw RAIR spectra of 60-layer ASW D_2O film before and after 0.5-, 1.1-, 1.5-, 2-, 2.5-, 3-, 3.5-, 4-, 4.5-, and 5-hour exposures to 3.7 eV CF_4 beam (2.8 x 10^{13} cm^{-2} s^{-1} flux), whose C-F modes were integrated and serve as the data in curve* **(b)** *in* **Figure 4-6**. *Data are offset for clarity.*

Figure A4-8

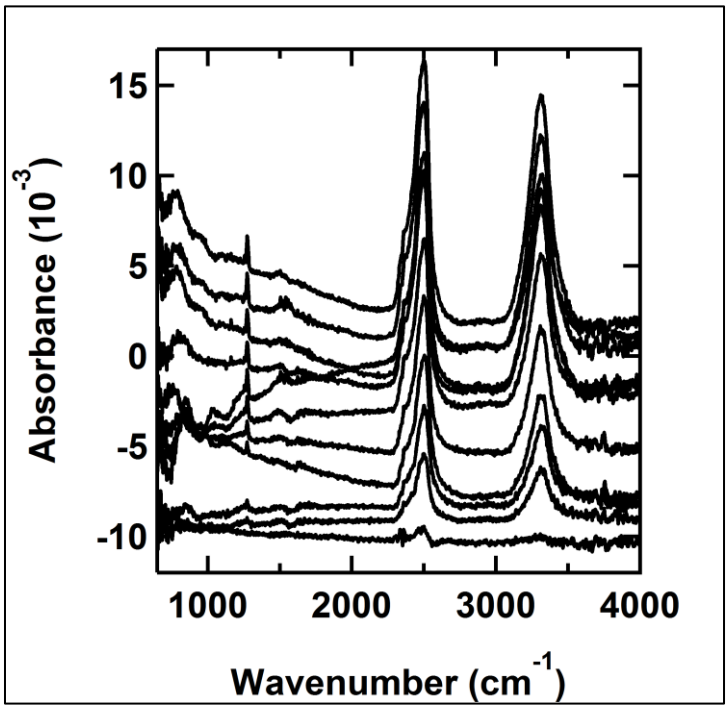

Raw data files: 060214B.IR01 – 11. *Raw RAIR spectra of 60-layer ASW D_2O film before and after 0.5-, 1-, 1.5-, 2-, 2.5-, 3-, 3.5-, 4.1-, 4.5-, and 5.1-hour exposures to 4.1 eV CF_4 beam (4.0 x 10^{13} cm^{-2} s^{-1} flux), whose C-F modes were integrated and serve as the data in curve* **(c)** *in* **Figure 4-6**. *Data are offset for clarity.*

Figure A4-9

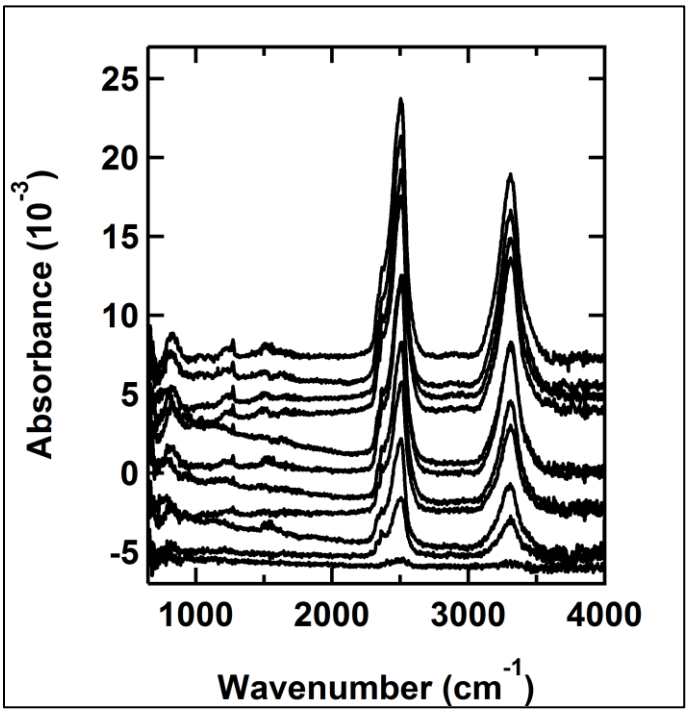

Raw data files: 060414B.IR01 – 11. *Raw RAIR spectra of 60-layer ASW D_2O film before and after 0.5-, 1-, 1.5-, 2-, 2.5-, 3.25-, 3.5-, 4-, 4.5-, and 5-hour exposures to 3.7 eV CF_4 beam (2.8 x 10^{13} cm^{-2} s^{-1} flux), whose C-F modes were integrated and serve as the data in curve* **(d)** *in* **Figure 4-6**. *Data are offset for clarity.*

Figure A4-10

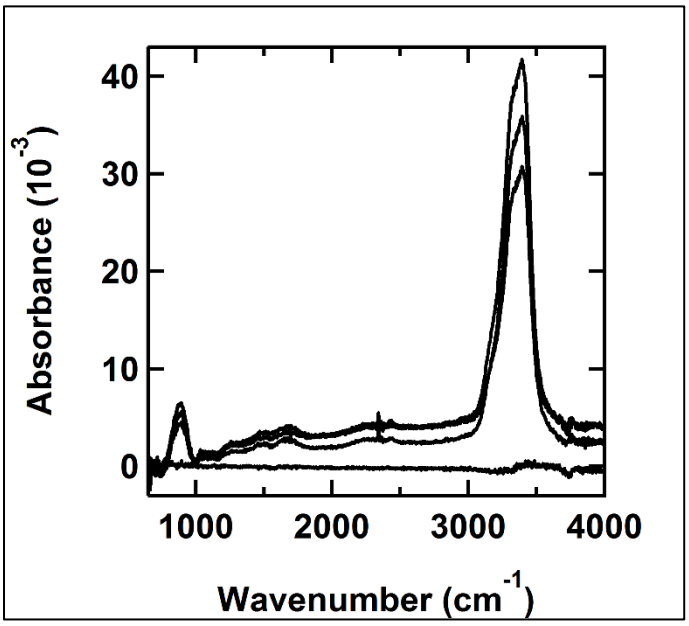

Raw data files: 081314B.IR01 – 04. *Raw RAIR spectra of 60-layer ASW H_2O film before and after 30-, 60-, and 90-minute exposures to 3.0 eV CO_2 beam (5.0 x 10^{15} cm^{-2} s^{-1} flux). The O=C=O modes at 2341 cm^{-1}, once integrated and the integrated intensity fit to a line, account for the 3.0 eV data point in* **Figure 4-7**.

Figure A4-11

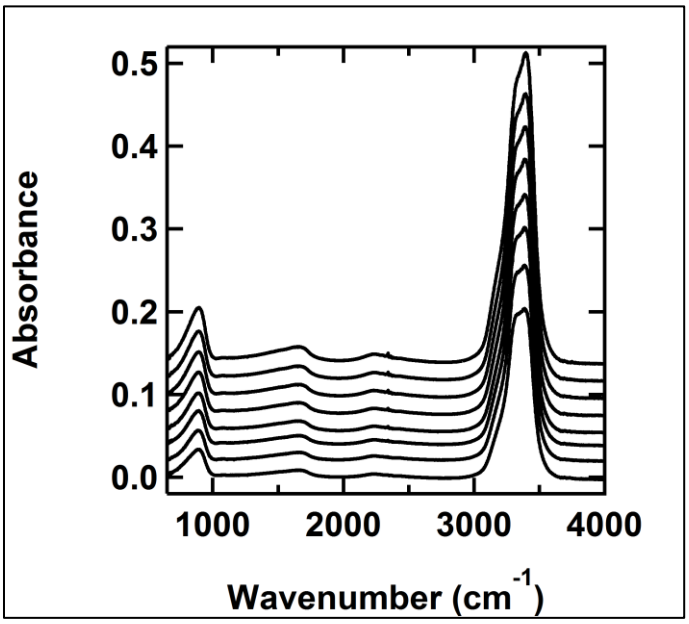

Raw data files: 100214A.IR01 – 08. *Raw RAIR spectra of 60-layer ASW H_2O film before and after 5-, 10-, 15-, 20-, 25-, 30-, and 40-minute exposures to 3.7 eV CO_2 beam (3.0 x 10^{15} cm^{-2} s^{-1} flux). The O=C=O modes at 2341 cm^{-1}, once integrated and the integrated intensity fit to a line, account for the 3.7 eV data point in* **Figure 4-7** *whose data is not already given in* **Figure A4-7**. *Data are offset for clarity.*

Figure A4-12

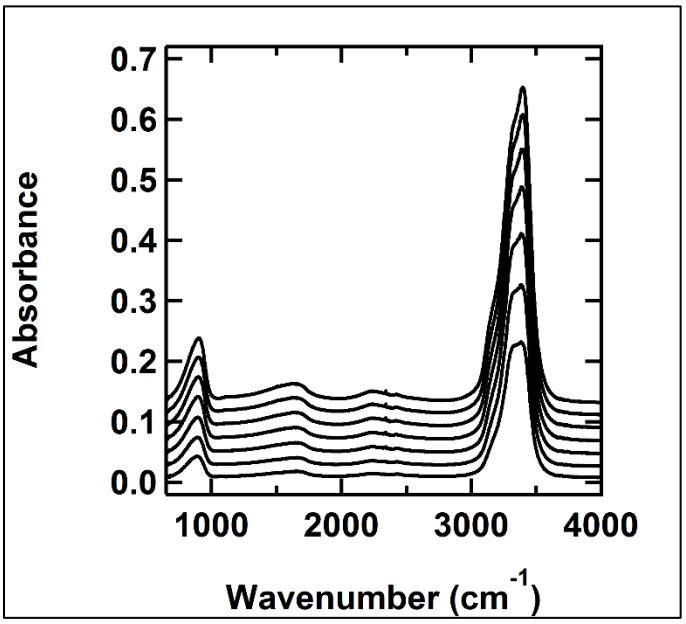

Raw data files: 093014A.IR01 – 07. *Raw RAIR spectra of 60-layer ASW H_2O film before and after 10-, 20-, 30-, 40-, 50-, and 60-minute exposures to 4.0 eV CO_2 beam (1.3 x 10^{16} cm^{-2} s^{-1} flux). The O=C=O modes at 2341 cm^{-1}, once integrated and the integrated intensity fit to a line, account for the 4.0 eV data point in* **Figure 4-7**. *Data are offset for clarity.*

Figure A4-13

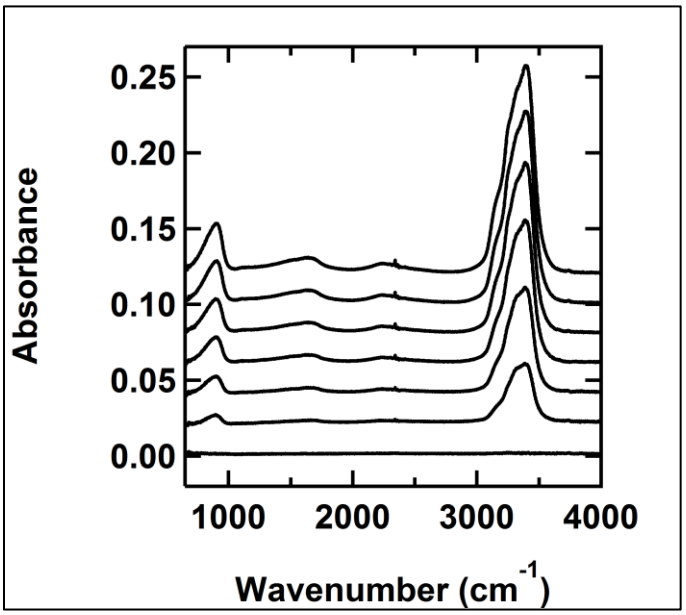

Raw data files: 090814B.IR01 – 07. *Raw RAIR spectra of 60-layer ASW H_2O film before and after 15-, 30-, 45-, 60-, 75-, and 90-minute exposures to 4.2 eV CO_2 beam (1.2 x 10^{16} cm^{-2} s^{-1} flux). The O=C=O modes at 2341 cm^{-1}, once integrated and the integrated intensity fit to a line, account for the 4.2 eV data point in* **Figure 4-7**. *Data are offset for clarity.*

Figure A5-1

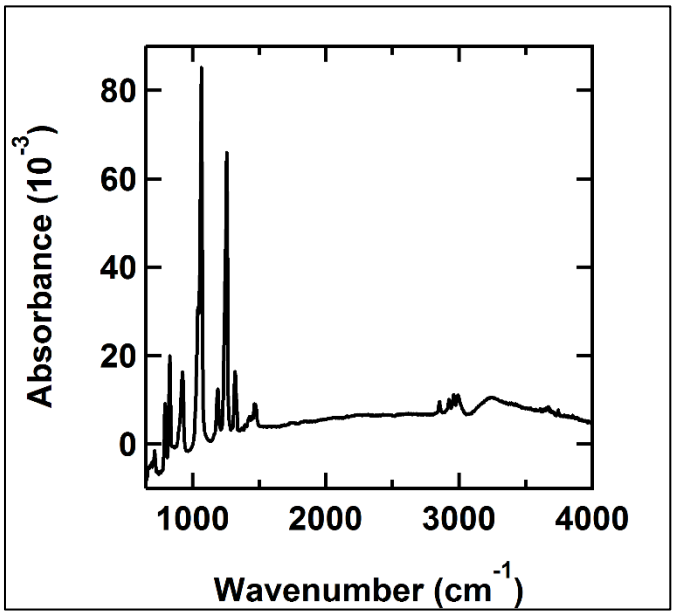

Raw data file: 082015A.IR01. *Raw RAIR spectrum of 40-layer DMMP, corrected for baseline and used in* **Figure 5-1**.

Figure A5-2

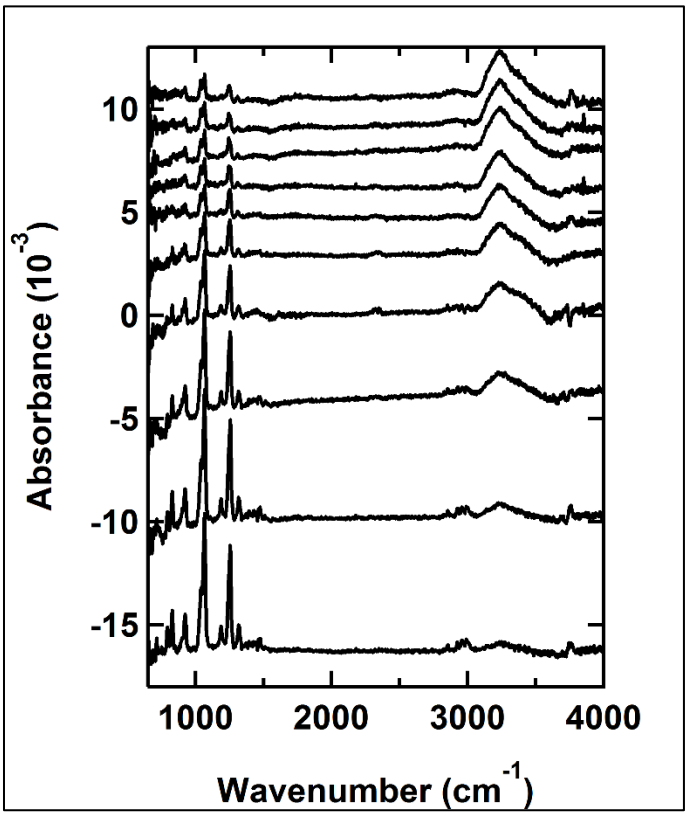

Raw data files: 042815B.IR01 – 10. *Raw RAIR spectra of 4-layer DMMP desorbing at 163 K, the P-O-C modes at 1041 and 1067 cm^{-1} integrated and used in the 163 K panel of* **Figure 5-2**. *Data are offset for clarity.*

Figure A5-3

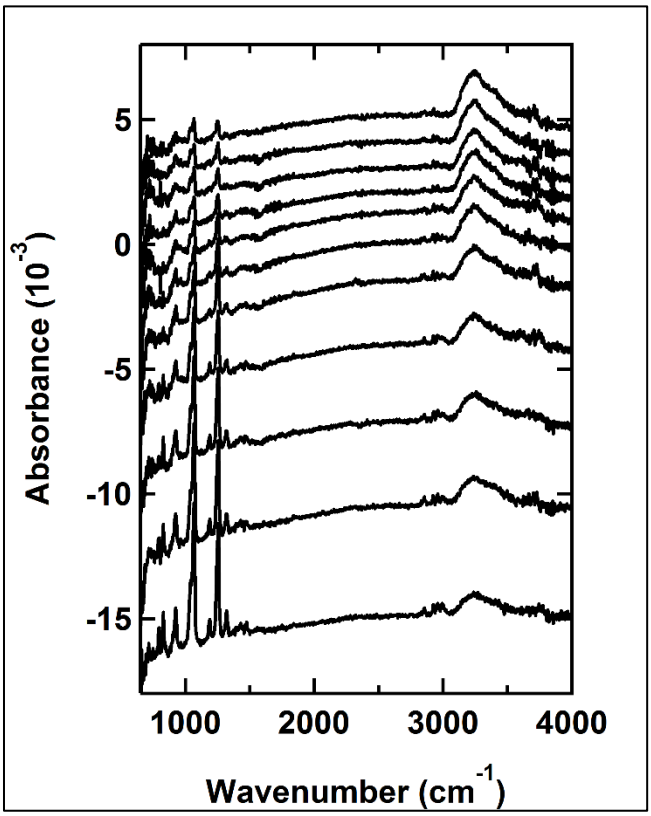

Raw data files: 043015B.IR01 – 11. *Raw RAIR spectra of 4-layer DMMP desorbing at 164 K, the P-O-C modes at 1041 and 1067 cm^{-1} integrated and used in the 164 K panel of* **Figure 5-2**. *Data are offset for clarity.*

Figure A5-4

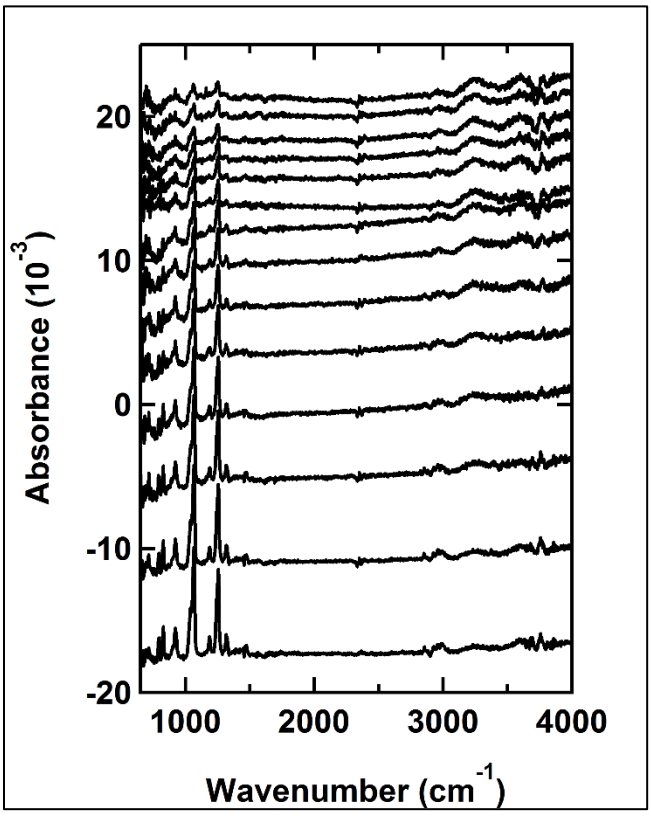

Raw data files: 050415A.IR01 – 15. *Raw RAIR spectra of 4-layer DMMP desorbing at 165 K, the P-O-C modes at 1041 and 1067 cm^{-1} integrated and used in the 165 K panel of* **Figure 5-2**. *Data are offset for clarity.*

Figure A5-5

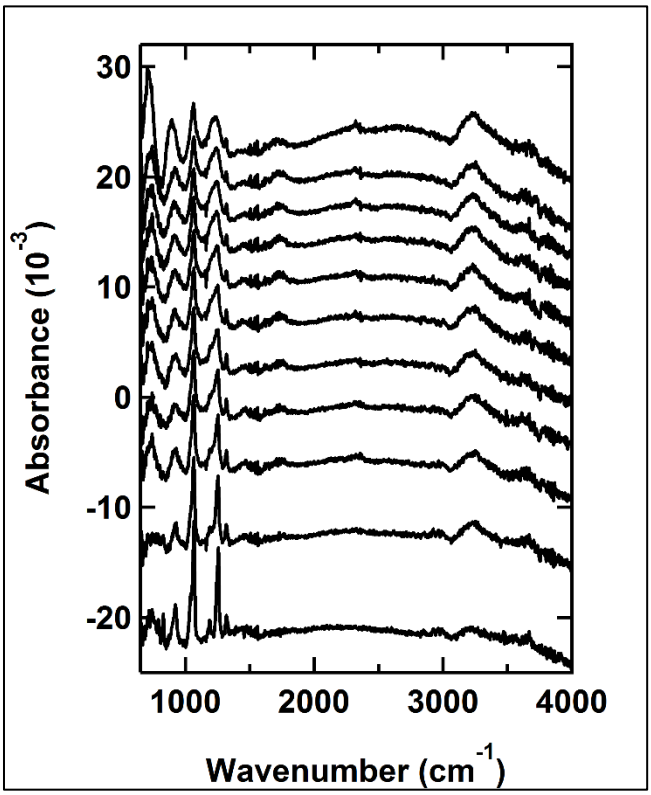

Raw data files: 082815A.IR01 – 10. *Raw RAIR spectra of 6-layer DMMP before and after 15-, 30-, 45-, 60-, 75-, 90-, 106-, 120-, and 135-minute exposures to 0.12 eV O(^{3}P) (2.9x10^{16} cm^{-2} s^{-1} flux), whose P-O-C modes at 1041 and 1067 cm^{-1} were integrated and used in* **Figure 5-3**. *The P=O modes near 1250 cm^{-1} are referenced in* **Figure 5-3(b)** *and* **Figure 5-4**. *The 106-minute exposure spectrum (third from top) is referenced as the black trace in* **Figure 5-5**. *Finally, these data are used in the "6 layer" curves in* **Figure 5-10**. *Data are offset for clarity.*

Figure A5-6

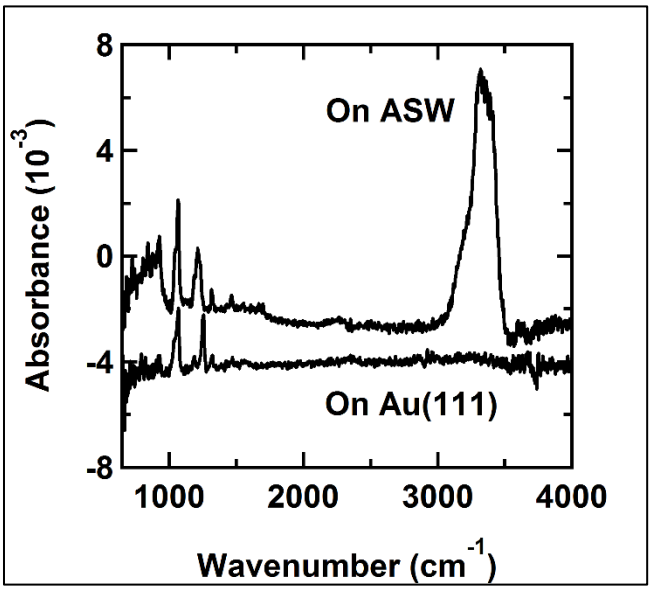

Raw data files: 061115D.IR01, 061215B.IR02. *Raw RAIR spectra of DMMP monolayers on ASW H_2O ice and clean Au(111), shown in* **Figure 5-5**. *Data are offset for clarity.*

Figure A5-7

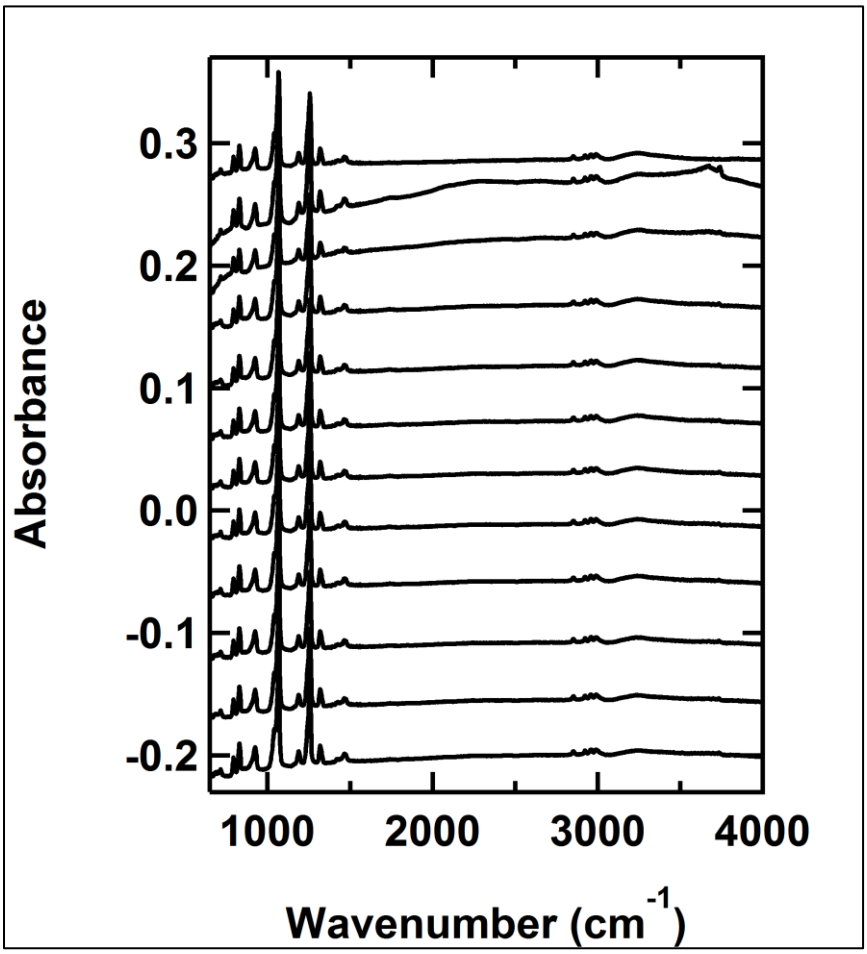

Raw data files: 082015B.IR02 – 12. *Raw RAIR spectra of 39-layer DMMP during exposure to 0.12 eV $O(^3P)$ used in the large data set shown in* **Figure 5-6**. *Data are offset for clarity.*

Figure A5-8

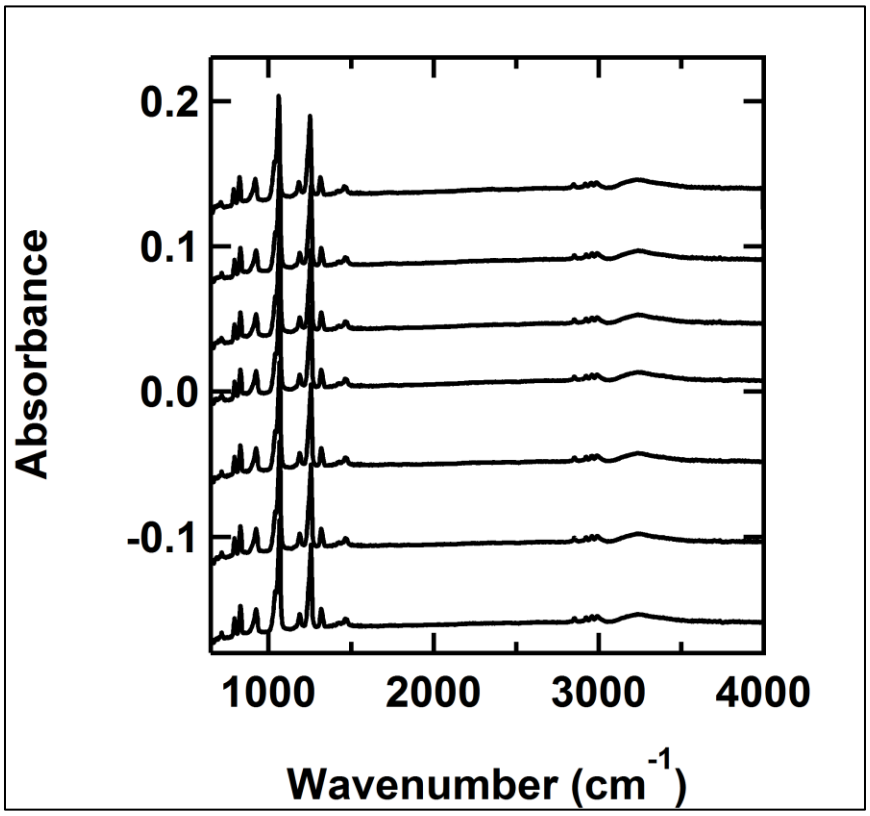

Raw data files: 082015B.IR13 – 19. *Raw RAIR spectra of 34-layer DMMP during exposure to 0.12 eV* $O(^3P)$ *used in the large data set shown in* **Figure 5-6**. *Data are offset for clarity.*

Figure A5-9

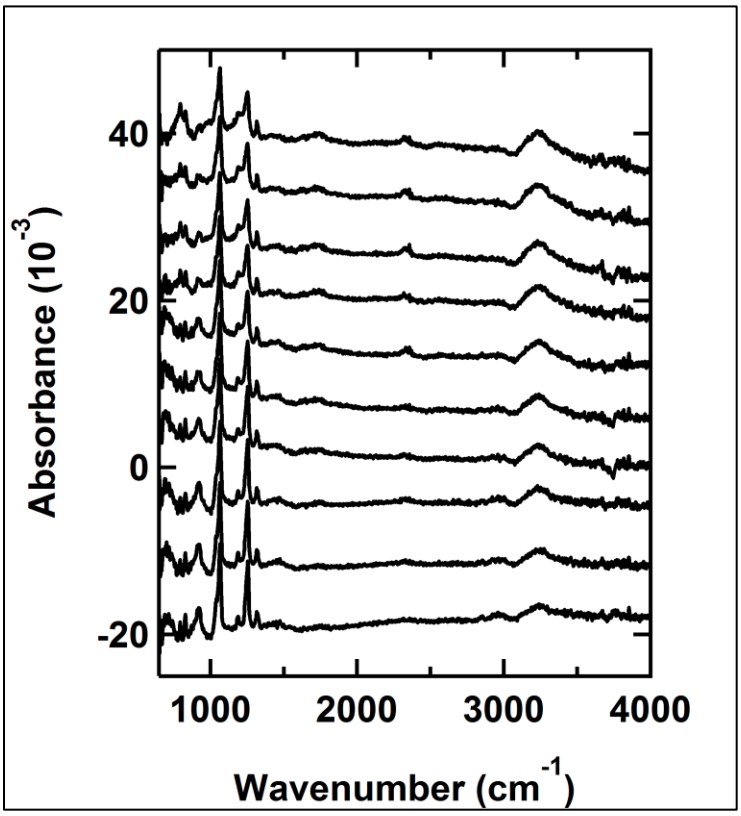

Raw data files: 083115A.IR02 – 11. *Raw RAIR spectra of 6-layer DMMP during exposure to 0.12 eV O(^{3}P) used in the large data set shown in* **Figure 5-6**. *Data are offset for clarity.*

Figure A5-10

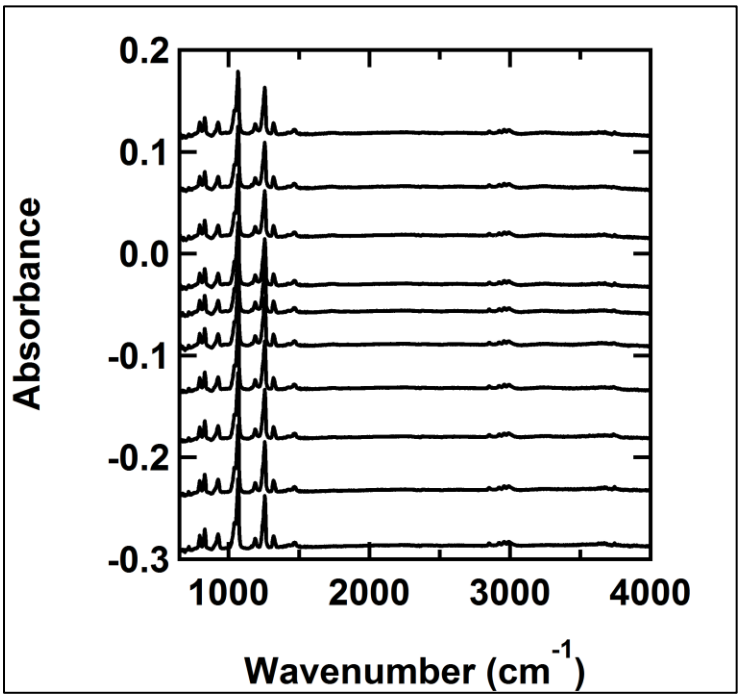

Raw data files: 091115A.IR01 – 10. *Raw RAIR spectra of 36-layer DMMP during exposure to 0.12 eV* $O(^3P)$ *used in the large data set shown in* **Figure 5-6**. *These data are also used in the "36 layer" curves in* **Figure 5-10**. *Data are offset for clarity.*

Figure A5-11

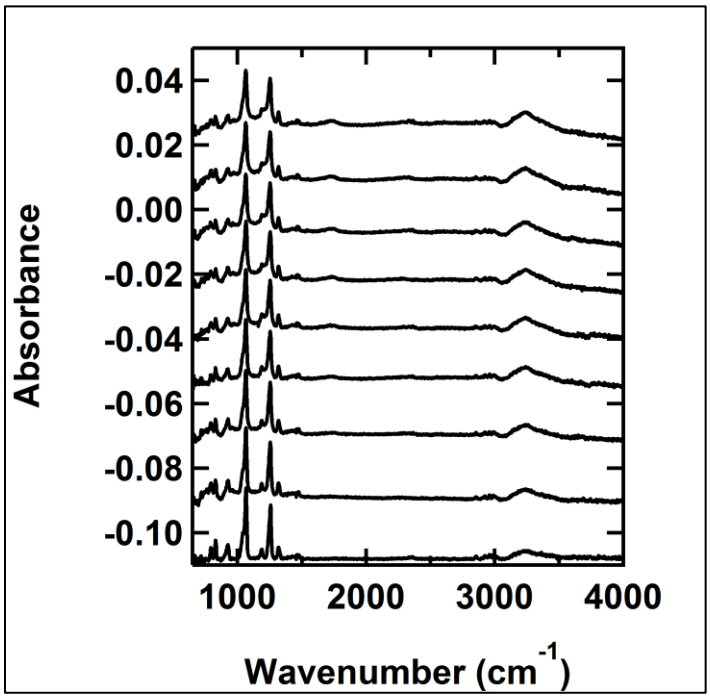

Raw data files: 111315A.IR01 – 10. *Raw RAIR spectra of 12-layer DMMP during exposure to 0.12 eV O(^{3}P) used in the large data set shown in* **Figure 5-6**. *These data are also used in the "12 layer" curves in* **Figure 5-10** *and the last spectrum (top) is used as the DMMP spectrum in* **Figure 6-9**. *Data are offset for clarity.*

Figure A5-12

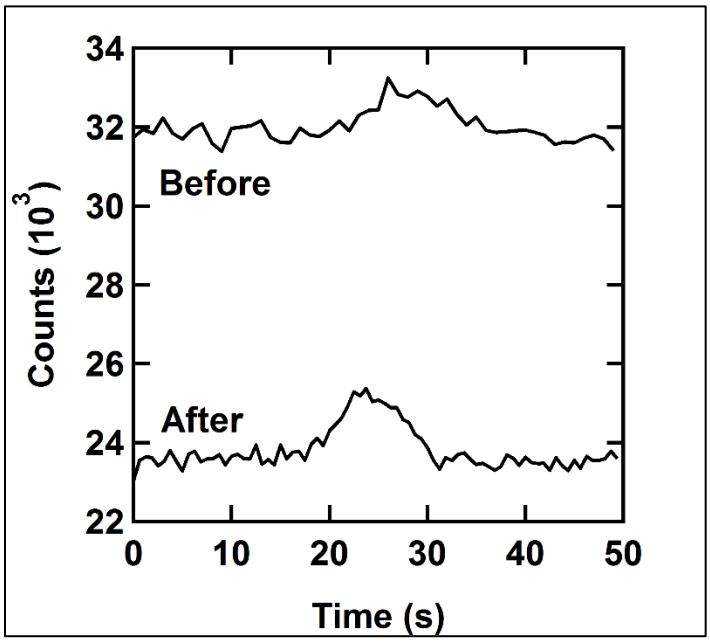

Raw data files: 090215.X01, 100115.X02. *Raw C(1s) XPS signals of 15-layer DMMP film before and after exposure to O(^{3}P), shown in* **Figure 5-7**.

Figure A5-13

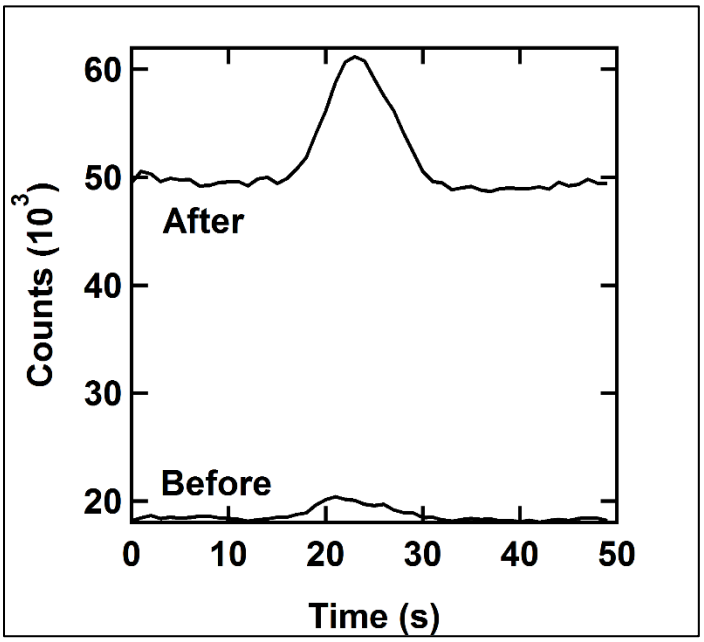

Raw data files: 090215.X02, 100115.X01. *Raw O(1s) XPS signals of 15-layer DMMP film before and after exposure to O(^{3}P), shown in* **Figure 5-7**.

Figure A5-14

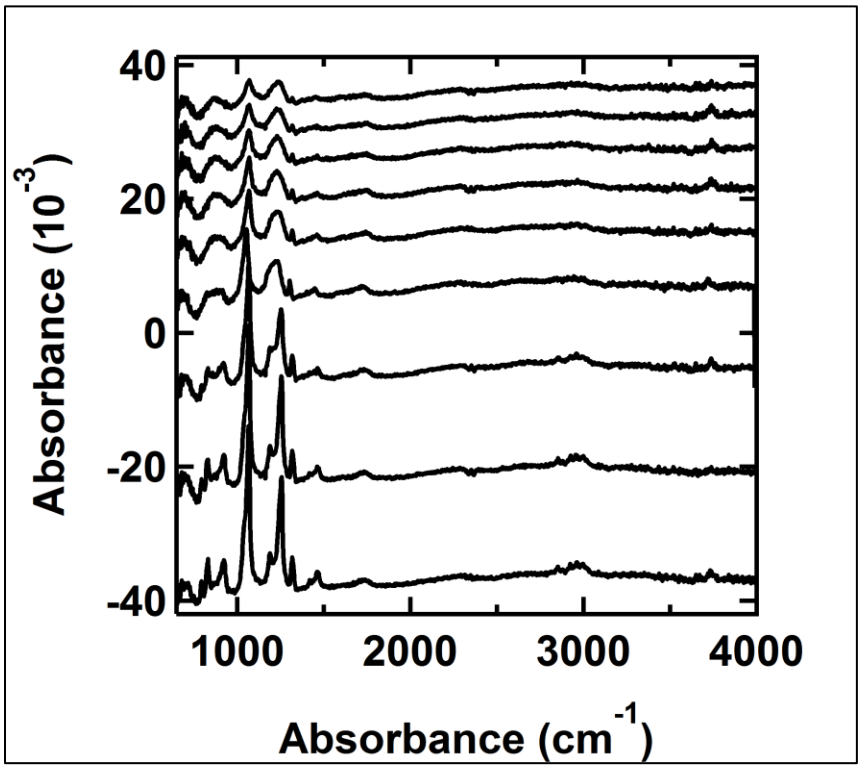

Raw data files: 111615B.IR01 – 09. *Raw RAIR spectra of O(^{3}P)-exposed 15-layer DMMP film during temperature ramp, shown as the "Exposed to O(^{3}P)" data and plots in* **Figure 5-8**. *The P=O regions of the 185 K and 195 K spectra (third and fourth from the bottom, respectively) are also shown in* **Figure 5-9**.

Figure A5-15

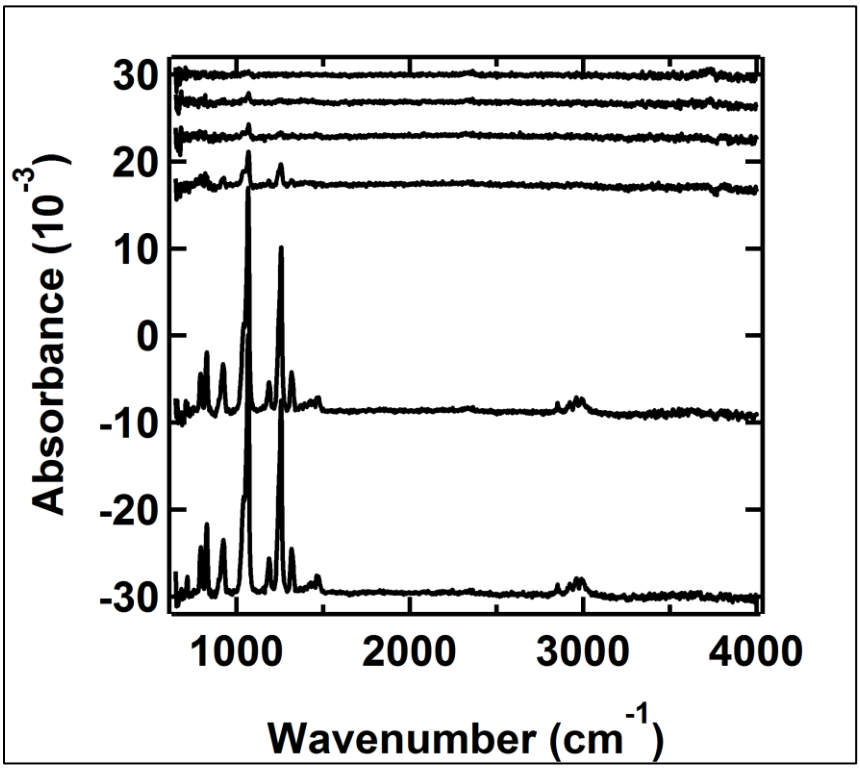

Raw data files: 11115A.IR02 – 07. *Raw RAIR spectra of 15-layer DMMP film during temperature ramp, shown as the "As Deposited" data and plots in* **Figure 5-8**.

Figure A6-1

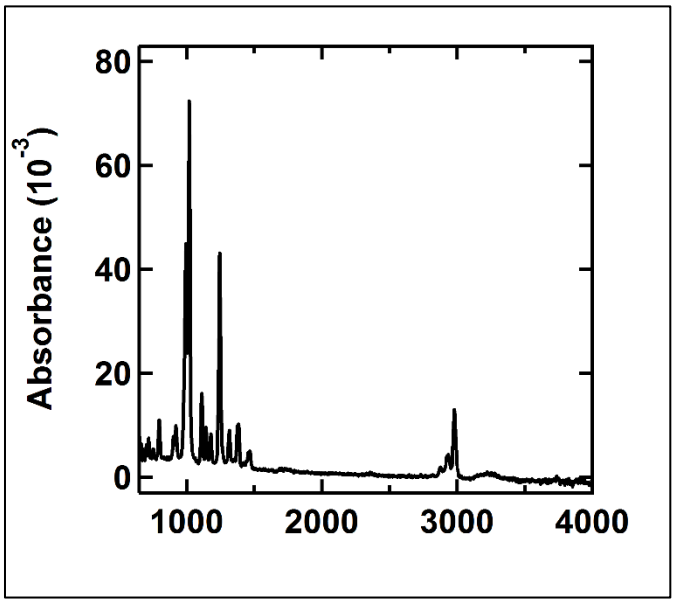

Raw data file: 072716A.IR01. *Raw RAIR spectrum of 27-layer DIMP, corrected for baseline and used in* **Figure 6-1**.

Figure A6-2

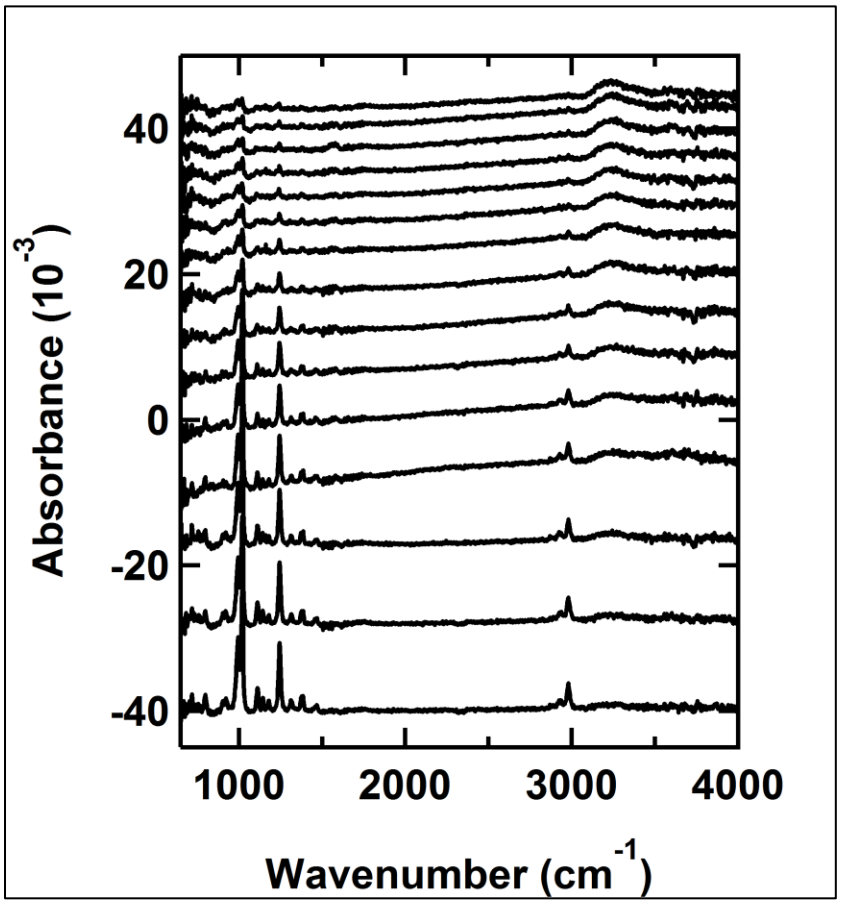

Raw data files: 070616A.IR02 – 16. *Raw RAIR spectra of 6-layer DIMP desorbing at 174 K, whose P-O-C modes at 995 and 1020 cm^{-1} were integrated and used in* **Figure 6-2**. *Data are offset for clarity.*

Figure A6-3

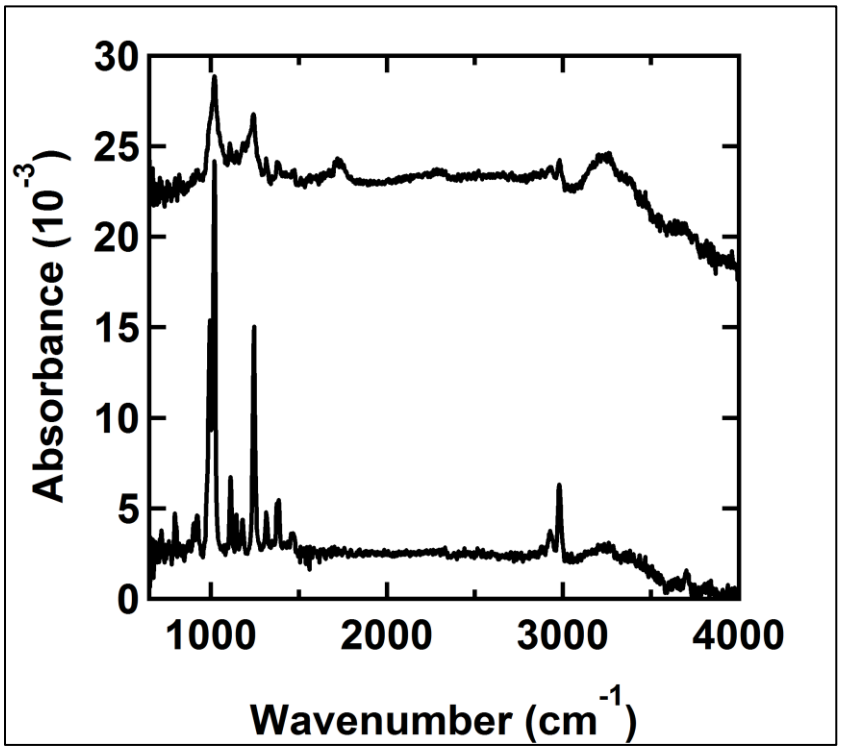

Raw data files: 102716A.IR01, 102716A.IR03. *Raw RAIR spectra of 7-layer DIMP film before and after exposure to 1 x 10^{21} cm^{-2} 0.12 eV $O(^3P)$, shown in* **Figure 6-3**. *Data are offset for clarity.*

Figure A6-4

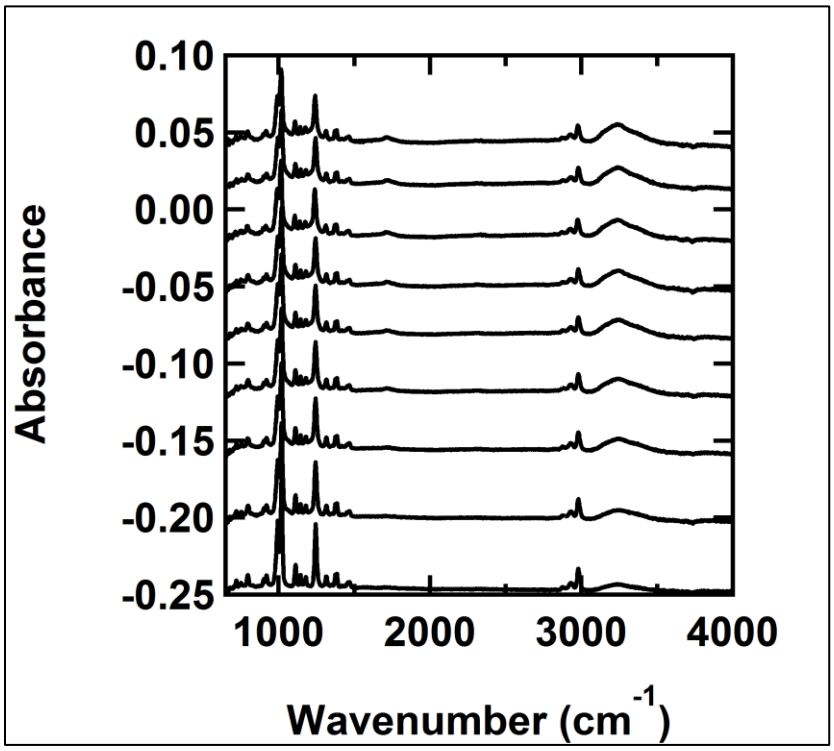

Raw data files: 112916A.IR01 – 09. *Raw RAIR spectra of 27-layer DIMP film before and after 31-, 75-, 120-, 165-, 216-, 270-, 315-, and 360-minute exposures to 0.12 eV O(^{3}P) (1.1 x 10^{17} cm^{-2} s^{-1} flux), shown in* **Figure 6-4**. *These data also comprise the "27 layer" curve of* **Figure 6-8**. *Data are offset for clarity.*

Figure A6-5

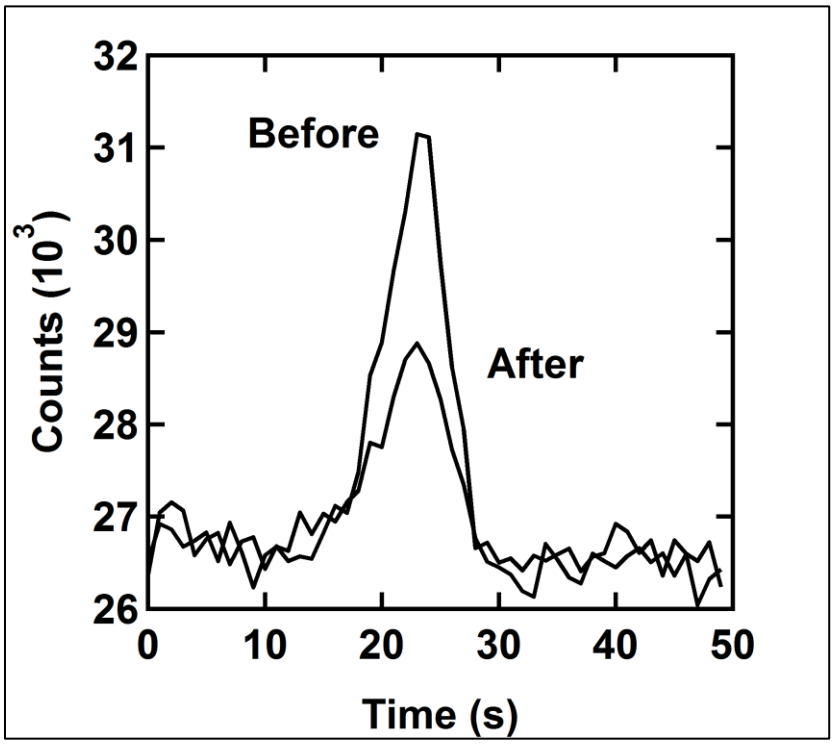

Raw data files: 102616.X01, 102716.X01. *Raw C(1s) XPS signal of pristine 10-layer DIMP film and 6-layer DIMP film exposed to O(^{3}P), shown in* **Figure 6-5**.

Figure A6-6

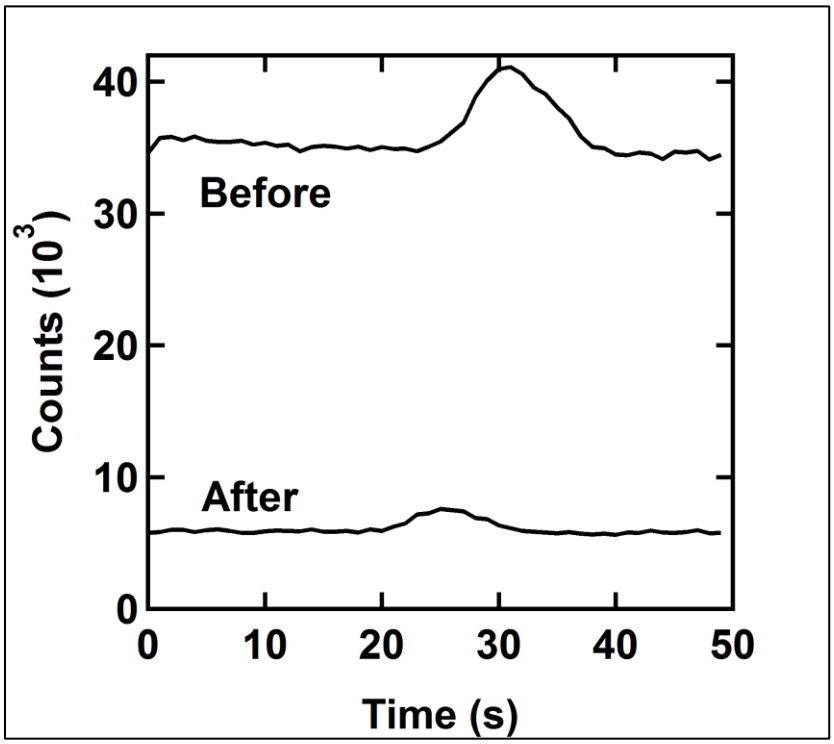

Raw data files: 102616.X02, 102716.X02. *Raw O(1s) XPS signal of pristine 10-layer DIMP film and 6-layer DIMP film exposed to O(^{3}P), shown in* **Figure 6-5**.

Figure A6-7

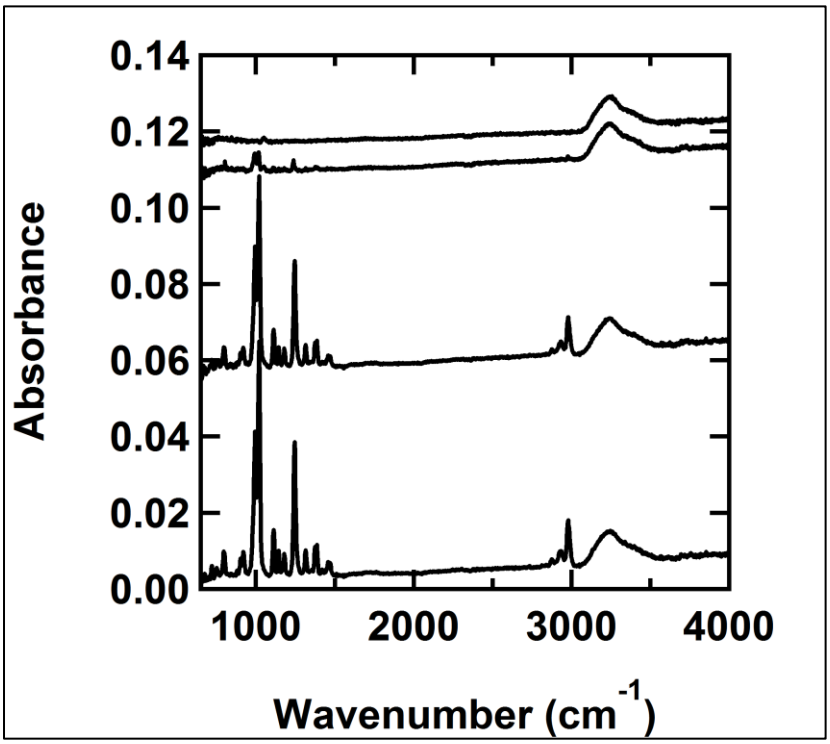

Raw data files: 120716A.IR05 – 08. *Raw RAIR spectra of DIMP film during temperature ramp, shown as the "As Deposited" data and plots in* **Figure 6-7**.

Figure A6-8

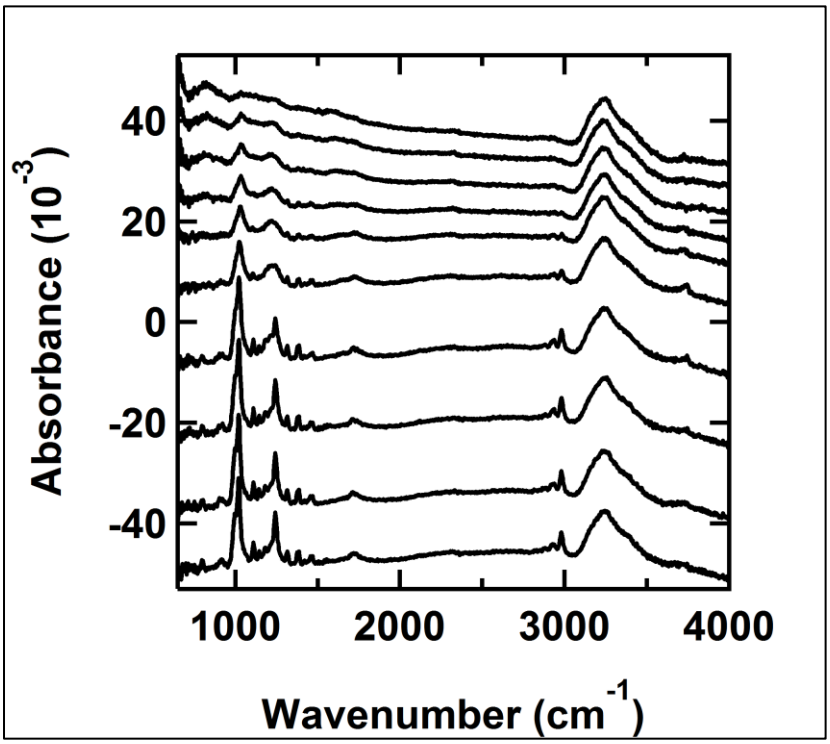

Raw data files: 120916A.IR06 – 15. *Raw RAIR spectra of O(^{3}P)-exposed DIMP film during temperature ramp, shown as the "Exposed to O(^{3}P)" data and plots in* **Figure 6-7**.

Figure A6-9

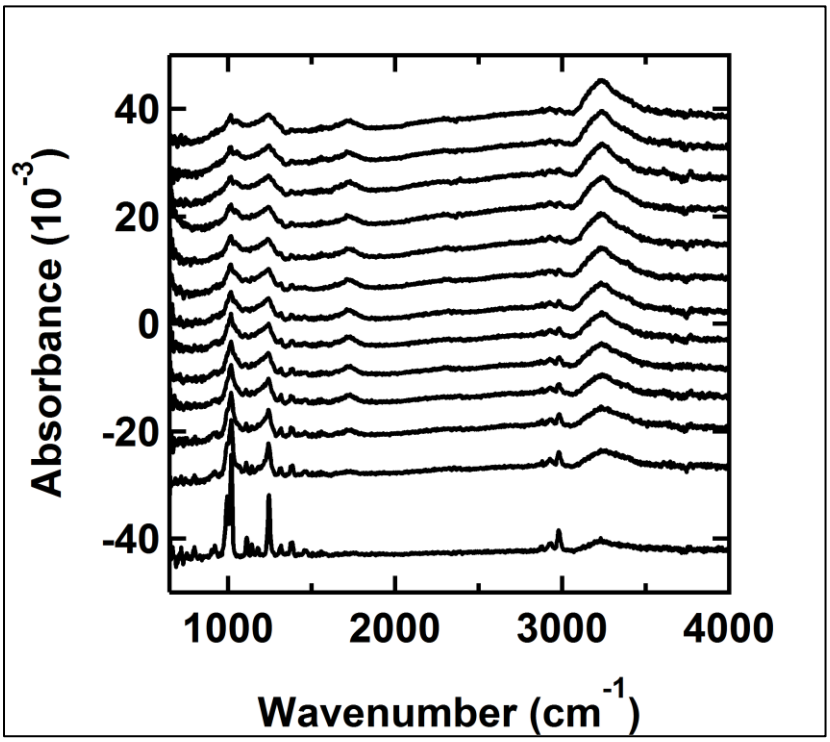

Raw data files: 112116A.IR01 – 13. *Raw RAIR spectra of 7-layer DIMP film before and after 40-, 80-, 121-, 160-, 200-, 240-, 280-, 320-, 360-, 400-, 441-, and 470-minute exposures to 0.12 eV O(^{3}P) (1.1 x 10^{17} cm^{-2} s^{-1} flux), shown in* **Figure 6-8**. *Data are offset for clarity.*

Figure A6-10

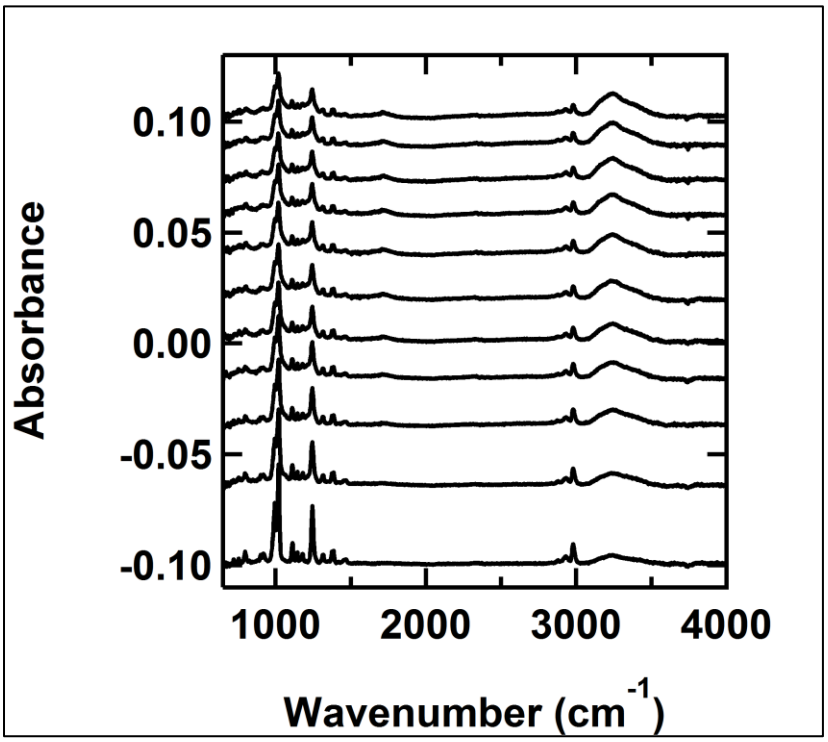

Raw data files: 112816A.IR01 – 11. *Raw RAIR spectra of 17-layer DIMP film before and after 40-, 80-, 120-, 160-, 200-, 241-, 280-, 320-, 361-, and 400-minute exposures to 0.12 eV O(^{3}P) (1.3 x 10^{17} cm^{-2} s^{-1} flux), shown in* **Figure 6-8**. *Two of these spectra also appear as "DIMP" in* **Figure 6-9**. *Data are offset for clarity.*

Figure A6-11

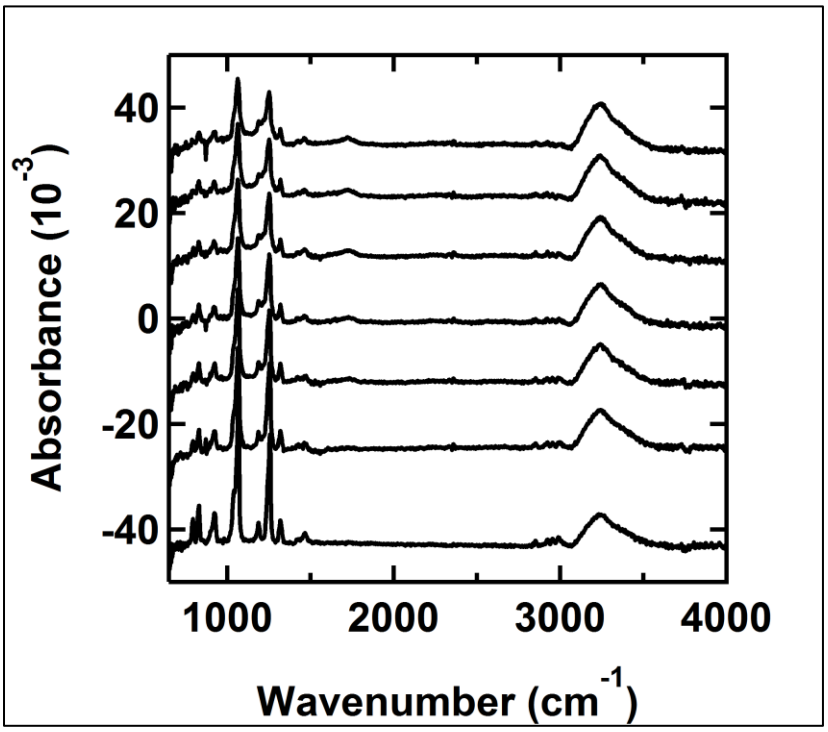

Raw data files: 122116A.IR01 – 07. *Raw RAIR spectra of 12-layer DMMP film before and after 20-, 35-, 50-, 65-, 83-, and 100-minute exposures to 0.12 eV O(^{3}P) (2.1 x 10^{17} cm^{-2} s^{-1} flux), shown in* **Figure 6-10**. *Data are offset for clarity.*

References

(1) Vickerman, J. C.; Gilmore, I. S. *Surface Analysis: The Principle Techniques*, 2nd ed.; Wiley: Chichester, U.K., 2009.

(2) Greenler, R. G. Infrared Study of Adsorbed Molecules on Metal Surfaces by Reflection Techniques. *J. Chem. Phys.* **1966**, *44*, 310–315.

(3) Greenler, R. G. Reflection Method for Obtaining the Infrared Spectrum of a Thin Layer on a Metal Surface. *J. Chem. Phys.* **1969**, *50*, 1963–1968.

(4) Briggs, D.; Seah, M. P. *Practical Surface Analysis by Auger and X-Ray Photoelectron Spectroscopy*, 2nd ed.; Wiley: Chichester, U.K., 1983.

(5) Crist, V. B. Handbooks of Monochromatic XPS Spectra Volume 1 - The Elements and Native Oxides. *Handb. Elem. Nativ. Oxides* **1999**, *1*, 1–43.

(6) Sibener, S. J.; Buss, R. J.; Cheuk Yiu Ng; Yuan, T. L. Development of a Supersonic $O(^3P_J)$, $O(^1D_2)$ Atomic Oxygen Nozzle Beam Source. *Rev. Sci. Instrum.* **1980**, *51*, 167–182.

(7) Alagia, M.; Aquilanti, V.; Ascenzi, D.; Balucani, N.; Cappelletti, D.; Cartechini, L.; Casavecchia, P.; Pirani, F.; Sanchini, G.; Volpi, G. G. Magnetic Analysis of Supersonic Beams of Atomic Oxygen, Nitrogen, and Chlorine Generated from a Radio-Frequency Discharge. *Isr. J. Chem.* **1997**, *37*, 329–342.

(8) Casavecchia, P.; Balucani, N.; Volpi, G. G. Reactive Scattering of $O(^3P, ^1D)$, $Cl(^2P)$ and OH Radicals. In *The Chemical Dynamics and Kinetics of Small Radicals*; Wagner, A., Liu, K., Eds.; World Scientific Publishing Company, 1996; pp 365–426.

(9) Aquilanti, V.; Ascenzi, D.; Cappelletti, D.; Pirani, F. Magnetic Analysis of Nearly Effusive and Moderately Supersonic Beams of Oxygen Molecules. *Int. J. Mass Spectrom. Ion Process.* **1995**, *149*, 355–371.

(10) Li, W.; Langlois, G. G.; Kautz, N. A.; Sibener, S. J. Formation of Stabilized Ketene Intermediates in the Reaction of $O(^3P)$ with Oligo(phenylene ethynylene) Thiolate Self-Assembled Monolayers on Au(111). *J. Phys. Chem. C* **2014**, *118*, 15846–15852.

(11) Polanyi, J. C. Some Concepts in Reaction Dynamics. *Acc. Chem. Res.* **1972**, *5*, 161–168.

(12) Bernstein, R. B. *Chemical Dynamics via Molecular Beam and Laser Techniques*; Oxford University Press: Oxford New York, 1982.

(13) Levine, R. D.; Bernstein, R. B. *Molecular Reaction Dynamics and Chemical Reactivity*; Oxford University Press: Oxford New York, 1987.

(14) Moore, C.; Smith, I. Vibrational–Rotational Excitation. Chemical Reactions of Vibrationally Excited Molecules. *Faraday Discuss. Chem. Soc.* **1979**, *67*, 146–161.

(15) Orr-Ewing, A. J. Dynamical Stereochemistry of Bimolecular Reactions. *J. Chem. Soc. Trans.* **1996**, *92*, 881–900.

(16) Parker, D. H.; Bernstein, R. B. Oriented Molecule Bems via the Electrostatic Hexapole: Preparation, Characterization, and Reactive Scattering. *Annu. Rev. Phys. Chem.* **1989**, *40*, 561–595.

(17) Loesch, H. J. Orientation and Alignment in Reactive Beam Collisions: Recent Progress. *Annu. Rev. Phys. Chem.* **1995**, *46*, 555–594.

(18) Love, J. C.; Estroff, L. A.; Kriebel, J. K.; Nuzzo, R. G.; Whitesides, G. M. Self-Assembled Monolayers of Thiolates on Metals as a Form of Nanotechnology. *Chem. Rev.* **2005**, *105*, 1103–1169.

(19) Ulman, A. Formation and Structure of Self-Assembled Monolayers. *Chem. Rev.* **1996**, *96*, 1533–1554.

(20) Schreiber, F. Structure and Growth of Self-Assembling Monolayers. *Prog. Surf. Sci.* **2000**, *65*, 151–256.

(21) Gibson, K. D.; Isa, N.; Sibener, S. J. Experiments and Simulations of Ar Scattering from an Ordered 1-Decanethiol-Au(111) Monolayer. *J. Chem. Phys.* **2003**, *119*, 13083–13095.

(22) Isa, N.; Gibson, K. D.; Yan, T.; Hase, W.; Sibener, S. J. Experimental and Simulation Study of Neon Collision Dynamics with a 1-Decanethiol Monolayer. *J. Chem. Phys.* **2004**, *120*, 2417–2433.

(23) Lu, J. W.; Day, B. S.; Fiegland, L. R.; Davis, E. D.; Alexander, W. A.; Troya, D.; Morris, J. R. Interfacial Energy Exchange and Reaction Dynamics in Collisions of Gases on Model Organic Surfaces. *Prog. Surf. Sci.* **2012**, *87*, 221–252.

(24) Sloane, T. M.; Brudzynski, R. J. Competition between Reactive Sites in the Reactions of Oxygen-Atoms and Hydroxyl Radicals with Phenylacetylene and Styrene. *J. Am. Chem. Soc.* **1979**, *101*, 1495–1499.

(25) Eichholtz, M.; Kohl, S.; Schneider, A.; Vollmer, J.; Wagner, H. G. The Reactions of O(^{3}P) Atoms with Aromatic Hydrocarbons with Unsaturated Side Chains. *Symp Int Combust Proc* **1996**, *26*, 527–534.

(26) Kanofsky, J. R.; Lucas, D.; Pruss, F.; Gutman, D. Direct Identification of the Reactive Channels in the Reactions of Oxygen Atoms and Hydroxyl Radicals with Acetylene and Methylacetylene. *J. Phys. Chem.* **1974**, *78*, 311–316.

(27) Arrington, C. A.; Cox, D. J. Arrhenius Parameters for the Reaction of Oxygen Atoms, O(3P), with Propyne. *J. Phys. Chem.* **1975**, *79*, 2584–2586.

(28) Schmoltner, A. M.; Chu, P. M.; Lee, Y. T. Crossed Molecular Beam Study of the Reaction O(^{3}P)+C_2H_2. *J. Chem. Phys.* **1989**, *91*, 5365–5373.

(29) Harding, L. B. Theoretical Studies on the Reaction of Atomic Oxygen (3P) with Acetylene. *J. Phys. Chem.* **1981**, *85*, 10–11.

(30) Harding, L. B.; Wagner, A. F. Theoretical Studies on the Reaction of Atomic Oxygen (O(3P)) with Acetylene. *J. Phys. Chem.* **1986**, *90*, 2974–2987.

(31) Xing, G.; Huang, X.; Wang, X.; Bersohn, R. Reactions of O(^{3}P) with Alkynes: The CO

and H Atom Channels. *J. Chem. Phys.* **1996**, *105*, 488–496.

(32) Girard, Y.; Chaquin, P. Addition Reactions of ^{1}D and ^{3}P Atomic Oxygen with Acetylene. Potential Energy Surfaces and Stability of the Primary Products. Is Oxirene Only a Triplet Molecule? A Theoretical Study. *J. Phys. Chem. A* **2003**, *107*, 10462–10470.

(33) Nguyen, T. L.; Vereecken, L.; Peeters, J. Quantum Chemical and Theoretical Kinetics Study of the $O(^{3}P) + C_2H_2$ Reaction: A Multistate Process. *J. Phys. Chem. A* **2006**, *110*, 6696–6706.

(34) Schmoltner, A. M.; Chu, P. M.; Brudzynski, R. J.; Lee, Y. T. Crossed Molecular Beam Study of the Reaction $O(^{3}P)+C_2H_2$. *J. Chem. Phys.* **1989**, *91*, 6926–6936.

(35) Casavecchia, P.; Capozza, G.; Segoloni, E.; Leonori, F.; Balucani, N.; Volpi, G. G. Dynamics of the $O(^{3}P) + C_2H_4$ Reaction: Identification of Five Primary Product Channels (Vinoxy, Acetyl, Methyl, Methylene, and Ketene) and Branching Ratios by the Crossed Molecular Beam Technique with Soft Electron Ionizat. *J. Phys. Chem. A* **2005**, *109*, 3527–3530.

(36) Haller, I.; Pimentel, G. C. Reaction of Oxygen Atoms with Acetylene to Form Ketene. *J. Am. Chem. Soc.* **1962**, *84*, 2855–2857.

(37) Gaedtke, H.; Glänzer, K.; Hippler, H.; Luther, K.; Troe, J. Addition Reactions of Oxygen Atoms at High Pressures. *Symp. Combust.* **1973**, *14*, 295–303.

(38) Tour, J. M.; Jones, L.; Pearson, D. L.; Lamba, J. J. S.; Burgin, T. P.; Whitesides, G. M.; Allara, D. L.; Parikh, A. N.; Atre, S. Self-Assembled Monolayers and Multilayers of Conjugated Thiols, α,ω-Dithiols, and Thioacetyl-Containing Adsorbates. Understanding Attachments between Potential Molecular Wires and Gold Surfaces. *J. Am. Chem. Soc.* **1995**, *117*, 9529–9534.

(39) Dhirani, A.; Zehner, R. W.; Hsung, R. P.; Guyot-Sionnest, P.; Sita, L. R. Self-Assembly of Conjugated Molecular Rods: A High-Resolution STM Study. *J. Am. Chem. Soc.* **1996**, *118*, 3319–3320.

(40) Yang, G.; Qian, Y.; Engtrakul, C.; Sita, L. R.; Liu, G. Y. Arenethiols Form Ordered and Incommensurate Self-Assembled Monolayers on Au(111) Surfaces. *J. Phys. Chem. B* **2000**, *104*, 9059–9062.

(41) Cai, L.; Yao, Y.; Yang, J.; Price, D. W.; Tour, J. M. Chemical and Potential-Assisted Assembly of Thiolacetyl-Terminated Oligo(phenylene ethynylene)s on Gold Surfaces. *Chem. Mater.* **2002**, *14*, 2905–2909.

(42) Béthencourt, M. I.; Srisombat, L. O.; Chinwangso, P.; Lee, T. R. SAMs on Gold Derived from the Direct Adsorption of Alkanethioacetates Are Inferior to Those Derived from the Direct Adsorption of Alkanethiols. *Langmuir* **2009**, *25*, 1265–1271.

(43) Singh, A.; Dahanayaka, D. H.; Biswas, A.; Bumm, L. A.; Halterman, R. L. Molecularly Ordered Decanethiolate Self-Assembled Monolayers on Au(111) from in situ Cleaved Decanethioacetate: An NMR and STM Study of the Efficacy of Reagents for Thioacetate Cleavage. *Langmuir* **2010**, *26*, 13221–13226.

(44) Duan, L.; Garrett, S. J. An Investigation of Rigid P-Methylterphenyl Thiol Self-Assembled Monolayers on Au (111) Using Reflection-Absorption Infrared Spectroscopy and Scanning Tunneling Microscopy. *J. Phys. Chem. B* **2001**, *105*, 9812–9816.

(45) Ulman, A.; Kang, J. F.; Shnidman, Y.; Liao, S.; Jordan, R.; Choi, G. Y.; Zaccaro, J.; Myerson, A. S.; Rafailovich, M.; Sokolov, J.; et al. Self-Assembled Monolayers of Rigid Thiols. *J. Biotechnol.* **2000**, *74*, 175–188.

(46) Dunbar, T. D.; Cygan, M. T.; Bumm, L. A.; McCarty, G. S.; Burgin, T. P.; Reinerth, W. A.; Jones II, L.; Jackiw, J. J.; Tour, J. M.; Weiss, P. S.; et al. Combined Scanning Tunneling Microscopy and Infrared Spectroscopic Characterization of Mixed Surface Assemblies of Linear Conjugated Guest Molecules in Host Alkanethiolate Monolayers on Gold. *J. Phys. Chem. B* **2000**, *104*, 4880–4893.

(47) Kang, J. F.; Ulman, A.; Liao, S.; Jordan, R.; Yang, G.; Liu, G. Y. Self-Assembled Rigid Monolayers of 4′-Substituted-4-Mercaptobiphenyls on Gold and Silver Surfaces. *Langmuir* **2001**, *17*, 95–106.

(48) Matei, D. G.; Muzik, H.; Gölzhäuser, A.; Turchanin, A. Structural Investigation of 1,1'-Biphenyl-4-Thiol Self-Assembled Monolayers on Au(111) by Scanning Tunneling Microscopy and Low-Energy Electron Diffraction. *Langmuir* **2012**, *28*, 13905–13911.

(49) Maksymovych, P.; Yates Jr., J. T. Au Adatoms in Self-Assembly of Benzenethiol on the Au(111) Surface. *J. Am. Chem. Soc.* **2008**, *130*, 7518–7519.

(50) Maksymovych, P.; Voznyy, O.; Dougherty, D. B.; Sorescu, D. C.; Yates Jr., J. T. Gold Adatom as a Key Structural Component in Self-Assembled Monolayers of Organosulfur Molecules on Au(111). *Prog. Surf. Sci.* **2010**, *85*, 206–240.

(51) Kautz, N. A.; Kandel, S. A. Alkanethiol/Au(111) Self-Assembled Monolayers Contain Gold Adatoms: Scanning Tunneling Microscopy before and after Reaction with Atomic Hydrogen. *J. Am. Chem. Soc.* **2008**, *130*, 6908–6909.

(52) Kautz, N. A.; Kandel, S. A. Alkanethiol Monolayers Contain Gold Adatoms, and Adatom Coverage Is Independent of Chain Length. *J. Phys. Chem. C* **2009**, *113*, 19286–19291.

(53) Jobbins, M. M.; Raigoza, A. F.; Kandel, S. A. Adatoms at the Sulfur–Gold Interface in 1-Adamantanethiolate Monolayers, Studied Using Reaction with Hydrogen Atoms and Scanning Tunneling Microscopy. *J. Phys. Chem. C* **2011**, *115*, 25437–25441.

(54) Cerioni, G.; Plumitallo, A.; Frey, J.; Rappoport, Z. Oxygen-17 and Carbon-13 NMR Studies of Diarylketenes. *Magn. Reson. Chem.* **1995**, *33*, 669–673.

(55) Barry, N. J.; Fletcher, W.; Whitehead, J. C. The Dynamics of OH Production in the Reaction $O(^3P)$ + Benzene. *J. Phys. Chem.* **1986**, *90*, 4911–4912.

(56) Lu, J. W.; Fiegland, L. R.; Davis, E. D.; Alexander, W. A.; Wagner, A.; Gandour, R. D.; Morris, J. R. Initial Reaction Probability and Dynamics of Ozone Collisions with a Vinyl-Terminated Self-Assembled Monolayer. *J. Phys. Chem. C* **2011**, *115*, 25343–25350.

(57) Yan, T.; Isa, N.; Gibson, K. D.; Sibener, S. J.; Hase, W. L. Role of Surface Intramolecular Dynamics in the Efficiency of Energy Transfer in Ne Atom Collisions with a *n*-

Hexylthiolate Self-Assembled Monolayer. *J. Phys. Chem. A* **2003**, *107*, 10600–10607.

(58) Tasić, U. S.; Yan, T.; Hase, W. L. Dynamics of Energy Transfer in Collisions of O(3P) Atoms with a 1-Decanethiol Self-Assembled Monolayer Surface. *J. Phys. Chem. B* **2006**, *110*, 11863–11877.

(59) Gibson, K. D.; Langlois, G. G.; Li, W.; Killelea, D. R.; Sibener, S. J. Molecular Interactions with Ice: Molecular Embedding, Adsorption, Detection, and Release. *J. Chem. Phys.* **2014**, *141*, 18C514/1-11.

(60) Langlois, G. G.; Li, W.; Gibson, K. D.; Sibener, S. J. Capture of Hyperthermal CO2 by Amorphous Water Ice via Molecular Embedding. *J. Phys. Chem. A* **2015**, *119*, 12238–12244.

(61) Sill, G. T.; Wilkening, L. L. Ice Clathrate as a Possible Source of the Atmospheres of the Terrestrial Planets. *Icarus* **1978**, *33*, 13–22.

(62) Owen, T.; Bar-Nun, A. Comets, Impacts, and Atmospheres. *Icarus* **1995**, *116*, 215–226.

(63) Dauphas, N. The Dual Origin of the Terrestrial Atmosphere. *Icarus* **2003**, *165*, 326–339.

(64) Owen, T. The Contributions of Comets to Planets, Atmospheres, and Life: Insights from Cassini-Huygens, Galileo, Giotto, and Inner Planet Missions. *Space Sci. Rev.* **2008**, *138*, 301–316.

(65) Notesco, G.; Bar-Nun, A.; Owen, T. Gas Trapping in Water Ice at Very Low Deposition Rates and Implications for Comets. *Icarus* **2003**, *162*, 183–189.

(66) Yokochi, R.; Marboeuf, U.; Quirico, E.; Schmitt, B. Pressure Dependent Trace Gas Trapping in Amorphous Water Ice at 77K: Implications for Determining Conditions of Comet Formation. *Icarus* **2012**, *218*, 760–770.

(67) Burke, D. J.; Brown, W. A. Ice in Space: Surface Science Investigations of the Thermal Desorption of Model Interstellar Ices on Dust Grain Analogue Surfaces. *Phys. Chem. Chem. Phys.* **2010**, *12*, 5947–5969.

(68) Ehrenfreund, P.; Charnley, S. B. Organic Molecules in the Interstellar Medium, Comets, and Meteorites: A Voyage from Dark Clouds to the Early Earth. *Annu. Rev. Astron. Astrophys* **2000**, *38*, 427–483.

(69) Gudipati, M. S.; Allamandola, L. J. Facile Generation and Storage of Polycyclic Aromatic Hydrocarbon Ions in Astrophysical Ices. *Astrophys. J.* **2003**, *596*, L195-198.

(70) Nuevo, M.; Bredehöft, J. H.; Meierhenrich, U. J.; d'Hendecourt, L.; Thiemann, W. H.-P. Urea, Glycolic Acid, and Glycerol in an Organic Residue Produced by Ultraviolet Irradiation of Interstellar/Pre-Cometary Ice Analogs. *Astrobiology* **2010**, *10*, 245–256.

(71) Barks, H. L.; Buckley, R.; Grieves, G. A.; Di Mauro, E.; Hud, N. V.; Orlando, T. M. Guanine, Adenine, and Hypoxanthine Production in UV-Irradiated Formamide Solutions: Relaxation of the Requirements for Prebiotic Purine Nucleobase Formation. *ChemBioChem* **2010**, *11*, 1240–1243.

(72) Congiu, E.; Chaabouni, H.; Laffon, C.; Parent, P.; Baouche, S.; Dulieu, F. Efficient

Surface Formation Route of Interstellar Hydroxylamine through NO Hydrogenation. I. the Submonolayer Regime on Interstellar Relevant Substrates. *J. Chem. Phys.* **2012**, *137*, 054714/1-10.

(73) Kaiser, R. I.; Maity, S.; Jones, B. M. Synthesis of Prebiotic Glycerol in Interstellar Ices. *Angew. Chemie - Int. Ed.* **2015**, *54*, 195–200.

(74) de Marcellus, P.; Meinert, C.; Myrgorodska, I.; Nahon, L.; Buhse, T.; D'Hendecourt, L. L. S.; Meierhenrich, U. J. Aldehydes and Sugars from Evolved Precometary Ice Analogs: Importance of Ices in Astrochemical and Prebiotic Evolution. *Proc. Natl. Acad. Sci. U. S. A.* **2015**, *112*, 965–970.

(75) MacDonald, G. J. Role of Methane Clathrates in Past and Future Climates. *Clim. Change* **1990**, *16*, 247–281.

(76) Makogon, Y. F.; Holditch, S. A.; Makogon, T. Y. Natural Gas-Hydrates - A Potential Energy Source for the 21st Century. *J. Pet. Sci. Eng.* **2007**, *56*, 14–31.

(77) Schüth, F. Technology: Hydrogen and Hydrates. *Nature* **2005**, *434*, 712–713.

(78) Veluswamy, H. P.; Kumar, R.; Linga, P. Hydrogen Storage in Clathrate Hydrates: Current State of the Art and Future Directions. *Appl. Energy* **2014**, *122*, 112–132.

(79) Aaron, D.; Tsouris, C. Separation of CO_2 from Flue Gas: A Review. *Sep. Sci. Technol.* **2005**, *40*, 321–348.

(80) Linga, P.; Kumar, R.; Lee, J. D.; Ripmeester, J.; Englezos, P. A New Apparatus to Enhance the Rate of Gas Hydrate Formation: Application to Capture of Carbon Dioxide. *Int. J. Greenh. Gas Control* **2010**, *4*, 630–637.

(81) D'Hendecourt, L. L. S.; de Muizon, M. J. The Discovery of Interstellar Carbon Dioxide. *Astron. Astrophys.* **1989**, *223*, L5-8.

(82) Gibb, E. L.; Whittet, D. C. B.; Schutte, W. A.; Boogert, A. C. A.; Chiar, J. E.; Ehrenfreund, P.; Gerakines, P. A.; Keane, J. V.; Tielens, A. G. G. M.; van Dishoeck, E. F.; et al. An Inventory of Interstellar Ices toward the Embedded Protostar W33A. *Astrophys. J.* **2000**, *536*, 347–356.

(83) Martínez-Botí, M. A.; Foster, G. L.; Chalk, T. B.; Rohling, E. J.; Sexton, P. F.; Lunt, D. J.; Pancost, R. D.; Badger, M. P. S.; Schmidt, D. N. Plio-Pleistocene Climate Sensitivity Evaluated Using High-Resolution CO_2 Records. *Nature* **2015**, *518*, 49–54.

(84) Martínez-Botí, M. A.; Marino, G.; Foster, G. L.; Ziveri, P.; Henehan, M. J.; Rae, J. W. B.; Mortyn, P. G.; Vance, D. Boron Isotope Evidence for Oceanic Carbon Dioxide Leakage during the Last Deglaciation. *Nature* **2015**, *518*, 219–222.

(85) Gibson, K. D.; Killelea, D. R.; Yuan, H.; Becker, J. S.; Pratihar, S.; Manikandan, P.; Kohale, S. C.; Hase, W. L.; Sibener, S. J. Scattering of High-Incident-Energy Kr and Xe from Ice: Evidence That a Major Channel Involves Penetration into the Bulk. *J. Phys. Chem. C* **2012**, *116*, 14264–14273.

(86) Gibson, K. D.; Killelea, D. R.; Becker, J. S.; Yuan, H.; Sibener, S. J. Energetic Ballistic

Deposition of Volatile Gases into Ice. *Chem. Phys. Lett.* **2012**, *531*, 18–21.

(87) Pratihar, S.; Kohale, S. C.; Yang, L.; Manikandan, P.; Gibson, K. D.; Killelea, D. R.; Yuan, H.; Sibener, S. J.; Hase, W. L. Chemical Dynamics Simulations of High Energy Xenon Atom Collisions with the {0001} Surface of Hexagonal Ice. *J. Phys. Chem. C* **2013**, *117*, 2183–2193.

(88) Ocampo, J.; Klinger, J. Adsorption of N_2 and CO_2 on Ice. *J. Colloid Interface Sci.* **1982**, *86*, 377–383.

(89) Bar-Nun, A.; Dror, J.; Kochavi, E.; Laufer, D. Amorphous Water Ice and Its Ability to Trap Gases. *Phys. Rev. B* **1987**, *35*, 2427–2435.

(90) Notesco, G.; Bar-Nun, A. Trapping of Methanol, Hydrogen Cyanide, and *n*-Hexane in Water Ice, above Its Transformation Temperature to the Crystalline Form. *Icarus* **1997**, *126*, 336–341.

(91) Collings, M. P.; Anderson, M. A.; Chen, R.; Dever, J. W.; Viti, S.; Williams, D. A.; McCoustra, M. R. S. A Laboratory Survey of the Thermal Desorption of Astrophysically Relevant Molecules. *Mon. Not. R. Astron. Soc.* **2004**, *354*, 1133–1140.

(92) Kumi, G.; Malyk, S.; Hawkins, S.; Reisler, H.; Wittig, C. Amorphous Solid Water Films: Transport and Guest-Host Interactions with CO_2 and N_2O Dopants. *J. Phys. Chem. A* **2006**, *110*, 2097–2105.

(93) Hood, L. L. Thermal Processing of Chondrule Precursors in Planetesimal Bow Shocks. *Meteorit. Planet. Sci.* **1998**, *33*, 97–107.

(94) Joslin, R. D. Aircraft Laminar Flow Control. *Annu. Rev. Fluid Mech.* **1998**, *30*, 1–29.

(95) Cebeci, T.; Kafyeke, F. Aircraft Icing. *Annu. Rev. Fluid Mech* **2003**, *35*, 11–21.

(96) Pirug, G.; Bonzel, H. . UHV Simulation of the Electrochemical Double Layer: Adsorption of $HClO_4/H_2O$ on Au(111). *Surf. Sci.* **1998**, *405*, 87–103.

(97) Henderson, M. A. The Interaction of Water with Solid Surfaces: Fundamental Aspects Revisited. *Surf. Sci. Rep.* **2002**, *46*, 1–308.

(98) Hodgson, A.; Haq, S. Water Adsorption and the Wetting of Metal Surfaces. *Surf. Sci. Rep.* **2009**, *64*, 381–451.

(99) Gibson, K. D.; Killelea, D. R.; Yuan, H.; Becker, J. S.; Sibener, S. J. Determination of the Sticking Coefficient and Scattering Dynamics of Water on Ice Using Molecular Beam Techniques. *J. Chem. Phys.* **2011**, *134*, 034703/1-7.

(100) Killelea, D. R.; Gibson, K. D.; Yuan, H.; Becker, J. S.; Sibener, S. J. Dynamics of the Sputtering of Water from Ice Films by Collisions with Energetic Xenon Atoms. *J. Chem. Phys.* **2012**, *136*, 144705/1-8.

(101) Tingey, G. L. Kinetics of the Water—Gas Equilibrium Reaction. I. The Reaction of Carbon Dioxide with Hydrogen. *J. Phys. Chem.* **1966**, *70*, 1406–1412.

(102) Shebaro, L.; Bhalotra, S. R.; Herschbach, D. Molecular Beam Chemistry: Formation of

Benzene and Other Higher Hydrocarbons from Small Alkanes and Alkenes in a Catalytic Supersonic Nozzle. *J. Phys. Chem. A* **1997**, *101*, 6775–6780.

(103) Itikawa, Y. Cross Sections for Electron Collisions with Carbon Dioxide. *J. Phys. Chem. Ref. Data* **2002**, *31*, 749–767.

(104) Itikawa, Y. Cross Sections for Electron Collisions with Nitrogen Molecules. *J. Phys. Chem. Ref. Data* **2006**, *35*, 31–53.

(105) Woltz, P. J. H.; Nielsen, A. H. The Infrared Spectra of CF_4 and GeF_4. *J. Chem. Phys.* **1952**, *20*, 307–312.

(106) Jones, L. H.; Kennedy, C.; Ekberg, S. Potential Constants of CF4. *J. Chem. Phys.* **1978**, *69* (2), 833–838.

(107) Byl, O.; Kondratyuk, P.; Forth, S. T.; FitzGerald, S. A.; Chen, L.; Johnson, J. K.; Yates Jr., J. T. Adsorption of CF_4 on the Internal and External Surfaces of Opened Single-Walled Carbon Nanotubes: A Vibrational Spectroscopy Study. *J. Am. Chem. Soc.* **2003**, *125*, 5889–5896.

(108) Fournier, R. P.; Savoie, R.; Bessette, F.; Cabana, A. Vibrational Spectra of Liquid and Crystalline CF_4. *J. Chem. Phys.* **1968**, *49*, 1159–1164.

(109) Falk, M. Amorphous Solid Carbon Dioxide. *J. Chem. Phys.* **1987**, *86*, 560–564.

(110) Gálvez, O.; Ortega, I. K.; Maté, B.; Moreno, M. A. A Study of the Interaction of CO_2 with Water Ice. *Astron. Astrophys.* **2007**, *472*, 691–698.

(111) Bernstein, M. P.; Cruikshank, D. P.; Sandford, S. A. Near-Infrared Laboratory Spectra of Solid H_2O/CO_2 and CH_3OH/CO_2 Ice Mixtures. *Icarus* **2005**, *179*, 527–534.

(112) Kimmel, G. A.; Stevenson, K. P.; Dohnálek, Z.; Smith, R. S.; Kay, B. D. Control of Amorphous Solid Water Morphology Using Molecular Beams. I. Experimental Results. *J. Chem. Phys.* **2001**, *114*, 5284–5294.

(113) Hodyss, R.; Johnson, P. V.; Orzechowska, G. E.; Goguen, J. D.; Kanik, I. Carbon Dioxide Segregation in 1:4 and 1:9 CO_2:H_2O Ices. *Icarus* **2008**, *194*, 836–842.

(114) Barnes, J. A.; Gough, T. E. Fourier Transform Infrared Spectroscopy of Molecular Clusters: The Structure and Internal Mobility of Clustered Carbon Dioxide. *J. Chem. Phys.* **1987**, *86*, 6012–6017.

(115) Ewing, G. E.; Sheng, D. T. Infrared Spectroscopy of CO_2 Ultrafine Particles. *J. Phys. Chem.* **1988**, *92*, 4063–4066.

(116) Fleyfel, F.; Devlin, J. P. FT-IR Spectra of CO_2 Clusters. *J. Phys. Chem.* **1989**, *93*, 7292–7294.

(117) Signorell, R.; Kunzmann, M. K. Isotope Effects on Vibrational Excitons in Carbon Dioxide Particles. *Chem. Phys. Lett.* **2003**, *371*, 260–266.

(118) Bonnamy, A.; Georges, R.; Hugo, E.; Signorell, R. IR Signature of $(CO_2)_N$ Clusters: Size, Shape and Structural Effects. *Phys. Chem. Chem. Phys.* **2005**, *7*, 963–969.

(119) Jones, L. H.; Swanson, B. I. Transverse Optical to Longitudinal Optical Splitting and Dipole Moment Derivatives from Infrared Spectra of Thin Films of Molecular Solids. *J. Phys. Chem.* **1991**, *95*, 2701–2707.

(120) Ovchinnikov, M. A.; Wight, C. A. Inhomogeneous Broadening of Infrared and Raman Spectral Bands of Amorphous and Polycrystalline Thin Films. *J. Chem. Phys.* **1993**, *99*, 3374–3379.

(121) Taraschewski, M.; Cammenga, H. K.; Tuckermann, R.; Bauerecker, S. FTIR Study of CO_2 and H_2O/CO_2 Nanoparticles and Their Temporal Evolution at 80 K. *J. Phys. Chem. A* **2005**, *109*, 3337–3343.

(122) Winkler, M.; Harnes, J.; Børve, K. J. Structure of Neutral Nanosized Clusters Produced by Coexpansion of CF_4 and CH_4. *J. Phys. Chem. A* **2011**, *115*, 13259–13268.

(123) Tsuzuki, S.; Uchimaru, T.; Mikami, M.; Urata, S. Magnitude and Orientation Dependence of Intermolecular Interaction between Perfluoroalkanes: High Level Ab Initio Calculations of CF_4 and C_2F_6 Dimers. *J. Chem. Phys.* **2002**, *116*, 3309–3315.

(124) Mahlanen, R.; Jalkanen, J.-P.; Pakkanen, T. A. Potential Energy Surfaces of CF_4, CCl_4 and CBr_4 Dimers. *Chem. Phys.* **2005**, *313*, 271–277.

(125) Caminati, W.; Maris, A.; Dell'Erba, A.; Favero, P. G. Dynamical Behavior and Dipole-Dipole Interactions of Tetrafluoromethane-Water. *Angew. Chemie Int. Ed.* **2006**, *45*, 6711–6714.

(126) Sandford, S. A.; Allamandola, L. J. The Physical and Infrared Spectral Properties of CO_2 in Astrophysical Ice Analogs. *Astrophys. J.* **1990**, *355*, 357–372.

(127) Escribano, R. M.; Muñoz Caro, G. M.; Cruz-Diaz, G. A.; Rodríguez-Lazcano, Y.; Maté, B. Crystallization of CO_2 Ice and the Absence of Amorphous CO_2 Ice in Space. *Proc. Natl. Acad. Sci. U. S. A.* **2013**, *110*, 12899–12904.

(128) Ehrenfreund, P.; Boogert, A. C. A.; Gerakines, P. A.; Tielens, A. G. G. M.; van Dishoeck, E. F. Infrared Spectroscopy of Interstellar Apolar Ice Analogs. *Astron. Astrophys.* **1997**, *328*, 649–669.

(129) Buch, V.; Delzeit, L.; Blackledge, C.; Devlin, J. P. Structure of the Ice Nanocrystal Surface from Simulated versus Experimental Spectra of Adsorbed CF_4. *J. Phys. Chem.* **1996**, *100*, 3732–3744.

(130) Devlin, J. P.; Buch, V. Vibrational Spectroscopy and Modeling of the Surface and Subsurface of Ice and of Ice−Adsorbate Interactions. *J. Phys. Chem. B* **1997**, *101*, 6095–6098.

(131) *CRC Handbook of Chemistry and Physics*, 89th ed.; Lide, D. R., Ed.; GRC Press: Boca Raton, FL, 2009.

(132) Lennard-Jones, J. E. Processes of Adsorption and Diffusion on Solid Surfaces. *Trans. Faraday Soc.* **1932**, *28*, 333–359.

(133) Balooch, M.; Cardillo, M. J.; Miller, D. R.; Stickney, R. E. Molecular Beam Study of the

Apparent Activation Barrier Associated with Adsorption and Desorption of Hydrogen on Copper. *Surf. Sci.* **1974**, *46*, 358–392.

(134) Harris, J. On Vibrationally-Assisted Dissociation of H_2 at Metal Surfaces. *Surf. Sci.* **1989**, *221*, 335–345.

(135) Smith, R. S.; Dohnálek, Z.; Kimmel, G. A.; Stevenson, K. P.; Kay, B. D. The Self-Diffusivity of Amorphous Solid Water near 150 K. *Chem. Phys.* **2000**, *258*, 291–305.

(136) Angell, C. A. Amorphous Water. *Annu. Rev. Phys. Chem.* **2004**, *55*, 559–583.

(137) Shalit, A.; Perakis, F.; Hamm, P. Two-Dimensional Infrared Spectroscopy of Isotope-Diluted Low Density Amorphous Ice. *J. Phys. Chem. B* **2013**, *117*, 15512–15518.

(138) Langlois, G. G.; Thompson, R. S.; Li, W.; Sibener, S. J. Oxidation, Destruction, and Persistence of Multilayer Dimethyl Methylphosphonate Films during Exposure to $O(^3P)$ Atomic Oxygen. *J. Phys. Chem. C* **2016**, *120*, 16863–16870.

(139) Bothe, M. A. The Chemical Weapons Convention: A General Overview. In *The New Chemical Weapons Convention: Implementation and Prospects*; Michael Bothe, Natalino Ronzitti, A. R., Ed.; Kluwer Law International: Cambridge, MA, 1999; p 600.

(140) Kim, K.; Tsay, O. G.; Atwood, D. A.; Churchill, D. G. Destruction and Detection of Chemical Warfare Agents. *Chem. Rev.* **2011**, *111*, 5345–5403.

(141) Davies, P. R.; Newton, N. G. The Chemisorption of Organophosphorus Compounds at an Al(111) Surface. *Appl. Surf. Sci.* **2001**, *181*, 296–306.

(142) Ekerdt, J. G.; Klabunde, K. J.; Shapley, J. R.; White, J. M.; Yates, J. T. J. Surface Chemistry of Organophosphorus Compunds. *J. Phys. Chem.* **1988**, *92*, 6182–6188.

(143) Hegde, R. I.; Greenlief, C. M.; White, J. M. Surface Chemistry of Dimethyl Methylphosphonate on Rh(100). *J. Phys. Chem. A* **1985**, *89*, 2886–2891.

(144) Henderson, M. A.; White, J. M. Adsorption and Decomposition of Dimethyl Methylphosphonate on Platinum(111). *J. Am. Chem. Soc.* **1988**, *110*, 6939–1947.

(145) Smentkowski, V. S.; Hagans, P.; Yates, J. T. Study of the Catalytic Destruction of Dimethyl Methylphosphonate: Oxidation over Mo(110). *J. Phys. Chem.* **1988**, *92*, 6351–6357.

(146) Chen, D. A.; Ratliff, J. S.; Hu, X.; Gordon, W. O.; Senanayake, S. D.; Mullins, D. R. Dimethyl Methylphosphonate Decomposition on Fully Oxidized and Partially Reduced Ceria Thin Films. *Surf. Sci.* **2010**, *604*, 574–587.

(147) Davis, E. D.; Gordon, W. O.; Wilmsmeyer, A. R.; Troya, D.; Morris, J. R. Chemical Warfare Agent Surface Adsorption: Hydrogen Bonding of Sarin and Soman to Amorphous Silica. *J. Phys. Chem. Lett.* **2014**, *5*, 1393–1399.

(148) Kim, C.; Lad, R.; Tripp, C. Interaction of Organophosphorous Compounds with TiO_2 and WO_3 Surfaces Probed by Vibrational Spectroscopy. *Sens. Actuators, B* **2001**, *76*, 442–448.

(149) Mitchell, M. B.; Sheinker, V. N.; Mintz, E. A. Adsorption and Decomposition of

Dimethyl Methylphosphonate on Metal Oxides. *J. Phys. Chem. B* **1997**, *101*, 11192–11203.

(150) Panayotov, D. A.; Morris, J. R. Uptake of a Chemical Warfare Agent Simulant (DMMP) on TiO_2: Reactive Adsorption and Active Site Poisoning. *Langmuir* **2009**, *25*, 3652–3658.

(151) Panayotov, D. A.; Morris, J. R. Thermal Decomposition of a Chemical Warfare Agent Simulant (DMMP) on TiO2: Adsorbate Reactions with Lattice Oxygen as Studied by Infrared Spectroscopy. *J. Phys. Chem. C* **2009**, *113*, 15684–15691.

(152) Segal, S. R.; Cao, L.; Suib, S. L.; Tang, X.; Satyapal, S. Thermal Decomposition of Dimethyl Methylphosphonate over Manganese Oxide Catalysts. *J. Catal.* **2001**, *198*, 66–76.

(153) Wilmsmeyer, A. R.; Gordon, W. O.; Davis, E. D.; Troya, D.; Mantooth, B. A.; Lalain, T. A.; Morris, J. R. Infrared Spectra and Binding Energies of Chemical Warfare Nerve Agent Simulants on the Surface of Amorphous Silica. *J. Phys. Chem. C* **2013**, *117*, 15685–15697.

(154) Wilmsmeyer, A. R.; Uzarski, J.; Barrie, P. J.; Morris, J. R. Interactions and Binding Energies of Dimethyl Methylphosphonate and Dimethyl Chlorophosphate with Amorphous Silica. *Langmuir* **2012**, *28*, 10962–10967.

(155) Gordon, W. O.; Tissue, B. M.; Morris, J. R. Adsorption and Decomposition of Dimethyl Methylphosphonate on Y_2O_3 Nanoparticles. *J. Phys. Chem. C* **2007**, *111*, 3233–3240.

(156) Bermudez, V. M. Investigation of the Interaction of γ-Al_2O_3 with Aqueous Solutions of Dimethyl Methylphosphonate Using Infrared Multiple Internal Reflection Spectroscopy. *Langmuir* **2013**, *29*, 1483–1489.

(157) Bermudez, V. M. Effect of Humidity on the Interaction of Dimethyl Methylphosphonate (DMMP) Vapor with SiO_2 and Al_2O_3 Surfaces, Studied Using Infrared Attenuated Total Reflection Spectroscopy. *Langmuir* **2010**, *26*, 18144–18154.

(158) Li, Y.; Klabunde, K. J. Nanoscale Metal Oxide Particles as Chemical Reagents. Destructive Adsorption of a Chemical Agent Simulant, Dimethyl Methylphosphonate, on Heat-Treated Magnesium Oxide. *Langmuir* **1991**, *7*, 1388–1393.

(159) Panayotov, D. A.; Morris, J. R. Catalytic Degradation of a Chemical Warfare Agent Simulant: Reaction Mechanisms on TiO2-Supported Au Nanoparticles. *J. Phys. Chem. C* **2008**, *112*, 7496–7502.

(160) Mattsson, A.; Lejon, C.; Štengl, V.; Bakardjieva, S.; Opluštil, F.; Andersson, P. O.; Österlund, L. Photodegradation of DMMP and CEES on Zirconium Doped Titania Nanoparticles. *Appl. Catal. B Environ.* **2009**, *92*, 401–410.

(161) Bertilsson, L.; Engquist, I.; Liedberg, B. Interaction of Dimethyl Methylphosphonate with Alkanethiolate Monolayers Studied by Temperature-Programmed Desorption and Infrared Spectroscopy. *J. Phys. Chem. B* **1997**, *101*, 6021–6027.

(162) Bertilsson, L.; Potje-Kamloth, K.; Liess, H.-D.; Liedberg, B. On the Adsorption of Dimethyl Methylphosphonate on Self-Assembled Alkanethiolate Monolayers: Influence

of Humidity. *Langmuir* **1999**, *15*, 1128–1135.

(163) Bertilsson, L.; Potje-Kamloth, K.; Lieβ, H.-D. Molecular Interaction of DMMP and Water Vapor with Mixed Self-Assembled Monolayers Studied by IR Spectroscopy and SAW Devices. *Thin Solid Films* **1996**, *284–285* (95), 882–887.

(164) Ferguson-McPherson, M. K.; Low, E. R.; Esker, A. R.; Morris, J. R. Sorption of Dimethyl Methylphosphonate within Langmuir-Blodgett Films of Trisilanolphenyl Polyhedral Oligomeric Silsesquioxane. *J. Phys. Chem. B* **2005**, *109*, 18914–18920.

(165) Bermudez, V. M. Quantum-Chemical Study of the Adsorption of DMMP and Sarin on γ-Al_2O_3. *J. Phys. Chem. C* **2007**, *111*, 3719–3728.

(166) Bermudez, V. M. Computational Study of the Adsorption of Trichlorophosphate, Dimethyl Methylphosphonate, and Sarin on Amorphous SiO_2. *J. Phys. Chem. C* **2007**, *111*, 9314–9323.

(167) Bermudez, V. M. Computational Study of Environmental Effects in the Adsorption of DMMP, Sarin, and VX on γ-Al_2O_3: Photolysis and Surface Hydroxylation. *J. Phys. Chem. C* **2009**, *113*, 1917–1930.

(168) Quenneville, J.; Taylor, R. S.; Van Duin, A. C. T. Reactive Molecular Dynamics Studies of DMMP Adsorption and Reactivity on Amorphous Silica Surfaces. *J. Phys. Chem. C* **2010**, *114*, 18894–18902.

(169) Yang, L.; Taylor, R.; de Jong, W. A.; Hase, W. L. A Model DMMP/TiO_2 (110) Intermolecular Potential Energy Function Developed from Ab Initio Calculations. *J. Phys. Chem. C* **2011**, *115*, 12403–12413.

(170) Troya, D.; Edwards, A. C.; Morris, J. R. Theoretical Study of the Adsorption of Organophosphorous Compounds to Models of a Silica Surface. *J. Phys. Chem. C* **2013**, *117*, 14625–14634.

(171) Taylor, D. E.; Runge, K.; Cory, M. G.; Burns, D. S.; Vasey, J. L.; Hearn, J. D.; Gri, K.; Henley, M. V. Surface Binding of Organophosphates on Silica: Comparing Experiment and Theory. *J. Phys. Chem. C* **2013**, *117*, 2699–2708.

(172) Michalkova, A.; Ilchenko, M.; Gorb, L.; Leszczynski, J. Theoretical Study of the Adsorption and Decomposition of Sarin on Magnesium Oxide. *J. Phys. Chem. B* **2004**, *108*, 5294–5303.

(173) Mitchell, M. B.; Sheinker, V. N.; Cox, W. W. Room Temperature Reaction of Ozone and Dimethyl Methylphosphonate (DMMP) on Alumina-Supported Iron Oxide. *J. Phys. Chem. C* **2007**, *111*, 9417–9426.

(174) Mitchell, M. B.; Sheinker, V. N.; Cox Jr., W. W.; Hardcastle, K. Sustained Room Temperature Decomposition of Dimethyl Methylphosphonate (DMMP) by O_3 on Alumina-Supported MnO_x. *J. Phys. Chem. C* **2011**, *115*, 11514–11524.

(175) Li, Z.; Li, Y.; Cao, P.; Zhao, H. Surface Decontamination of Chemical Agent Surrogates Using an Atmospheric Pressure Air Flow Plasma Jet. *Plasma Sci. Technol.* **2013**, *15*, 696–701.

(176) Moeller, T. M.; Alexander, M. L.; Engelhard, M. H.; Gaspar, D. J.; Luna, M. L.; Irving, P. M. Surface Decontamination of Simulated Chemical Warfare Agents Using a Nonequilibrium Plasma With Off-Gas Monitoring. *IEEE Trans. Plasma Sci.* **2002**, *30*, 1454–1459.

(177) Kim, D. B.; Gweon, B.; Moon, S. Y.; Choe, W. Decontamination of the Chemical Warfare Agent Simulant Dimethyl Methylphosphonate by Means of Large-Area Low-Temperature Atmospheric Pressure Plasma. *Curr. Appl. Phys.* **2009**, *9*, 1093–1096.

(178) Zhu, W.-C.; Wang, B.-R.; Xi, H.-L.; Pu, Y.-K. Decontamination of VX Surrogate Malathion by Atmospheric Pressure Radio-Frequency Plasma Jet. *Plasma Chem. Plasma Process.* **2010**, *30*, 381–389.

(179) Herrmann, H. W.; Henins, I.; Park, J.; Selwyn, G. S. Decontamination of Chemical and Biological Warfare (CBW) Agents Using an Atmospheric Pressure Plasma Jet (APPJ). *Phys. Plasmas* **1999**, *6*, 2284–2289.

(180) Zegers, E. J. P.; Fisher, E. M. Gas-Phase Pyrolysis of Diisopropyl Methylphosphonate. *Combust. Flame* **1998**, *115*, 230–240.

(181) Korobeinichev, O. P.; Ilyin, S. B.; Shvartsberg, V. M.; Chernov, A. A. The Destruction Chemistry of Organophosphorus Compounds in Flames—I: Quantitative Determination of Final Phosphorus-Containing Species in Hydrogen-Oxygen Flames. *Combust. Flame* **1999**, *118*, 718–726.

(182) Glaude, P. A.; Melius, C.; Pitz, W. J.; Westbrook, C. K. Detailed Chemical Kinetic Reaction Mechanisms for Incineration of Organophosphorus and Fluoroorganophosphorus Compounds. *Proc. Combust. Inst.* **2002**, *29*, 2469–2476.

(183) Liang, S.; Hemberger, P.; Neisius, N. M.; Bodi, A.; Grützmacher, H.; Levalois-Grützmacher, J.; Gaan, S. Elucidating the Thermal Decomposition of Dimethyl Methylphosphonate by Vacuum Ultraviolet (VUV) Photoionization: Pathways to the PO Radical, a Key Species in Flame-Retardant Mechanisms. *Chem. - A Eur. J.* **2015**, *21*, 1073–1080.

(184) Korobeinichev, O. P.; Shvartsberg, V. M.; Shmakov, A. G.; Bolshova, T. A.; Jayaweera, T. M.; Melius, C. F.; Pitz, W. J.; Westbrook, C. K.; Curran, H. Flame Inhibition by Phosphorus-Containing Compounds in Lean and Rich Propane Flames. *Proc. Combust. Inst.* **2005**, *30*, 2353–2360.

(185) Conforti, P. F.; Braunstein, M.; Dodd, J. A. Energetics and Dynamics of the Reactions of O(^{3}P) with Dimethyl Methylphosphonate and Sarin. *J. Phys. Chem. A* **2009**, *113*, 13752–13761.

(186) Conforti, P. F.; Braunstein, M.; Stearns, J. A.; Dodd, J. A. Collision Dynamics of O(^{3}P) + DMMP Using a Specific Reaction Parameters Potential Form. *J. Phys. Chem. A* **2012**, *116*, 2506–2518.

(187) Davisson, M.; Love, A.; Vance, A.; Reynolds, J. *Environmental Fate of Organophosphorus Compounds Related to Chemical Weapons*; Livermore, CA, 2005.

(188) Fitch, J. P.; Raber, E.; Imbro, D. R. Technology Challenges in Responding to Biological

or Chemical Attacks in the Civilian Sector. *Science* **2003**, *302*, 1350–1354.

(189) Gibson, K. D.; Sibener, S. J. Scattering Dynamics, Survival, and Dispersal of Dimethyl Methylphosphonate Interacting with the Surface of Multilayer Graphene. *J. Phys. Chem. A* **2016**, *120*, 4863–4871.

(190) Itikawa, Y. Cross Sections for Electron Collisions with Oxygen Molecules. *J. Phys. Chem. Ref. Data* **2009**, *38*, 1–20.

(191) Templeton, M.; Weinberg, W. H. Decomposition of Phosphonate Esters Adsorbed on Aluminum Oxide. *J. Am. Chem. Soc.* **1985**, *107*, 774–779.

(192) Eaton, G.; Harris, L.; Patel, K.; Symons, M. C. R. Infrared and Nuclear Magnetic Resonance Spectroscopic Studies on the Solvation of Trimethylphosphate and Dimethylphosphonate. *J. Chem. Soc. Faraday Trans* **1992**, *88*, 3527–3531.

(193) Herman, M. A.; Van Der Veken, B. J.; Barnes, A. J. Vibrational Studies on Conformational Equilibrium in Dimethylmethylphosphonate and Methyldimethylphosphinate. *J. Mol. Struct.* **1983**, *99*, 197–206.

(194) Lomax, S.; Barnes, A. J.; Van Der Veken, B. J. Conformational Behaviour of Dimethylmethylphosphonate and Methyldimethylphosphinate Studied by Infrared Spectroscopy in Low-Temperature Matrices. *J. Mol. Struct.* **1983**, *99*, 137–145.

(195) Vishnyakov, A.; Neimark, A. V. Molecular Model of Dimethylmethylphosphonate and Its Interactions with Water. *J. Phys. Chem. A* **2004**, *108*, 1435–1439.

(196) Cuisset, A.; Mouret, G.; Pirali, O.; Roy, P.; Cazier, F.; Nouali, H.; Demaison, J. Gas-Phase Vibrational Spectroscopy and Ab Initio Study of Organophosphorus Compounds: Discrimination between Species and Conformers. *J. Phys. Chem. B* **2008**, *112*, 12516–12525.

(197) Garton, D. J.; Minton, T. K.; Alagia, M.; Balucani, N.; Casavecchia, P.; Volpi, G. G. Reactive Scattering of Ground-State and Electronically Excited Oxygen Atoms on a Liquid Hydrocarbon Surface. *Faraday Discuss.* **1997**, *108*, 387–399.

(198) Garton, D. J.; Minton, T. K.; Alagia, M.; Balucani, N.; Casavecchia, P.; Gualberto Volpi, G. Comparative Dynamics of Cl(^{2}P) and O(^{3}P) Interactions with a Hydrocarbon Surface. *J. Chem. Phys.* **2000**, *112*, 5975–5984.

(199) Paz, Y.; Trakhtenberg, S.; Naaman, R. Reaction between O(^{3}P) and Organized Organic Thin-Films. *J. Phys. Chem.* **1994**, *98*, 13517–13523.

(200) Thomas, L. C. *Interpretation of the Infrared Spectra of Organophosphorus Compounds*; Heyden & Son Ltd.: London, 1974.

(201) Aschmann, S. M.; Tuazon, E. C.; Atkinson, R. Atmospheric Chemistry of Diethyl Methylphosphonate, Diethyl Ethylphosphonate, and Triethyl Phosphate. *J. Phys. Chem. A* **2005**, *109* (10), 2282–2291.

(202) Ganesan, K.; Raza, S. K.; Vijayaraghavan, R. Chemical Warfare Agents. *J. Pharm. BioAllied Sci.* **2010**, *2*, 166–178.

(203) Smith, C. S.; Metcalfe, E. A Study of Fire-Retardant Mechanisms in the Gas Phase by FTIR Spectroscopy. *Polym. Int.* **2000**, *49*, 1169–1176.

(204) Szinicz, L. History of Chemical and Biological Warfare Agents. *Toxicology* **2005**, *214*, 167–181.

(205) Bartelt-Hunt, S. L.; Knappe, D. R. U.; Barlaz, M. A. A Review of Chemical Warfare Agent Simulants for the Study of Environmental Behavior. *Crit. Rev. Environ. Sci. Technol.* **2008**, *38*, 112–136.

(206) Munro, N. B.; Talmage, S. S.; Griffin, G. D.; Waters, L. C.; Watson, A. P.; King, J. F.; Hauschild, V. The Sources, Fate, and Toxicity of Chemical Warfare Agent Degradation Products. *Environ. Health Perspect.* **1999**, *107*, 933–974.

(207) Hu, S. X.; Yu, J. G.; Zeng, E. Y. Atmospheric Degradation Mechanisms of a Simulant Organophosphorus Pesticide Isopropyl Methyl Methylphosphonate: A Theoretical Consideration. *Int. J. Quantum Chem.* **2013**, *113*, 1128–1136.

(208) Aschmann, S. M.; Tuazon, E. C.; Long, W. D.; Atkinson, R. Atmospheric Chemistry of Isopropyl Methyl Methylphosphonate and Dimethyl N,N-Dimethylphosphoroamidate. *J. Phys. Chem. A* **2010**, *114*, 3523–3532.

(209) Martin, P.; Tuazon, E. C.; Atkinson, R.; Maughan, A. D. Atmospheric Gas-Phase Reactions of Selected Phosphorus-Containing Compounds. *J. Phys. Chem. A* **2002**, *106*, 1542–1550.

(210) Liu, Y.; Liggio, J.; Harner, T.; Jantunen, L.; Shoeib, M.; Li, S. M. Heterogeneous OH Initiated Oxidation: A Possible Explanation for the Persistence of Organophosphate Flame Retardants in Air. *Environ. Sci. Technol.* **2014**, *48*, 1041–1048.

(211) Kim, S. H.; Kim, J. H.; Kang, B. K. Decomposition Reaction of Organophosphorus Nerve Agents on Solid Surfaces with Atmospheric Radio Frequency Plasma Generated Gaseous Species. *Langmuir* **2007**, *23*, 8074–8078.

(212) Cory, M. G.; Taylor, D. E.; Bunte, S. W.; Runge, K.; Vasey, J. L.; Burns, D. S. Theoretical Methodology for Prediction of Tropospheric Oxidation of Dimethyl Phosphonate and Dimethyl Methylphosphonate. *J. Phys. Chem. A* **2011**, *115*, 1946–1954.

(213) Guilbault, G. G.; Scheide, E.; Das, J. An Experimental Technique for Studying the Infrared Spectrum of Chemisorbed Compounds. *Spectrosc. Lett.* **1996**, *1*, 167–175.

(214) Crooks, R. M.; Yang, H. C.; McEllistrem, L. J.; Thomas, R. C.; Ricco, A. J. Interactions between Self-Assembled Monolayers and an Organophosphonate Detailed Study Using Surface Acoustic Wave-Based Mass Analysis, Polarization Modulation-FTIR Spectroscopy and Ellipsometry. *Faraday Discuss.* **1997**, *107*, 285–305.

(215) Mott, A. J.; Rez, P. Calculated Infrared Spectra of Nerve Agents and Simulants. *Spectrochim. Acta - Part A Mol. Biomol. Spectrosc.* **2012**, *91*, 256–260.

(216) Hameka, H. F.; Carrieri, A. H.; Jensen, J. O. Calculations of the Structure and the Vibrational Infrared Frequencies of Some Methylphosphonates. *Phosphorus. Sulfur. Silicon Relat. Elem.* **1992**, *66*, 1–11.

(217) Weber, M.; de Moraes, I. R.; Motheo, A. J.; Nart, F. C. In Situ Vibrational Spectroscopy Analysis of Adsorbed Phosphate Species on Gold Single Crystal Electrodes. *Colloids Surfaces A Physicochem. Eng. Asp.* **1998**, *134*, 103–111.

(218) Weber, M.; Nart, F. C. On the Adsorption of Ionic Phosphate Species on Au(111)—an in situ FTIR Study. *Electrochim. Acta* **1996**, *41*, 653–659.

(219) Waghe, A.; Kanan, S. M.; Abu-Yousef, I.; Jensen, B.; Tripp, C. P. Infrared Study of UV-Irradiated Tungsten Trioxide Powders Containing Adsorbed Dimethyl Methyl Phosphonate and Trimethyl Phosphate. *Res. Chem. Intermed.* **2006**, *32*, 613–623.

(220) Connor, P. A.; McQuillan, A. J. Phosphate Adsorption onto TiO_2 from Aqueous Solutions: An in Situ Internal Reflection Infrared Spectroscopic Study. *Langmuir* **1999**, *15*, 2916–2921.

(221) Pleshko, N.; Boskey, A.; Mendelsohn, R. Novel Infrared Spectroscopic Method for the Determination of Crystallinity of Hydroxyapatite Minerals. *Biophys. J.* **1991**, *60*, 786–793.

(222) Kuiper, A. E. T.; van Bokhoven, J. J. G. M.; Medema, J. The Role of Heterogeneity in the Kinetics of a Surface Reaction. I. Infrared Characterization of the Adsorption Structures of Organophosphonates and Their Decomposition. *J. Catal.* **1976**, *43*, 154–167.

(223) Li, Y. X.; Schlup, J. R.; Klabunde, K. J. Fourier Transform Infrared Photoacoustic Spectroscopy Study of the Adsorption of Organophosphorus Compounds on Heat-Treated Magnesium Oxide. *Langmuir* **1991**, *7*, 1394–1399.

(224) Burns, D. S.; Cory, M. G.; Taylor, D. E.; Bunte, S. W.; Runge, K.; Vasey, J. L. A Comparison of Primary and Secondary Hydrogen Abstraction from Organophosphates by Hydroxyl Radical. *Int. J. Chem. Kinet.* **2013**, *45*, 187–201.

(225) Aschmann, S. M.; Long, W. D.; Atkinson, R. Rate Constants for the Gas-Phase Reactions of OH Radicals with Dimethyl Phosphonate over the Temperature Range of 278-351 K and for a Series of Other Organophosphorus Compounds at ~280 K. *J. Phys. Chem. A* **2008**, *112*, 4793–4799.

(226) Aschmann, S. M.; Long, W. D.; Atkinson, R. Temperature-Dependent Rate Constants for the Gas-Phase Reactions of OH Radicals with 1,3,5-Trimethylbenzene, Triethyl Phosphate, and a Series of Alkylphosphonates. *J. Phys. Chem. A* **2006**, *110*, 7393–7400.

(227) Abbott, A.; Sierakowski, T.; Kiddle, J. J.; Clark, K. K.; Mezyk, S. P. Detailed Investigation of the Radical-Induced Destruction of Chemical Warfare Agent Simulants in Aqueous Solution. *J. Phys. Chem. B* **2010**, *114*, 7681–7685.

(228) Atkinson, R. Gas-Phase Tropospheric Chemistry of Volatile Organic Compounds: 1. Alkanes and Alkenes. *J. Phys. Chem. Ref. Data* **1997**, *26*, 215–290.

(229) Denisov, E. T. Solid-Phase Radical Reactions and Mechanism of Oxidation of Carbon-Chain Polymers. *Russ. Chem. Rev.* **1978**, *47*, 572–586.

(230) Ingold, K. U. Peroxy Radicals. *Acc. Chem. Res.* **1969**, *2*, 1–9.

(231) Aguila, A.; O'Shea, K. E.; Tobien, T.; Asmus, K.-D. Reactions of Hydroxyl Radical with Dimethyl Methylphosphonate and Diethyl Methylphosphonate. A Fundamental Mechanistic Study. *J. Phys. Chem. A* **2001**, *105*, 7834–7839.

(232) Atkinson, R.; Baulch, D. L.; Cox, R. A.; Crowley, J. N.; Hampson, R. F.; Hynes, R. G.; Jenkin, M. E.; Rossi, M. J.; Troe, J.; IUPAC Subcommittee. Evaluated Kinetic and Photochemical Data for Atmospheric Chemistry: Volume II -- Gas Phase Reactions of Organic Species. *Atmos. Chem. Phys.* **2006**, *6*, 3625–4055.

(233) Orlando, J. J.; Tyndall, G. S. Laboratory Studies of Organic Peroxy Radical Chemistry: An Overview with Emphasis on Recent Issues of Atmospheric Significance. *Chem. Soc. Rev.* **2012**, *41*, 6294–6317.

(234) Devolder, P.; Fittschen, C.; Frenzel, A.; Hippler, H.; Poskrebyshev, G.; Striebelb, F.; Viskolczc, B.; Ehrstuhl, L. Complete Falloff Curves for the Unimolecular Decomposition of I-Propoxy Radicals between 330 and 408 K. *Phys. Chem. Chem. Phys.* **1999**, *1*, 675–681.

(235) Peeters, J.; Fantechi, G.; Vereecken, L. A Generalized Structure-Activity Relationship for the Decomposition of (Substituted) Alkoxy Radicals. *J. Atmos. Chem.* **2004**, *48*, 59–80.

(236) Atkinson, R.; Carter, W. P. L. Reactions of Alkoxy Radicals under Atmospheric Conditions: The Relative Importance of Decomposition versus Reaction with O2. *J. Atmos. Chem.* **1991**, *13*, 195–210.

(237) Ferenac, M. A.; Davis, A. J.; Holloway, A. S.; Dibble, T. S. Isomerization and Decomposition Reactions of Primary Alkoxy Radicals Derived from Oxygenated Solvents. *J. Phys. Chem. A* **2003**, *107*, 63–72.

(238) Moad, G.; Solomon, D. H. *The Chemistry of Radical Polymerization*; Elsevier: Amsterdam Boston, 2006.

(239) Carlier, M.; Sochet, L.-R. Detection by E.S.R. of Peroxy Radicals: The Importance of Radical-Radical Reactions in the Slow Oxidation of Butane. *Combust. Flame* **1975**, *25*, 309–312.

(240) Korobeinichev, O. P.; Shvartsberg, V. M.; Shmakov, A. G. The Chemistry of Combustion of Organophosphorus Compounds. *Russ. Chem. Rev.* **2007**, *76*, 1094–1121.